FABRICATION AND CHARACTERIZATION OF ULTRAFILTRATION AND NANOFILTRATION MEMBRANES

WANG KAIYU

(*M. Eng., Tianjin University*)

A THESIS SUBMITTED

FOR THE DEGREE OF PHYLOSOPHY OF DOCTOR

DEPARTMENT OF CHEMICAL & BIOMOLECULAR ENGINEERING

NATIONAL UNIVERSITY OF SINGAPORE

2005

Acknowledgement

First of all, I would like to express my deepest appreciation to my academic supervisor, Professor Neal Chung Tai-Shung, for his invaluable guidance and help throughout this research project. I gratefully acknowledge National University of Singapore (NUS) for providing me an opportunity to pursue my Ph.D degree and the research scholarship.

I would also like to thank my thesis committee membranes, Prof. Renbi Bai and Prof. Lianfa Song for their constructive advice and instruction. I would especially thank Prof. Takeshi Matsuura from University of Ottawa, Canada for his kind helps and invaluable suggestions to my research work, and providing technical support for the permeation apparatus. I also want to thanks Dr. K. P. Pramoda from IMRE for her helps.

I also wish to take this opportunity to give my sincere thanks to all the colleagues in our research group for their kind assistance. Special thanks are due to Dr. Chun Cao, Ms. Meilin Chng, Dr. Peishi Tin, Ms. Weifen Guo, Mr. Lu Shao, Mr. Youchang Xiao, Ms. May May Teoh, Mr. Junying Xiong, Ms. Lanying Jiang, Ms. Xiangyi Qiao, Mr. Ruixue Liu, Mr. Santoso Yohannes Ervan and Ms. Natalia Widjojo for their assistance and generous suggestions; Mdm. H. J. Chiang, Mdm S. M. Chew and Mr. K. P. Ng from the Department of Chemical and Biomolecular Engineering in NUS for their support.

Last but not least, I am most grateful to my wife Ms. Zhaoxia Wang, my parents and my family for their endless love, encouragement and support that enable me to continue my academic pursuing.

Table of Contents

Summary

Effects of flow angle within spinneret and dope flow rate during spinning on the morphology, water permeability and separation performance of poly(ethersulfone) ultrafiltration hollow fiber membranes were investigated. The wet-spinning process was purposely chosen to fabricate hollow fibers without extra drawing. Experimental results suggest that higher dope flow rates (shear rates) in the spinneret produced UF hollow fiber membranes with smaller pore sizes and denser skin layers due to the enhanced molecular orientation. Hollow fibers spun from a conical spinneret had smaller mean pore sizes with larger geometric standard deviations than hollow fibers spun from a traditional straight spinneret. Macrovoids can be significantly suppressed and almost disappear for the 90° spinneret at high dope flow rates while this was not observed for the 60° conical spinneret. On the other hand, finger-like macrovoids in asymmetric hollow fiber membranes can be completely eliminated under high elongational stresses.

Two flat composite nanofiltration membranes (NADIR® N30F and NF PES10) were systematically characterized by using neutral molecules and electrolytes. Both irreversible thermodynamic and steric-hindrance pore (SHP) models were applied to estimate structural parameters. The effective charge density (ϕX) determined from the Teorell-Meyer-Sievers (TMS) model through fitting the NaCl rejection data, varied as a function of electrolyte concentration. These two negatively charged membranes expressed higher rejection to divalent anions, lower rejection to divalent cations and can fractionate anions in the binary salt mixture solutions of $NaCl/Na_2SO_4$. Through adjusting

pH, the separation of cephalexin can be effectively manipulated while N30F membrane shows higher rejection to cephalexin than NF PES10 membrane.

A novel process was proposed for preparing polybenzimidazole (PBI) nanofiltration membrane through chemically modifying the as-cast composite PBI membrane with *p*-Xylylene dichloride. The modified PBI membranes had decreased mean pore size and narrowed pore size distribution. Moreover, the mean pore size can be controlled through the modification process. The modified PBI nanofiltration membranes had improved the ion rejection performance for liquid separation, especially for multivalent cations and anions fractionation. Moreover, this modified PBI membrane can be utilized for the separation of cephalexin under a wide range of pH.

Based on the unique amphoteric property of imidazole group within PBI, a novel PBI NF hollow fiber membrane was fabricated by a one-step phase inversion process without post-treatment. The resultant mechanically stable PBI membranes can withstand trans-membrane pressures up to 30 bars. It was found that the mean effective pore size decreased, while the pure water permeability increased with an increase in elongational draw ratio. The PBI membrane exhibited higher rejection to divalent cations, lower rejection to divalent anions and the lowest rejection to monovalent ions at pH 7.0. Divalent and monovalent ions in $NaCl/MgCl_2$ and $NaCl/Na_2SO_4$ binary salt solutions can be effectively fractionated due to the ion competition. By adjusting pH, PBI membranes showed high separation to cephalexin over a wide range of pH. Moreover, the PBI NF membranes exhibited high Cr(VI) rejection and chemical stable in the basic solutions.

LIST of TABLES

LIST of FIGURES

Nomenclature

A	effective filtration area of membrane, [m^2]
$A_k/\Delta x$	ratio of membrane porosity to thickness, [m^{-1}]
C_b	solute concentration in the bulk solution, [$mol\ m^{-3}$]
C_f	solute concentration in the feed solution, [$mol\ m^{-3}$]
C_m	solute concentration at the membrane surface, [$mol\ m^{-3}$]
C_p	solute concentration in the permeate, [$mol\ m^{-3}$]
d_s	solute Stokes diameter, [nm]
d_p	pore diameter, [nm]
D_s	diffusivity of solute molecule in a dilute solution, [$m^2\ s^{-1}$]
DG	diethylene glycol
$DMAc$	N, N - Dimethylacetimide
ID	inner diameter, [mm]
IEP	isoelectronic point
J_s	solute or ion flux, [$mol\ m^{-2}\ s^{-1}$]
J_v	permeate volume flux, [$m^3\ m^{-2}\ s^{-1}$]
k	Boltzmann's constant, [$1.38 \times 10^{23}\ J\ K^{-1}$]
k'	mass transfer coefficient, [$m\ s^{-1}$]
L_p	pure water permeability, [$m^3\ m^{-2}\ s^{-1}\ bar^{-1}$]
$MWCO$	molecular weight cut off, [Da]
NMP	N-methyl-2-pyrrolidone
OD	outer diameter, [mm]
P	solute permeability, [$m\ s^{-1}$]
PBI	polybenzimidazole
PES	polyethersulfone
PVP	poly(vinyl pyrrolidone)
PWP	pure water permeability, [$liter\ m^{-2}\ hr^{-1}\ bar^{-1}$]

pK_a	ionization equilibrium constant, [-]
Q	water permeation volumetric flow rate, [m^3 hr^{-1}]
r_p	pore radius, [nm]
r_s	solute stokes radius, [nm]
Re	Renolds number, [-]
R_{obs}	observed solute rejection, [-]
R_T	real solute rejection, [-]
Sc	Schmidt number, [-]
S_D	steric hindrance factor diffusion, [-]
S_F	steric hindrance factor for permeation flow, [-]
Sh	Sherwood number, [-]
T	absolute temperature, [K]
u_f	linear velocity of feed solution, [m s^{-1}]

α	transport number of cation in free solution defined as D$^+$/(D$^+$ + D$^-$)
ΔP	trans-membrane pressure, [bar]
η	ratio of solute diameter to pore diameter d_s/d_p, [-]
φ	elongational draw ratio, [-]
μ	solvent viscosity, [N s m^{-2}]
μ_s	geometric mean diameter of solute at $R_T = 50\%$, [nm]
ξ	ratio of effective charge density (ϕX) to the electrolyte concentration at the membrane surface (C_m), [-]
π	osmotic pressure, [Pa]
σ	reflection coefficient, [-]
σ_g	geometric standard deviation about μ_s, [-]
σ_p	geometric standard deviation about μ_p, [-]
ϕX	effective charge density, [mol m^{-3}]
ω	the solute permeability [mol cm^{-2} s^{-1} Pa^{-1}],

CHAPTER ONE

INTRODUCTION

1.1 Development of Polymeric Membrane for Liquid Separation

In biology, a membrane is defined as a very thin envelope that surrounds and protects a cell. It controls the exchanges between the cell and the exterior environment: the membrane allows the passage of certain substances and prevents the passage of others. In the industry, membranes, which are bundled into modules to form an operation unit, are selective barriers that can be used to separate fluid mixtures, e.g., liquids or gases, into two parts with different compositions. The membrane, as an interface between the two bulk phases, can be a homogeneous phase or a heterogeneous collection of phases [Winston Ho & Sirkar, 1992]. Membrane-based separations are energy efficient and cost effective compared to traditional separation processes [Mulder, 1996]. Membrane technology, important for non-thermal separation, has become more attractive to avoid thermodynamically imposed efficiency limitations on heat utilization [Koros, 2004]. The driving force for membrane separation is a chemical potential difference between the two separated phases. This potential difference can result in pressure difference, concentration difference, and electrical potential difference or any combination of these variables. The driving forces are often used to classify membrane processes.

Membrane processes for liquid separation that use pressure difference as a driving force can be subdivided into four categories, i.e., microfiltration (MF), reverse osmosis (RO),

nanofiltration (NF) and ultrafiltration (UF). Separation of fluids by size exclusion through these four processes is primarily dependent on the pore size and pore size distribution of the membrane. Pores can be classified according to their sizes, as listed in Table 1.1. For ultrafiltration membranes, the pores on the surface are in the range of 1 ~ 100 nm. They are generally applied to micro-emulsion oil removal, biomolecule and virus separation from aqueous streams. The morphology and the separation performance of ultrafiltration membranes are mainly determined by the fabrication conditions.

Table 1.1 Membrane Separation Processes and Membrane Characteristics

Membrane Process	Separation Mechanism	Nominal pore size or Intermolecular Size (Å)	Transport Regime
Microfiltration	Size exclusion	500-50000	Macropores
Ultrafiltration	Size exclusion	10-1000	Mesopores
Nanofiltration	Size exclusion Electrical exclusion	5 - 20	Micropores Molecular
Reverse Osmosis	Size exclusion Solution/diffusion	<5	Micropores Molecular

Membranes either have a symmetric (isotropic) or an asymmetric (anisotropic) structure. Symmetric membranes have a uniform structure throughout the entire membrane thickness, whereas asymmetric membranes have a gradient in structure. The separation performance of asymmetric membranes is determined by their entire structure, which the relatively dense skin primarily controls separation and the porous part underneath the skin supplies as the mechanical support. The membrane structure can be controlled by adjusting thermodynamics and kinetic parameters involved in the formation process [Pinnau & Freeman, 1999]. Commonly used ultrafiltration membranes can be produced

from ceramic and polymeric materials. Compared to ceramic membranes, polymeric membranes are preferrable in the mild environment for their higher productivity and flexibility in the application. The majority of polymeric membranes are prepared by the controlled phase separation of homogeneous polymer solutions into two phases: one with higher polymer concentration, and one with lower polymer concentration. The concentrated phase solidifies shortly after phase separation, and forms the membrane. This method is called the phase inversion. The performance of the resulting membrane depends largely on the morphology formed during phase separation, and on subsequent (or almost simultaneous) solidification. Phase inversion can be induced in several ways. There are four main techniques for the preparation of polymeric membranes by controlled phase separation: thermally induced phase separation (TIPS); air-casting of a polymer solution; precipitation from the vapor phase of non-solvent; and immersion precipitation in non-solvent bath [Strathmann & Kock, 1977].

Generally, polymeric ultrafiltration membranes are fabricated from an initially thermodynamically stable polymer solution through phase inversion technique via immersion precipitation. Since Leob and Sourirajan invented the first flat integrally skinned asymmetric cellulose acetate membranes used for reverse osmosis in late 1960's [Leob & Sourirajan, 1963], Mahon [1966] made the first mention of hollow fiber membranes in his patents. From then on, synthetic polymeric membrane technology obtained much attention from both academia and industry for its potential application in separation processes. Membranes with different morphologies can be obtained depending on the thermodynamics parameters involved, as well as, on the kinetics of precipitation of

polymer solution. The mechanisms of nucleation and growth and the spinodal separation have been widely used to describe liquid-liquid phase separation evolution [Cahn, 1965].
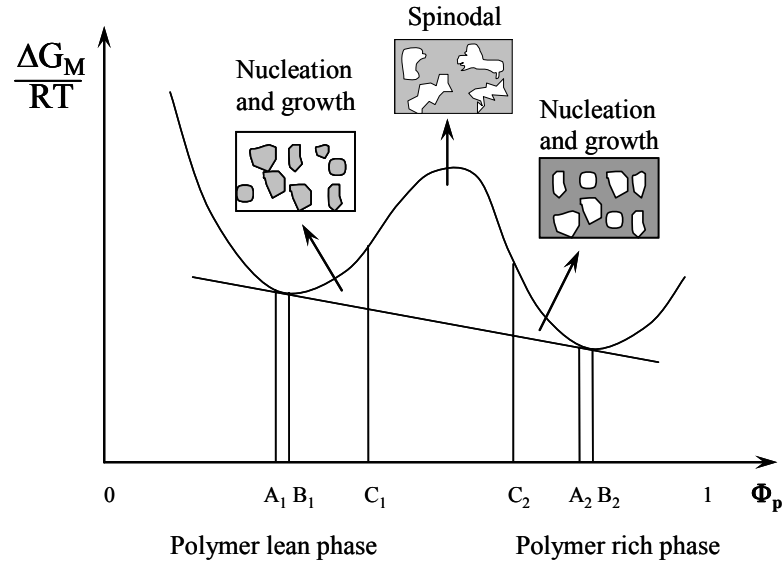
Fig. 1.1 Schematic of Gibbs free energy gradient as a function of polymer concentration

Flory–Huggins theory is typically used to describe the thermodynamic behavior of polymer/solvent/non-solvent system through considering change of the Gibbs free energy [Flory, 1942]. According to Figure 1.1, it represents the free mixture Gibbs energy gradient as a function of polymer solution composition. When a concentrated polymer solution ($\Phi_p > B_2$) changes its composition to the metastable region, where Φ_p varies in the range $B_2 \sim C_2$, a nucleus is formed with polymer lean phase ($\Phi_p = A_1$). On the other hand, when a diluted polymer solution changes its composition to the metastable region, where Φ_p varies in the range B_1-C_1, a nucleus of polymer rich phase is formed ($\Phi_p = A_2$). These nuclei grow due to the mass transfer with the surrounding phase. This mechanism is known as nucleation and growth. When the nuclei formation is not favored, the

polymer solution concentration goes into the unstable region, where Φ_p varies in the range $C_1 \sim C_2$. The liquid-liquid separation takes place, but the nuclei are not formed. This mechanism is called spinodal separation.

A typical isothermal ternary phase diagram is illustrated in Figure 1.2. The phase diagram can be divided into three regions (i) the stable region, located between the polymer/solvent axis and the binodal line, (ii) the metastable region, located between the bimodal line and spinodal line, and (iii) the unstable region, located between the spinodal line and the non-solvent/solvent axis [Pinnau, 1991]. By the penetration of non-solvent, the polymer solution becomes visually turbid and separates into two conjugative liquid phases at equilibrium, forming the binodal curve. Physically, the tie lines describe phase equilibrium between two phases, which means the chemical potentials in two phases have to be equivalent for each species. The spinodal line represents the situation where all possible concentration fluctuations lead to instability, and phase separation occurs spontaneously. For a ternary system, the binodal line and the spinodal line meet at the critical point. The location of critical point determines whether the polymer-rich phase and polymer-poor phase forms a new phase. In the metastable region between spinodal and binodal lines, small perturbations will decay, and phase decomposition can only happen when there is a sufficiently large perturbation. Within the spinodal curve, any small perturbation will cause phase separation of the system.

In the immersion precipitation process, a homogeneous polymer solution is cast on a suitable support or extruded through a die, and then immersed in a coagulation bath

containing a nonslovent. The nonsolvent begins to diffuse into the polymer solution and the solvent begins to diffuse into coagulation bath, bringing the composition of the polymer solution into the miscibility gap of ternary phase diagram. Hence, the polymer solution is decomposed into two phases: a polymer-rich phase and a polymer-lean phase. The location of the critical point determined whether the polymer-rich phase and the polymer-lean phase forms a new phase. At a certain stage during phase demixing, the polymer-rich phase is solidified into a solid matrix by crystallization or vitrification, while the polymer-poor phase develops into the pores [Wijmans & Smolders, 1986].
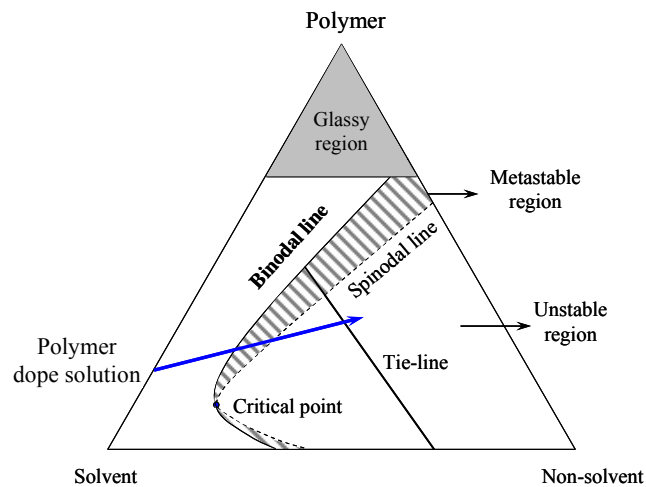
Fig. 1.2 Schematic of an isothermal phase diagram for a ternary polymer/solvent/non-solvent system as a function of composition

Upon the kinetics of process, liquid-liquid phase separation may proceed in two different ways, the nucleation and growth of new phases or spinodal decomposition. It is suggested that the formation of a skin layer and gelation of pore walls in the sublayer of microporous membrane was attributed to the mechanism of aggregate formation in the

polymer-poor phase [Broens et al., 1980]. Slower phase separation generally proceeds through a nucleation and growth mechanism, resulting in a closed membrane structure. Spinodal decomposition is considered as a near instantaneous process that creates an interconnected network of polymer rich and lean phases [Koros & Fleming, 1993]. This allows for a microporous substructure that is interconnected to support large trans-membrane pressure drops. However, the formation of skin layer is still a very complicated process. During the wet phase inversion, after the onset of liquid-liquid phase separation, a higher local polymer concentration in the outermost region is the ultimate determining factor for the formation of skin layer [Smolders, 1980].

Nowadays, several membrane configurations can be available for liquid separation. For example, spiral-wound modules generally have high packing density and low cost while require extensive feedwater pretreatment and have a high fouling potential. Tubular membrane modules are fouling resistant, and can be backflushed but have low packing densities and are expensive [Frank et al., 2001]. In comparison to flat sheet membranes, the hollow fiber configuration is a favorite choice for modules in membrane separation because of the following advantages: 1) a much larger membrane area per unit volume of membrane module, and hence resulting in a higher productivity; 2) self mechanical support which can be back flushed for liquid separation and 3) good flexibility and easy handling during the module fabrication and in the operation [Chung et al., 2000]. Nowadays, hollow fiber membranes are widely used in the membrane separation fields including gas separation, reverse osmosis, ultrafiltration, pervaporation and dialysis. Ultrafiltration membranes can be put into the separation process directly, and can be also

applied as porous support to make other kinds membranes through coating the surface with polymeric materials.

However, the hollow fiber spinning process, where a pressurized viscous polymer solution is extruded from a complicated channel within a tube-orifice spinneret, is much more complex than the casting process of flat sheet membranes. This is due to the fact that the rapid phase inversion kinetics and the interfacial mass transfer during the spinning process, as well as the structure and dimensions of the spinneret, viscosity and other properties of the dope, dope flow rate, quench conditions (temperature and composition) of internal and external coagulants, bore fluid flow rate, air gap length and humidity, fiber take-up speed play important roles on membrane morphology and separation performance. These parameters will influence the morphology and the separation performance of the resultant hollow fiber membranes. Although the principle of membrane formation (phase separation process) is independent of the membrane configuration, the shear stresses and elongational stresses suffered in preparing flat sheet membranes are very low as compared to those in fabricating hollow fibers as shown in Figure 1.3 & 1.4.
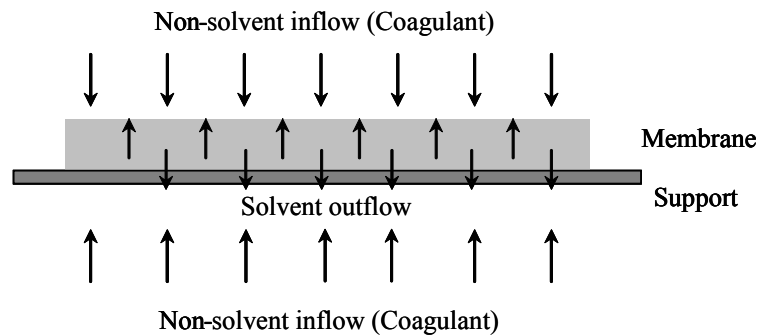
Fig. 1.3 Solvent/non-solvent exchange during fabrication of flat sheet membrane
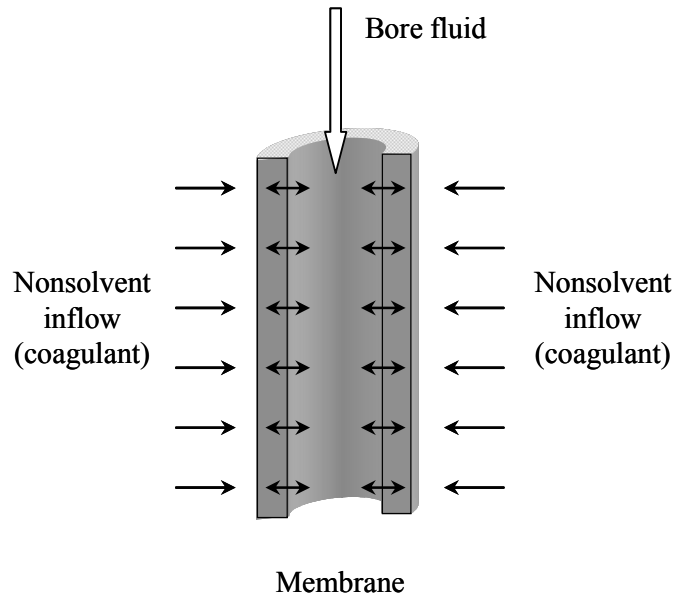
Fig. 1.4 Solvent/non-solvent exchange during fabrication of hollow fiber membrane

Usually, a spinneret consists of a reservoir and an annular channel which has a high L/ΔD (annulus length/flow gap) ratio. When a viscous polymer solution extrudes through the channel within a spinneret, it will be subjected to various stresses, such as shear stress induced by shear rate, which may influence the macro-molecular chain orientation and packing, thus subsequently affecting fiber formation, morphology and separation performance [Cabosso et al. 1976]. Membrane researchers had recognized that the dope rheological behavior induced by shear rate within the spinneret plays a very important role in the process of hollow fiber membrane formation. Chung et al. [2000] focused on studying the effect of shear rate on properties of hollow fiber UF membranes while Aptel et al. [1985] studied the effect of dope extrusion rate on properties of polysulfone hollow fiber UF membranes by the dry-jet wet spinning process. They reported that the obtained

water permeability of hollow fibers decreased and the rejection increased with an increase in the shear rate because the molecular chain orientation was introduced during the spinning. Porter [1990] reported that a tighter fiber with lower permeability and higher rejection were produced as the spinning solution velocity increased because of the alignment of polymer molecules under shear stress in the flow direction. He concluded that the pores in the skin would be elongated as a result of the alignment of polymer chains when spinning solution velocity increased. Ismail et al. [2003 & 1997] have systematically investigated the effect of shear rate on morphology and properties of hollow fiber membranes for gas and liquid separations. They demonstrated that the orientation induced by shear stress within the spinneret could be frozen into the wet-spun fibers and might be relaxed in the air gap region.

In view of complexity of the phase inversion process, the structure of the resultant hollow fiber membranes is strongly related to the composition of polymer dope solution, the bore fluid solution and the spinning conditions. Much research has demonstrated that the formation of asymmetric membrane structure can be controlled by both the thermodynamics of the polymer solution and the kinetics of the transport process. Generally, two kinds of microstructures can be formed during phase inversion process: sponge-like macrovoids which are induced by instantaneous demixing and finger-like macrovoids, which are induced by delayed demixing [Reuvers et al., 1987]. The origins of macrovoids formation in the cross-section of phase-inversion membranes have been often studied and seriously debated. Several researchers believed that it originates from the thermodynamic aspects of chemical potential gradient [Cohen et al. 1979]; others

suggested that it starts from local surface instability, material and stress imbalance, which induce solvent intrusion and capillary flow [Levich et al. 1969]. Other mechanisms such as Marangoni effects [Levich et al. 1969] and reverse osmosis effects [McKelvey et al. 1996] have also been proposed.

The presence of macrovoids caused by fast precipitation kinetics in the coagulation bath lowers the mechanical properties of the membrane and may lead to defects in the selective layer (as to gas and vapor separations applications). For some applications, a small number of macrovoids developed under the skin in asymmetric membranes can enhance their permeability without sacrificing the selectivity of the membrane. However, when operated under high pressures, finger-like macrovoids in asymmetric hollow fibers are undesirable because they are weak mechanical points which usually result in membrane failure at high pressures. Ways to reduce finger-like macrovoids or to modify the phase-inversion conditions to yield sponge-like structures have been studied. These may consist of 1) using high polymer concentration solutions [Kesting and Fritzsche, 1993]; 2) the addition of high viscosity components [Liu et al., 2003; 3) the addition of surfactants [Tsai et al., 2000; Tsai et al., 2001]; 4) the induction of delayed demixing [Kim et al., 2001] or gelation [Lin et al., 2002] and 5) spinning at high shear rates [Ren et al., 2002]. These different approaches can adjust the mass transfer process between solvents and non-solvents during polymer coagulation when the dope polymer solution contacts coagulant.

Rheological properties of polymer solution, which are correlated with shear flow induced

by shear stress within the spinneret and elongation flow induced by elongational stress (gravity and drawing force) in the air gap and/or the coagulant bath, have effects on the polymer molecular chain conformation and induced molecular orientation in the skin layer during the phase inversion process of hollow fiber formation. Chung et al. [1998] found that the hollow fiber membranes spun at high shear rate had a lower flux but a higher selectivity for gas and liquid separation. Likewise, Ismail et al. [1997 & 2003] observed that the molecular orientation and the gas selectivity were enhanced with an increase in shear rate. Idris et al. [2003] also suggested that extrusion shear was linked indirectly to phase inversion through induced molecular orientation and affected the subsequent dry/wet precipitation in the spinning process. Moreover, Qin et al. [2001] observed that the molecular orientation induced at the outer skin of the nascent fiber by shear rate could be frozen in the wet spinning process but it is relaxed in the dry–jet wet spinning process.

Compared to the dry–jet wet spun hollow fibers, wet spun hollow fiber membranes showed low flux and high separation performance. As for the elongation in the air gap, Paul [1969] reported that the molecular orientation correlated very well with the draw-ratio in wet-spinning process during fiber formation; and Ekiner and Vassilatos [2001], Cao et al. [2004] observed that an increase in draw-ratio or elongation strain resulted in denser morphology and higher gas selectivity. It is clear that dope rheology strongly affects the performance of hollow fiber membranes. Increasing shear rate and elongational rate can therefore strengthen the macromolecular orientation along the spinning direction and the packing density of polymer molecules, and then subsequently

modify the structure of membranes. As a result, the hollow fiber spinning process not only affects the structure but also the separation performance of the fabricated membranes.

Although the formation of finger-like macrovoids can be reduced through adjusting the interaction between polymer solution and coagulation medium by changing the composition of polymer solution, bore fluid and the coagulant agent, there are some limitations to polymer solutions which cannot satisfy all the requirements for eliminating finger-like macrovoids. All the above studies were based on the hollow fiber membranes spun by the straight annular spinneret. Different designs of the spinneret will influence fluid dynamics when polymer solution flows though the channel inside spinneret. However, there has been no report on the effects of conical spinneret on ultra-filtration hollow fiber spinning. Since in the channel of conical spinneret, the radial flowing will influence the chain packing of macromolecules further and subsequently the morphology of membranes. Therefore, the study and design of conical spinneret are needed since the hollow fibers spun from conical spinneret may have potential application in industry. As a result, under a specific composition of the polymer solution, whether finger-like macrovoids can be eliminated completely through increasing the shear rates and elongational rates during hollow fiber spinning is still needed to be studied systematically.

1.2 Development and Application of Nanofiltration Membranes

Nanofiltration is a recently developed pressure-driven process in the membrane separation. It seems that Eriksson is one of the first authors using the terminology "nanofiltration" explicitly in 1988. Since then this term has been introduced to indicate a specific domain of membrane technology between ultrafiltration and reverse osmosis since NF membrane is supposed to be a very loose reverse osmosis membrane or a very tight ultrafiltration membrane with respect to its permeate flux and separation performance, as shown in Fig. 1.5. Nanofiltration membranes have received their name as they have nominal molecular weight cut-offs (MWCO) from 200 to 1000 Daltons for uncharged molecules such as sugars (glucose, sucrose, lactose), corresponding to having pores of about 0.5~2 nm in diameter. In many applications NF has replaced reverse osmosis due to lower energy consumption and high flux rate [Raman et al., 1994].

Most commercial NF membranes are typically negatively or positively charged by the dissociation of surface functional groups such as sulphonic or carboxyl acids or the adsorption of ions on the membrane [Petersen, 1993]. These characteristics of NF membranes allow solutes to be separated by a combination of the size sieving, electrical interaction between ions and the membrane surface charge. Therefore, nanofiltration is of special interests in applications where fractionation of charged molecules or selective desalination is required. Nanofiltration membranes can be used to separate or adjust the ratio of mono- and multi-valent ions. Major applications of nanofiltration include removal of hardness and dissolved organics from water [Watson & Hornburg, 1989],

Micrometers (Log Scale)	Ionic Range	Molecular range	Macro molecular range	Micro particle range	Macro particle range	
		Scanning Electron Microscope		Optical Microscope	Visible to naked eye	
		0.001 0.01	0.1	1.0 10	100 1000	

Angstrom Units (Log Scale)	10	100	1000	10^4	10^5	10^6	10^7

Relative size of common materials

Carbon Black   Paint Pigment   Human hair

Endotoxin/Pyrogen   Yeast cells   Beach sand

Metal Ion   Synth. Dye   virus   Bacteria   Mist

Tobacco Smoke   Coal Dust

Gelatin   Red Blood Cells   PinPoint   Granular Activated Carbon

Sugars   Colloid Sillica/Particles   Blue Indigo Dye   Pollens

Atomic Radii   Albumin Protein

Latex/Emulsion

Asbestos   Milled Flour

Separation Processes

Reverse Osmosis   Ultrafiltration   Particle Filtration

Nanofiltration   Microfiltration

Fig. 1.5 Classification of separation process according to size of solutes [Donnelly et al., 1998]

arsenic removal from drinking water [Urase et al., 1998; Vrijenhoek, & Waypa, 2000; Saitúa et al., 2005], removal of highly colored lignin and chlorinated lignin derivatives arising from bleaching of wood pulp [Bindoff, 1987], demineralization in the dairy industry [Horst et al., 1995], removal of small organic molecules in organic synthesis membrane reactor [Whu et al., 1999], heavy metal ions recovery from electroplating wastewater [Hafiane et al., 2000; Mohammed et al., 2004] and tannery wastewater [Cassano et al., 1996], purification of drug derivative from concentrated saline solutions [Capelle et al., 2002] and especially in the purification and separation of pharmaceuticals from fermentation broths [Christy & Vermant, 2002].

Pharmaceutical synthesis results frequently in crude reaction mixtures containing both organic compounds of different molecular weights and inorganic salts in an aqueous system. These mixtures can be formed when mineral acids or bases are involved as catalysts or neutralization agents during the reaction [Luthra et al., 2001; Capelle et al., 2002]. The subsequent purification is usually straightforward since mineral salts can precipitate in organic solvents and organic molecules are extracted by solvents or/and salted out from water. It is more difficult to deal with mixtures in water when the interesting organic molecule is hydrophilic, that is completely (at least highly) soluble in the aqueous media.

Moreover, some organic syntheses of bulk drug generally involve multi-step reactions where each reaction may be carried out in a different organic solvent. The isolation of the drug is often carried out in a solvent different from the solvent used in the reaction. The

overall objective is to maximize the product yield and minimize the impurity. Most reactor streams in pharmaceutical manufacturing contain thermally labile, high molecular weight (250~1000Da) product of interests along with other large and small molecular weight by-products, residual reactants and the solvent [Paul & Rosas, 1990]. The product (intermediate or final) must be separated from other species and the current solvent, because the subsequent reaction often cannot tolerate the previous solvent as an inert impurity beyond a certain concentration. Conventional separation processes (e.g. distillation) require special conditions (e.g., high vacuum) to handle thermally labile products and extraneous chemicals to affect separation, while athermal membrane processes for such separation would be highly feasible. Organic solvent-resistant membranes are particularly considered since they can selectively retain solutes with molecular weights greater than 250Da and simultaneously allow the smaller molecules to wash out along with the organic solvent at ambient temperature. Nanofiltration has been employed in the process of athermal solvent exchange from one organic synthesis step to the next step [Goulas et al., 2002].

Antibiotics are clinically useful because they are highly effective against microorganism with minimal toxicity to people. Antibiotics are mainly produced by fermentation, and are harvested from the broths by selective solvent extraction and concentrated by vacuum distillation. Membrane separation processes may have an improved efficiency and reduced operating cost in comparison with the traditional concentration processes.

NF can be used to recover the antibiotics from broths. There are two methods of

recovering antibiotics from broth: (i) adjusting the pH and the temperature of broth, removing water and inorganic salts by using hydrophilic NF membranes, concentrating the solution to near the maximum solubility, then extracting the antibiotics with minimal solvent. At the same time, low molecular weight organics and salts are washed out in the permeate; (ii) extracting the antibiotics with solvent, and then concentrating the solution with hydrophobic NF membranes. The transferred solvent can be recovered.

Studies on the concentration of antibiotics by NF processes are still at the beginning stage. Sheth et al. [2002] employed solvent-resistant NF membranes MPF-50 and MPF-60 to exchange the solvent methanol for ethyl acetate through nanofiltration-based diafiltration in the solution of erythromycin, an active intermediate of a kind of widely used broad-spectrum macrolide antibiotics. Zhang et al. [2003] prepared composite membranes for NF by the interfacial polymerization of piperazine and trimesoyl chloride. Some of the prepared membranes were coated with polyvinyl alcohol (PVA) to improve the hydrophilicity and smoothness of the membrane surface to decrease the membrane fouling. The membrane was used to concentrate the solution of antibiotics whose molecular weight is in the range of 800~1000Da, both in laboratory and pilot plant scales. The rejection coefficient of antibiotics could be maintained at higher than 99% constantly, while the permeate flux decreased due to the increase in feed concentration.

1.2.1 Nanofiltration separation mechanisms

The transport of the solute and the solvent through nanofiltration membranes is caused by

the chemical potential gradient between the two phases separated by the membrane. The selectivity of NF membranes is based on both the size and charge of solutes. Therefore, the transport and separation processes in NF membranes may be explained by a combination of at least three mechanisms, the solution-diffusion process, the sieving mechanism and electrostatic interactions between electrically charged ions and the charged membrane surface. The solute transfer is basically understood as being the result of the two following steps: first, a distribution of ionic species at the selective interface according to their charge; second, transfer by a combination of diffusion/convection/ electrophoretic mobility through the membrane.

Uncharged organic molecules are rejected by the sieving mechanism, based on the small pore size of the membrane. The membranes are often characterized by the molecular weight cut-off (MWCO) defined as the molecular weight of a molecule which is 90 % retained. Rejection coefficient is calculated using the following equation:

$$R = (1 - \frac{C_p}{C_f}) \times 100\% \qquad (1.1)$$

where C_p and C_f is the concentration of the solute in the permeate and the feed solution, respectively.

However, this parameter of MWCO gives only a rough estimate of retention characteristic of a membrane for uncharged molecules. Moreover, molecular weight cannot represent the geometry of the molecule and it does not provide information on the retention for molecules having a molecular weight below the MWCO.

The rejection of charged molecules and especially simple ions is influenced by the inherent negative charge of the membrane. This kind of ion-selective membrane has unequal ion distribution across the membrane with solutions containing different free ions. If an ion-exchange membrane in contact with an ionic solution is considered, then ions with the same charge as the fixed ions in the membrane are excluded and cannot pass through the membrane, and the transport rates of solutes will change as ion concentrations change. This effect is well known as Donnan exclusion [Donnan, 1995]. In the mixture of electrolytes with a common permeable counter ion and two co-ions, which are the totally rejected and the permeable ion, respectively, Perry and Linder [1989] gave detailed explanation of negative salt rejection in terms of the Spiegler-Kedem analysis by introducing the Donnan exclusion correction. For the case of electrolyte mixture Na_2SO_4 and $NaCl$, the membrane preferentially rejects SO_4^{2-} ions over Cl^-, and the rejection decreases as the concentration of Na_2SO_4 increases. To maintain electro neutrality, Na^+ must also permeate through the membrane. Moreover, at high concentration of SO_4^{2-}, the rejection of Cl^- can even be negative [Tsuru et al., 1991].

Afronso and Pinho [2000] reported the transport flux of $MgSO_4$, $MgCl_2$ and Na_2SO_4 across the NF membrane, the effect of the anion valence and the feed concentration on the salt rejections. They found that the order in salt rejection was $R_{MgCl_2} < R_{MgSO_4} < R_{Na_2SO_4}$, and an increase in the salt concentration leads to a decrease in the rejection. These two facts which are typical of electrically charged membrane are qualitatively in agreement with the ion exclusion principle. The lower rejection of $MgCl_2$ than $MgSO_4$ corresponds to the decreasing order of the anion charge density, i.e. the anion repulsion forces become

progressively weaker, while the lower rejection of $MgSO_4$ than Na_2SO_4 corresponds to the increasing order of the cations charge density.

When the concentration in the feed is low and the concentration of the fixed charge is high, the Donnan exclusion is very effective. However, with an increase in the feed concentration, this exclusion becomes less effective because the cation's shield effect on the membrane's negatively charged groups becomes progressively stronger, leading to the decrease of the membrane repulsion forces on the anions. This effect is more evident for the chloride ion than for the sulphate ion, since the latter has a higher charge density, and therefore is rejected by the membrane even at high concentrations.

At present, the only well established non-sieving mechanism of nanofiltration is the Donnan exclusion of co-ions, due to their interactions with fixed electric charges [Bowen et al., 1999; Bowen & Welfoot, 2002]. Counter-ions in binary electrolytes are transferred stoichiometrically owing to the zero electric current condition. Therefore, a salt as a whole will be rejected. The Donnan exclusion is marked by a characteristic dependence of rejection on the electrolyte valance type, an increase with the increasing co-ion charge and a decrease with the increasing counter-ion charge.

Yaroshchuk [2001] proposed a non-steric mechanism of nanofiltration by superposing the Donnan and dielectric exclusion for non-symmetrical binary electrolytes and their mixtures when they are in neutral and charged pores. The dielectric exclusion (DE) occurs due to the interactions of ions with polarized interfaces between media of different

dielectric constants. If an ion is located in the medium of a higher dielectric constant (water or other polar solvent), it induces an electric charge of the same sign as its own in the medium of a lower dielectric constant (polymeric or inorganic membrane matrix). Hence, a repulsion and exclusion of ions arise from membrane pores, in contrast to the Donnan exclusion where co-ions are excluded but counter-ions are pulled in the pores. The exclusion energy is proportional to the square of the ionic charge and both cations and anions are excluded from pores because the polarization charge is proportional to that of the ionic charge. No extra assumption is necessary about the change in dielectric properties of solvent in the pores. The dielectric exclusion is a universal phenomenon caused by ubiquitous differences in the dielectric constants of polar solvents and membrane matrix. It is found that the combinations of dielectric and Donnan exclusions, with different extents of contribution of each of them, may explain qualitatively the dependencies of salt rejections on the salt valence type observed with different NF membranes.

1.2.2 Nanofiltration separation models

The presence of acidic/basic functional groups on the NF membrane surface induces surface charge distributions, which govern the separation performance. Most models for ionic transport in NF membranes are based on either the thermodynamic of the theory of irreversible processes (TIP) or the extended *Nernst–Planck* equation. So far, several models were established to characterize and predict rejection and transport performance of NF membranes quantitatively, which include the irreversible thermodynamic model

[Spiegler & Kedem, 1966], fixed charge model [Hoffer And Kedem, 1967], space charge model [Bowen et al., 1999], steric-hindrance pore (SHP) model [Nakao & Kimura, 1982], electrostatic and steric-hindrance (ES) model [Yaroshchuk & Vovkogon, 1994], Donnan-Steric pore model [Wang et al., 1997; Mohammad, 2002] and so on.

(i) The irreversible thermodynamic model

The transport phenomena of UF, NF and RO membranes in pressure-driven processes can be described by the theory of irreversible thermodynamics. Spiegler and Kedem [1966] proposed to describe the volume flux (J_v) and the solute flux (J_s) passing through a membrane by the following equation:

$$J_v = L_P(\Delta P - \sigma \cdot \Delta \pi) \tag{1.2}$$

$$J_s = P \cdot (c_f - c_p) + (1 - \sigma) \cdot J_v \overline{c} \tag{1.3}$$

where L_p, σ, P are the membrane parameters called pure water permeability, reflection coefficient, solute permeability, π and $\overline{c}$ are osmotic pressure and mean concentration over the thickness of membrane, respectively.

Because the membrane was assumed to act as a black box containing no description of ion transport, it was not possible to characterize the structural and electrical properties of the membrane with this model. This model is on the basis of solution-diffusion mechanism, where no pore size distributions are taken into account. However, the pore size distribution of the membrane should be a key element for the description of the retention of organic molecules. Bruggen et al. [1999], Bowen and Doneva [2000] and Bowen and Welfoot [2002] introduced pore size distribution in the NF model, combining

diffusion parameter and the experimental water flux through the membrane to calculate the retention as a function of the molecular weight and pressure.

This model assumes that the flux of each species is proportional to the driving forces acting on the system, but it only takes into account the diffusion and ion flux in the convection mechanisms. Besides, the fluxes linearity and the reciprocity relations between the phenomenological coefficients are not valid when the system deviates from the equilibrium condition, i.e. for high pressures or fluxes.

(ii) The steric-hindrance pore (SHP) model

Nakao and Kimura [1982] proposed the steric-hindrance pore model while studying the discrepancy of the kinetic item of σ between the fiction model and the pore model.

Through modification of the pore model by eliminating the wall correction factor, σ, P and L_p can be expressed by following equations:

$$\sigma = 1 - S_F[1 + (16/9)q^2] \tag{1.4}$$

$$P = \omega RT = D_s \cdot S_D \cdot (A_k / \Delta X) \tag{1.5}$$

$$S_F = (1-q)^2(1+2q-q^2) \tag{1.6}$$

$$S_D = (1-q)^2 \tag{1.7}$$

S_D and S_F are the steric hindrance factors for diffusion and filtration flow respectively, D_s is the diffusivity of solute, ω is the solute permeability (mol/cm^2 s Pa), A_k is the ratio of total cross-sectional pore area to effective membrane area, q is the ratio of the Stokes

radius of solute to the radius of membrane pore, i.e. $q = r_s / r_p$. Solute radius r_s can be obtained by the *Stokes-Einstein* equation [Einstein, 1956]:

$$r_s = \frac{kT}{6\pi\mu D} = \frac{RT}{6\pi\mu D N_A} \tag{1.8}$$

k and N_A are Boltamann's constant and Avogadro's number, μ is the viscosity of solution. The pure water permeation volumetric flux is expressed by *Hagen-Poiseuille's* law:

$$J_v = \frac{\varepsilon \cdot r_p^2}{8\mu\tau} \frac{\Delta P}{\Delta X} \tag{1.9}$$

The value of $A_k / \Delta X$ for different solute calculated by SHP model was almost constant, and agreed well with that determined from the pure water permeation. Upon these obtained parameters the permeate flux and rejection performance of nanofiltration system can be predicted.

(iii) The fixed charge model and the space-charge (SC) model

The space-charge (SC) model for a charged capillary was originally proposed by Osterle and co-worker [1968]. This model is a more realistic model to predict rejection performance of NF membranes through assuming a straight capillary having charge on its surface. Basic equations include the *Poisson-Boltzmann* equation for ion concentration and electric potential in the radial direction, the *Nernst-Planck* equation for ionic transport, and the *Navier-Stokes* equation for the force balance in narrow pores relative to pore length. The SC model assumes ions as point charges, so the steric effects of the size of ions are neglected. The Boltzmann distribution is assumed to calculate the radial distribution of ion concentration using electric potential and the axial concentration

which means so-called fictitious concentration inside the capillaries. The main disadvantage of SC model is that the numerical solution of equations is complex, even with simplifying assumptions, especially as the number of permeating species increases. Another disadvantage is the exclusion of steric and friction interactions in the process of derivation.

(iv) The electrostatic and steric-hindrance model (ES)

Wang et al. [1997] developed the electrostatic and steric-hindrance model (ES) to estimate the structural parameters (pore radius r_p and the ratio of membrane porosity to the thickness, $A_k/\Delta x$) of NF membranes on the basis of the SHP model with the permeation experiments of aqueous solutions of neutral solutes, and proposed a simple empirical equation to correlate the effective fixed charge density ϕX, instead of fixed charge density X, to the concentration of charged solutes based on TMS model. The experimental results indicated the charge density is dependent on the concentration of the solutes. The ES model assumed a charged porous membrane and the charged solutes. The charged porous membrane can be regarded as a bundle of capillaries with the pore radius r_p, the ratio $A_k/\Delta x$ and the pore surface charge density q_w. The charged solute can completely dissociate into 'large ions' and 'small ions', and only the steric-hindrance effect is considered for the large ions, which can be simulated as a rigid sphere of Stokes radius r_s and further related to their diffusivity in dilute aqueous solution by the *Stokes-Enstein* equation. The ES model also assumes that all ions can be treated as point-like and their concentration distributions within the membrane capillaries obey the *Possion-Boltzmann* equation, which can be calculated approximately by the Donnan equilibrium.

The ion flux inside the charged capillaries of the membrane can be expressed by the modified *Nernst-Planck* equation by considering the steric-hindrance effects. However, the ES model, similar to the SHP model, seems to be limited when the pore radius is near 0.5 nm for the membranes.

(v) The Donnan-Steric Pore Model (DSPM)

Bowen and Mukhtar [1996] formulated a hybrid model in which the extended *Nernst-Planck* equation was used to describe ion transport and the steric-Donnan equilibrium model was used to describe ion partitioning as if the membrane were homogeneous and non-porous, but at the same time hindrance factors for diffusion and convection were included to allow for the transport of ions within a confined space. The values of the hindrance factor, which depend on the ratio of ionic radius/pore radius, were calculated using numerical technique from the drag force exerted by the solvent when solutes move in the confined spaces, such as membrane pores [Bowen & Sharif, 1994]. This model predicted the rejection of solutes depending on the effective pore radius r_p, effective charge density X_d and effective ratio of membrane thickness to porosity $\Delta x / A_k$. This model assumes that the effective charge density accounts for activities inside the membrane and non-idealities caused by solute-solute and solute-membrane interaction. The dependence of the effective charge density on feed concentration was correlated with a Freundlich type isotherm. The model parameters were obtained by fitting the model to data from permeation experiments of uncharged solutes and single salts. This predictive model has proved to be very successful in describing relatively simple systems such as organic molecules and univalent electrolytes. However, the quality of agreement with
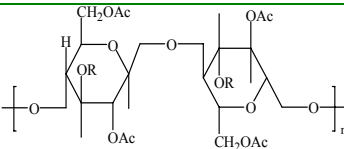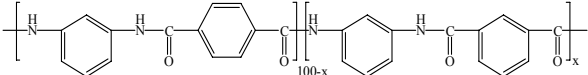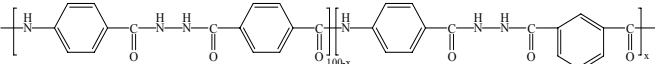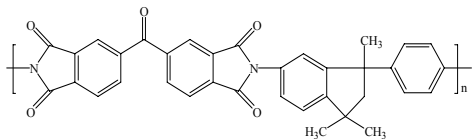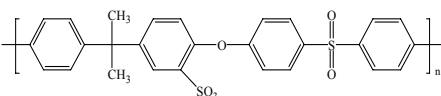
experimental data is worse in the rejection of multivalent cations such as Mg^{2+} [Shaep et al., 2001] and mixtures of electrolytes.

The exact mechanism of selective separation by NF membranes is still a matter of debate. These proposed hypotheses reflect the heterogeneity of the membrane's structure and composition (as tight ultrafiltration membrane and loose reverse-osmosis membrane). The separation properties are the consequence of the superposition of several mechanisms depending on the membrane structure.

1.2.3 Fabrication of nanofiltration membranes

Many hydrophilic polymer materials have been used to fabricate asymmetric nanofiltration membranes via phase inversion, as shown in Table 1.2[Schäfer et al., 2005].

Table 1.2 Polymer used to prepare asymmetric nanofiltration membranes

Polymer	Abbreviation	Chemical structure
Cellulose acetate (R = Ac) Cellulose acetate butyrate (R = Butyl)	CA CAB	
Polyamide	PA	
Pol(yamide-hydrazide)	PAH	
Polyimide	PI	
Sulfonated polysulfone	PSf-SO$_3$	

Brominated poly(phenylene oxide)	PPO-Br	
Poly(phthalazine ether sulfone ketone)	PPESK	
Sulfonated poly(phthalazine ether sulfone ketone)	(S)PPESK	
Sulfonated poly(ether ether ketone)	SPEEK	
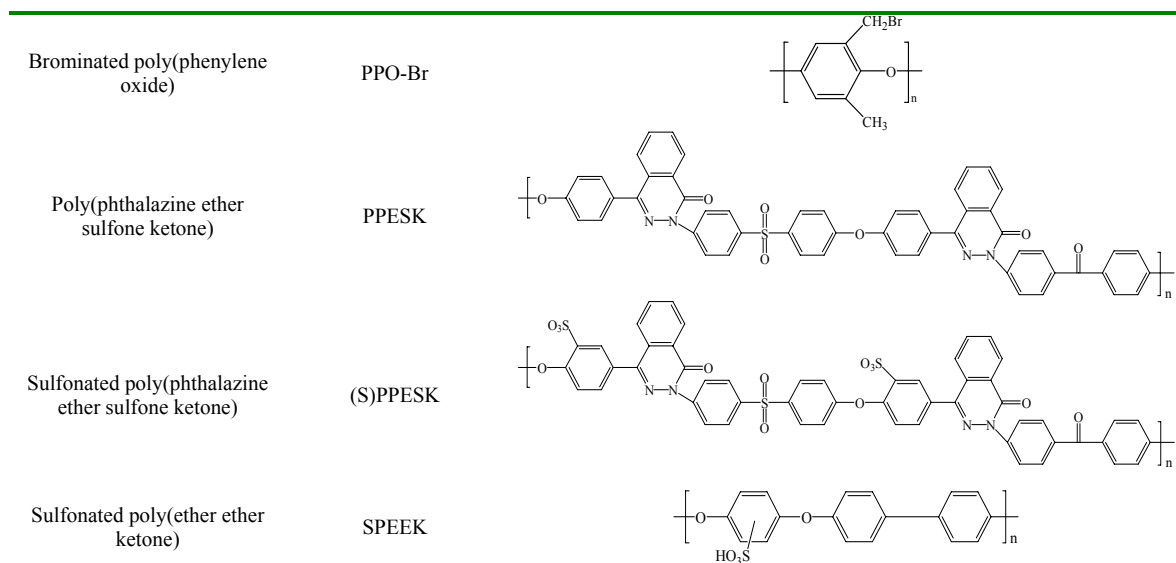
Most nanofiltration membranes are composite membranes which are made by spreading a thin layer on the porous asymmetric substrate by following methods:

- Coating
- In-situ polymerization
- Interfacial polymerization
- Plasma polymerization
- Radiation induced grafting
- Surface modification

Except for surface coating (dip, spray or spin coating), all these modification approaches involve polymerisation reactions which generate new materials as a very thin layer on the original membrane surface. Commercial nanofiltration membranes were not generally available until the late of 1980s although they were developed from the late of 1970s [Schäfer et al., 2005]. For example, interfacial polymerization reactions occur between two reactive monomers at the interface of two immiscible solvents to depositing a thin layer upon an ultrafiltration membrane, as shown in Fig. 1.6. The resultant NF membrane

29

had high MgSO$_4$ rejection (99%), and low NaCl rejection (< 60%). Table 1.3 lists the

major nanofiltration membrane producers and commercial membranes.
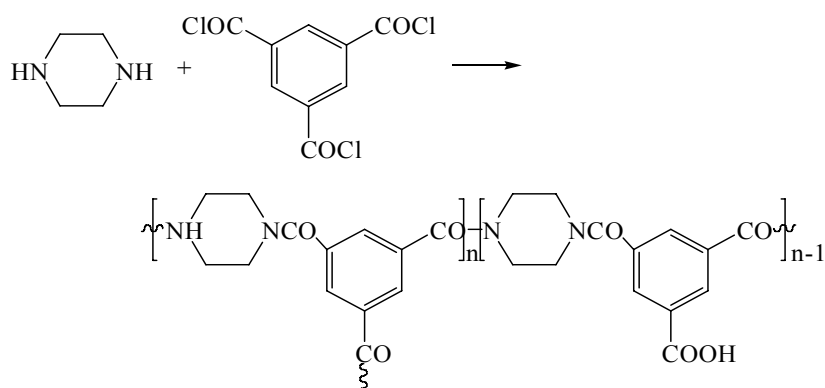
Fig. 1.6 Chemical reaction for fabrication of NS300 membrane from piperazine and trimesoylchloride [Petersen, 1993]

Table 1.3 Nanofiltration membrane manufacturers, materials and configuration

Membrane	Manufacturer	Membrane material	Charge (neutral pH)	Configuration
UTC-20	Toray	Polyamide	Positive	Flat sheet
NF40	Film-Tec (DOW)	Crosslinked aromatic polyamide	Negative	Flat sheet
NTR7450	Nitto-Denko	Sulfonated polyethersulfone	Negative	Flat sheet
NTR7410	Nitto-Denko	Sulfinated polysulfone	Negative	Flat sheet
NTR7250	Nitto-Denko	Polyvinyl alcohol	Negative	Flat sheet
Zirfon^R	Vito	Polysulfone with inorganic filler	Negative	Tubular
AFC-30	PCI	Polyamide	Negative	Flat sheet
Desal-5	Desalination systems	Composite	Negative	Flat sheet /spiral wound
NF 50, NF 70	Minneapolis, MN	Polyamide	Negative	Flat sheet /spiral wound
Nanomax 50	Millipore	Polyamide	Negative	Spiral wound
N30F NF PES10	Hoechst, Celgard, Germany	polyethersulfone- polyvinylpromidone	Negative	Flat sheet /spiral wound

1.3 Characterization of the ultrafiltration or nanofiltration membranes

Most porous ultrafiltration or nanofiltration membranes, either polymeric or inorganic, have a complex porous structure, with a set of pores with various sizes ranging from a few nanometers to several tens of nanometers which determines mass transport through membrane. There are several well established techniques for the determination of pore size and pore size distribution. They include the bubble point technique, mercury porosimetry, the microscopic approach, solute transport method, permporometry and thermoporometry [Cuperus, 1990].

AFM (atomic force microscope) can image the non-conducting sample without damaging the membrane. While SEM (scanning electron microscope) requires heavy metal coating for non-conducting sample and high beam energy which may damage polymeric membranes. However, average pore sizes obtained from SEM were smaller than those obtained by AFM due to the sample preparation. In addition, AFM images are distorted by convolution between pore shape and cantilever tip shape. Moreover, from SEM and AFM, the images can only give structure information on the membrane outer layer surface without pore inside morphology. This can be verified from the experimental results in which the mean pore sizes measure by AFM were about 3.5 times larger than those calculated based on the data from solute transport technique [Singh et al. 1998].

The porous structure can be represented by the apparent characteristics such as solvent and solute permeabilities since they are easily obtained from separation experimental

results. Therefore, the solute transport method can be used to learn more precise information about the porous structure of the membranes along with other instrumental analysis. Since the solute transport experiment is close to real separation process it can provide more information to predict separation performance of the membrane.

The charge property of nanofiltration membranes can be obtained from the rejection measurement of different salts, single salt rejection at different pH and different concentration, titration method and streaming potential measurement [Peeters, 1997].

1.4 Engineering principles for liquid separation membrane

Membrane science and technology have led to the significant innovation in both processes and products over a few decades, offering interesting opportunities in the design, rationalization, and optimization of innovative productions [Drioli & Romano, 2001]. They permit drastic improvements in manufacturing and processing, substantially decreasing the equipment-size production-capacity ratio, energy consumption, and/or waste production and resulting in cheaper, sustainable technical solutions [Strathmann, 2001]. Membrane operations show potential in molecular separations, clarifications, fractionations, concentrations, etc. in the liquid phase, in the gas phase, or in suspensions. Membrane operations make them ideal for industrial production: i) generally athermal and not involve phase changes or chemical additives, ii) simple in concept and operation, iii) modular and easy to scale-up, and iv) low in energy consumption with a potential for more rational utilization of raw materials and recovery and reuse of byproducts.

The chemical engineering of polymeric membranes for liquid separation can be fundamentally focused on (1) membrane material selection, (2) membrane fabrication procedures, (3) membrane characterization and evaluation and (4) membrane module design and separation performance. When designing a membrane system, the physical and chemical properties of the treated media should be firstly taken into consideration. Then, the material selection and the membrane fabrication procedure must be carefully identified. The chemistry of adopted materials along with the formation mechanisms occurring during membrane preparation will control the permeation flux and the separation efficiency of the resulted membrane.

Several elements determine the performance and applications of a membrane, namely, (1) pore size and pore size distribution, (2) thickness of the selective layer, (3) microstructure of the substrate layer, (4) intrinsic chemical and physical properties of the membrane materials and (5) cost. Pore size and pore size distribution usually determine membrane applications, separation factor or selectivity, whereas the selective layer thickness controls the membrane flux or productivity. Material's chemical and physical properties govern the intrinsic permselectivity for gas separation and pervaporation, fouling characteristics for reverse osmosis (RO), ultra-filtration (UF) and micro-filtration (MF) membranes, chemical resistance for membranes used in the harsh environments, and biocompatibility for biomedical membranes used in dialysis and tissue engineering.

Membrane material selection determines the physico-chemical interactions between the polymer and the permeate solvent or/and the dissolved solutes, the swelling of the

membrane by the solvent. Ideally the intrinsic properties of the liquid separation membrane materials should include (1) good chemical resistance (2) good mechanical strength (3) satisfactory thermal stability (4) fouling resistance (5) ease to recover (6) engineering feasibility (7) satisfactory manufacturing reproducibility and last but not least (8) low cost. It is of most importance that the polymer chosen must be highly permeable to the treated liquid solutions, which can efficiently minimize the total membrane area required; therefore the whole capital cost can be reduced.

1.5 Research Objectives and Project Organization

In Chapter One of this dissertation an overview is given of membrane development in the field of liquid separation, especially for ultrafiltration and nanofiltration. A brief introduction on the engineering principles of membrane liquid separation regarding the membrane material selection, membrane preparation, membrane characterization as well as the membrane module design and evaluation of membrane separation performance are presented. The nanofiltration mechanisms and solute rejection model are also summarized. The research objectives of this dissertation are given at the end of this chapter.

1.5.1 Objectives of Chapter Two

This thesis is divided to two parts based on their different objectives. The first part is focused on the fabrication and characterization of ultrafiltration hollow fiber membranes in Chapter two. The purposes of first part are mainly concentrated on two problems:

➢ How do the different flowing angles within the spinnerets affect the structure and the performance of the fabricated hollow fiber UF membranes?

➢ Is it possible to eliminate the finger-like macrovoids through increasing the shear rate or elongational rate during hollow fiber spinning?

This part will investigate the formation of finger-like macrovoids in ultrafiltration hollow fiber membranes which are spun from lower concentration polymer solution. The elimination of the finger-like macrovoids can make it possible for the fabricated hollow fiber membranes to sustain higher operating pressures, which can increase the process productivity and equipment efficiency together. Moreover, the research of effects of flowing angle within the spinneret on the structure and performance of the fabricated membrane will help us produce desirable hollow fiber UF membranes with reasonable permeate flux and separation performance. Although the result in this study can be applied to spinning other kinds of hollow fiber membranes (e.g. gas separation, reverse osmosis, pervaporation, nanofiltration, etc. from higher concentration polymer solutions, further research are still required since the property of different polymers and the concentration of polymer solution are other main parameters affecting the structure and performance of resultant membranes. This part also makes preparation for the fabrication of nanofiltration hollow fiber membranes (Chapter Five) which focus on the elimination of finger-like macrovoids. More specifically, this project addressed the following issues:

1. Effects of flow angle within the straight and conical spinnerets on the structure and the separation performance of the spun hollow fiber UF membranes;

2. Effects of spinning condition (wet spinning, dry jet-wet spinning, shear rate, elongational rate) on the structure, size and size distribution of the formed micropores on the surface of hollow fiber membranes; the mean effective pore size on the surface of membrane will be used to evaluate the formed micropores on the surface;

3. Effects of spinning condition (shear rate, elongation rate) on the formation of finger-like macrovoids during wet spinning and dry jet-wet spinning processes;

4. Effects of spinning condition (wet spinning, dry jet-wet spinning, shear rate, elongational rate) on the separation performance of hollow fiber membranes;

1.5.2 Objectives of Chapter Three to Five

The second part of this thesis (from Chapter Three to Chapter Five) is focused on the fabrication, characterization and application of nanofiltration membranes. Different methods have been employed to fabricate NF membranes by placing a thin active dense layer on the top of porous sublayer (asymmetric porous ultrafiltration support). In present, commercial nanofiltration membranes are only available in flat sheet pattern. Therefore, Chapter Three has systematically characterized two flat sheet composite nanofiltration membranes (NADIR$^{®}$ N30F and NF PES10) through measuring the rejection of neutral molecules and different electrolytes, the ion fractionation of binary salts mixtures; and investigated the feasibility of these two NF membranes for the separation of cephalexin over wide range of pH.

Chapter Four proposes a novel process for the preparation of PBI nanofiltration

membrane through chemically modifying the as-cast asymmetric PBI membrane with *p*-Xylylene dichloride. Since all NF membrane have their origins in reverse osmosis (RO) membranes and PBI was proved as potential material for membrane fabrication. The solute transport method is used to characterize the mean effective pore size and pore size distribution of the resultant membranes. The effect of solution pH on the membrane charge property and the separation performance to ions is discussed in detail. The modified membranes were applied to fractionate the binary electrolyte mixtures with same cation or anion. The feasibility of the modified PBI NF membrane for the separation of cephalexin over wide range of pH has been discussed.

Chapter Five explores a novel process to fabricate PBI NF hollow fiber membrane with appropriate charge characteristics by a one-step phase inversion process without post-treatment. The effects of bore fluid chemistry on the morphology and separation performance of PBI hollow fiber membranes were investigated. Characterization of the membrane structures and charge property together with the application in the separation of cephalexin were performed. The application in the removal of chromate from aqueous solution under different pH is also discussed in detail.

A detailed discussion of the experimental results and conclusions are presented at the end of each respective chapter. General conclusions drawn from whole research are summarized in the Chapter Six. Included in this ending chapter are some recommendations for future research related to this study. Appendix A provides the calculation of velocity distribution, shear rate at the outlet of spinneret.

CHAPTER TWO

EFFECTS OF FLOW ANGLE WITHIN SPINNERET, SHEAR RATE AND ELONGATION RATE ON MORPHOLOGY AND SEPARATION PERFORMANCE OF ULTRAFILTRATION HOLLOW FIBER MEMBRANES

2.1. Introduction

The hollow fiber spinning process is much more complex since hollow fiber is fabricated by a phase inversion process when a polymer solution and a bore fluid solution are simultaneously extruded from a spinneret to a coagulant. Although the residence time of a polymer solution flowing through the annular channel (a few mm in length) is very short, the flow induced shear stress can affect the rheological behavior of the polymeric solution because most highly concentrated polymeric solutions are viscoelastic fluid, i.e. non-Newtonian fluid. For straight annular spinnerets, the effect of molecular orientation induced by shear stress on membrane performance had been investigated by several researchers [Chung et al. 2000; Aptel et al., 1985; Silton et al., 1997; Qin et al., 2001]. Their results suggested that the hollow fiber membranes spun with an enhanced shear rate had a lower permeability but a higher separation due to a greater molecular orientation frozen in the high-sheared fibers. It was also found that there was a certain critical value

of shear rate. When the dope extrusion speed (shear rate) was over this value, the performance of the hollow fiber finally obtained may either drop [Chung et al., 2000] or would not be influenced significantly [Qin & Chung, 1999].

The induced orientation by shear stress or elongation stress affects not only separation performance, but also thermal and mechanical properties of hollow fibers. Yang and Chou [1996] found that the breaking stress and breaking elongation of polyacrylonitrile hollow fibers increased with draw ratio when the hollow fiber samples were in dry state. Moreover, with the aid of AFM [Chung et al., 2002], it was found that the nodules resulted from spinodal phase separation in the outer skin appeared to be randomly arranged at low shear rates but formed bands that were aligned in the direction of dope extrusion when shear rate increased. The results from AFM images also demonstrated the hypothesis that the higher shear stress in the spinneret may result in UF hollow fiber membranes with a denser skin due to the greater molecular orientation and the compact packing of molecules. Infrared reflection spectroscopic techniques have also been used to directly measure mechanically induced orientation of polymer molecules in hollow fibers [Xue et al., 1986; Ismail et al., 1997; Idris et al., 2003]. The spectroscopy analysis has provided the evidence for the increased molecular orientation that occurred in hollow fiber membranes spun under high extrusion shear. Recent results published by Gordeyev et al. [2001] provided the evidence by using Raman spectroscopy to suggest that spinning hollow fibers at high shear rates can induce anisotropy on the molecular level. For straight annular spinnerets, the highest shear stress usually occurs at the wall of the spinneret since the dope solution is normally a non-Newtonian fluid.

Chung and co-workers [Chung et al., 2000; Qin et al., 1999, 2000, 2001] had purposely chosen the wet-spinning process and used water as the external coagulant. It was believed that the effects of gravity and elongation stress on fiber formation could be dramatically reduced and the molecular orientation induced by shear stress within the spinneret could be frozen into the wet-spun fibers. Moreover, the ratio of dope flow rate over bore fluid flow rate was kept constant to reduce the complicated coupling effects (dragging, uneven demixing) of bore fluid flow rate on fiber formation. However, to our best understanding, no reports have been published on the effects of conical spinnerets on hollow fiber ultra-filtration membranes. All of above studies were based on the hollow fiber spinning with the straight annular spinnerets. One objective of this work is to extend the previous spinning technology to conical spinnerets and to understand the effect of flow angle within the spinneret on the molecular chain packing and separation performance for UF membranes.

If there is an air gap before coagulation, the effects of elongation and relaxation will play important roles. The elongation stresses (mostly outside the spinneret) from gravity and spin line stresses complicate the kinetics and dynamics of the phase inversion process [Chung, 1997]. In addition, non-Newtonian polymer solutions may exhibit die swell and relaxation after exiting from spinneret due to the relaxation of polymeric macromolecules. Therefore, investigating effects of elongation stresses on the morphology and structure of the fabricated hollow fiber membrane is another objective in this study.

2.2. Characterization of the mean pore size and the pore size distribution of UF hollow fiber membranes from solute separation data

Ultrafiltration membranes can be characterized by the pore size and the pore size distribution obtained from solute transport experiments. According to the method, the size of the solutes used for the ultrafiltration experiments should be known. Generally, the Stokes radius is used to describe the dimension of solutes. The Stokes radius of a macromolecule can be calculated by the Einstein equation [Einstein, 1956]:

$$D_{AB} = \frac{kT}{6r\pi\eta} \tag{2.1}$$

where D_{AB} is the diffusivity of the macromolecule in a solution (m^2/s), k is the Boltzmann constant, η is the solvent viscosity (Pa s), and r is the Stokes radius of the solute (m). The diffusivity can also be related to the intrinsic viscosity [Hsieh, et al., 1979]:

$$D_{AB} = \frac{2.5 \times 10^6 \, kT}{\eta (M[\eta])^{1/3}} \tag{2.2}$$

where M is the molecular weight (kg/mol), and $[\eta]$ is the intrinsic viscosity of the polymer (m^3/kg). By combining above two equations, the following equation can be obtained for r, the Stokes radius of solute (m), in the aqueous solution [Singh et al., 1998]:

$$r = 2.122 \times 10^{-10} (M[\eta])^{1/3} \tag{2.3}$$

Because the solvent viscosity η and the intrinsic viscosity $[\eta]$ depend on the solvent, the intrinsic viscosity of polyethylene glycol (PEG) and polyvinylpyrrolidone (PVP) of various molecular weights can be calculated from the empirical Mark-Houwink equations as follows:

For PEG [Meireles et al., 1995]: $\qquad [\eta] = 4.9 \times 10^{-4} \times M^{0.672}$ $\qquad\qquad$ (2.4)

For PVP [López de sa et al., 1987]: $\qquad [\eta] = 6.2 \times 10^{-5} \times M^{0.78}$ $\qquad\qquad$ (2.5)

By substituting the expression of the intrinsic viscosity $[\eta]$ into Eq. 2.3, we can obtain:

For PEG: $\qquad\qquad\qquad\qquad r = 16.73 \times 10^{-12} \times M^{0.557}$ $\qquad\qquad$ (2.6)

For PVP: $\qquad\qquad\qquad\qquad r = \;\;8.40 \times 10^{-12} \times M^{0.593}$ $\qquad\qquad$ (2.7)

Michaels [1980] found that solute rejection can be expressed by the log normal probability function of the solute size, for both biological and synthetic membranes, as expressed in the following equation:

$$R = erf(y) = \frac{1}{\sqrt{2\pi}} \int_{-\infty}^{y} e^{-\frac{u^2}{2}} \, \mathrm{d}u, \quad where \quad y = \frac{\ln d_s - \ln \mu_s}{\ln \sigma_g} \qquad (2.8)$$

and R is the separation factor (%), d_s is the solute diameter, μ_s is the geometric mean diameter of solute at $R = 50\%$, σ_g is the geometric standard deviation about μ_s, defined as the ratio of d_s at $R = 84.13\%$ and $R = 50\%$. When the solute separation factor (%) of an ultrafiltration membrane is plotted vs. the solute diameter on a log-normal probability paper, a straight line is yielded as:

$$F(R) = A + B\,(\ln d_s) \qquad\qquad (2.9)$$

By ignoring the steric and hydrodynamic hindrance effects of the pore on solutes [Cooper & Van Derveer, 1979], and neglecting the deformation of macromolecules under pressure and shear rate in the solution [Nguyen & Neel, 1983], the mean effective pore size μ_p and the geometric standard deviation σ_p can be considered the same as the μ_s and σ_g, which

determine the position and sharpness of the rejection curve, respectively. Therefore, based on μ_p and σ_p, the pore size distribution of a UF membrane can be expressed as the following probability density function [Youm & Kim, 1991] by the derivative of the Eq. (2.8) with respect to R:

$$\frac{\mathrm{d}\,R(d_p)}{\mathrm{d}\,d_p} = \frac{1}{d_p \ln \sigma_p \sqrt{2\pi}} \exp\left[-\frac{(\ln d_p - \ln \mu_p)^2}{2(\ln \sigma_p)^2} \right] \qquad (2.10)$$

Aimar et al. [1990] measured the rejection coefficients of membranes with dextrans and the data were fitted to a log-normal pore size distribution. Another attempt was to use aqueous PEG solutions with different molecular weights as the feed solutions in UF experiments to evaluate the mean pore size, the pore size distribution and the porosity from the solute separation data [Singh et al., 1998]. The effects of fouling and concentration polarization during the separation process can be neglected by employing high circulation rates and dilute solutions.

2.3.   Experimental

2.3.1.   Chemicals

Polyethersulphone (PES) RADEL A-300 (average M_w: 15,000 Da, a mixture of primarily polyethersulphone with a low level of polyetherethersulphone, as shown in Figure 2.1) was purchased from Amoco Performance Products, OH, USA. Polyethersulfone possesses the highest concentration of sulphone moieties in the polymer repeat unit. This polar moiety attracts water, with the result that polyethersulphone has the highest water absorption of the commercial sulphone polymers. The glass transition temperature (Tg) of PES is 220 ºC.

Polyethersulphone

Polyetherethersulphone
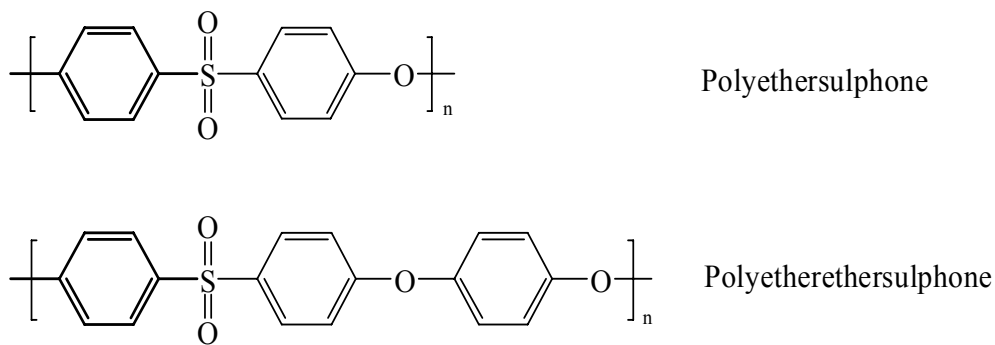
Fig. 2.1 Chemical structure of polyethersulphone and polyetherethersulphone

The solvent, *N*-methyl-2-pyrrolidone (NMP, > 99%), and non-solvent, diethylene glycol (DG) were provided by Merck. Polyethylene glycol (PEG, average M_w: 2,000) and three kinds of poly(vinyl pyrrolidone) (PVP) from Acros Organics, NJ, USA, PVP 10K (average M_w: 10,000 Da),   PVP 24K (average M_w: 24,000 Da) and PVP 40K (average

M_w: 40,000 Da), were used as solutes to measure the separation performance of as-spun ultrafiltration hollow fiber membranes. Other organic solvents were of reagent grade and used as received. The ultrapure water used in all experiments was produced by a Milli-Q unit (MilliPore, USA) with the resistivity of 18 MΩ cm.

2.3.2. Fabrication of UF hollow fiber membranes

The PES powder was dried at about 120°C in a vacuum oven for 12 hr to remove moisture content. The viscosity corresponding to different concentration of PES/NMP system (26 ºC) was plotted in Figure 2.2. The spinning dope solution of PES/NMP/DG (23/41/36 wt %) is prepared in advance. The dried PES powder was dispersed slowly into a chilled NMP and DG mixture (0~3°C, contained in a flask that was immersed in an ice bath), and stirred continuously with a high speed mechanical stirrer at room temperature. Finally, the flask with the mixture was stirred for two days until the solution became homogeneous. It was designed that this dope formulation was close to its cloud point (the binodal line) in order to speed up the phase separation during spinning, thus yielding a membrane with a thin skin and high water flux. The addition of DG as a non-solvent can result in a more rapid phase separation. The homogeneous dope solution prepared for spinning was used to study the dope rheological characteristics within the spinneret. An ARES Rheometric Scientific Rheometer was used to determine the shear stress of the dope solution as a function of shear rate. The viscosity of a polymeric solution is determined from the measured torque necessary to overcome the viscous resistance when a cone rotates in a fluid. The experiment was carried out using a 25 mm cone plate at 25°C and the steady-state shear rate was measured in the range of 1-100 s^{-1}.
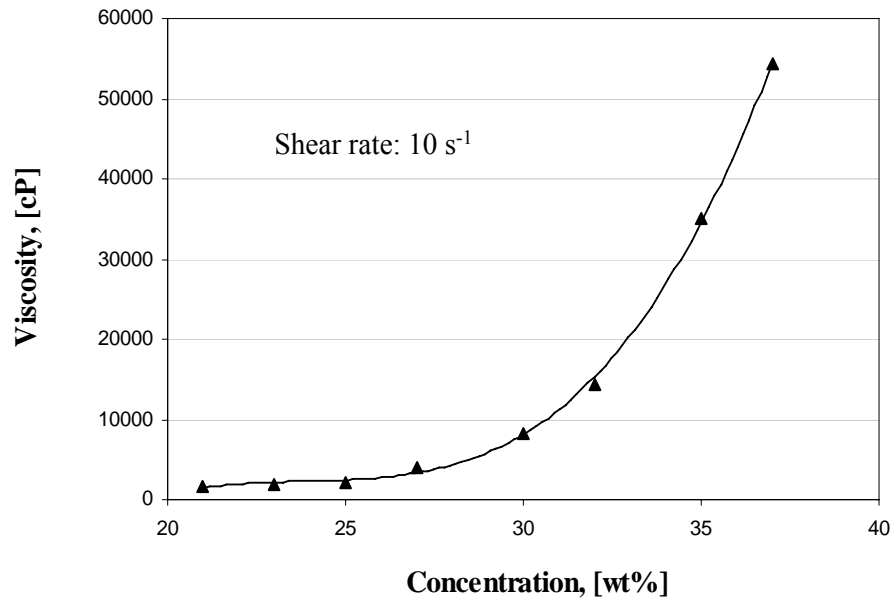
Fig. 2.2. Viscosity versus concentration of PES/NMP system

The power-law model [Shilton, 1997] was applied to fit the rheological data and a relationship between shear stress τ (N m^{-2}) and shear rate $\dot{\gamma}$ (s^{-1}) of the spinning dope solution was obtained as follows:

$$\tau = 13.28 \times |\dot{\gamma}|^{0.7968} \qquad (2.11)$$

The shear rate and shear stress induced at the outer wall of a spinneret during hollow fiber formation can be determined by this equation from the velocity profile. Two kinds of spinnerets with different flow angles were used in hollow fiber spinning process, their structures are presented in Figure 2.3.
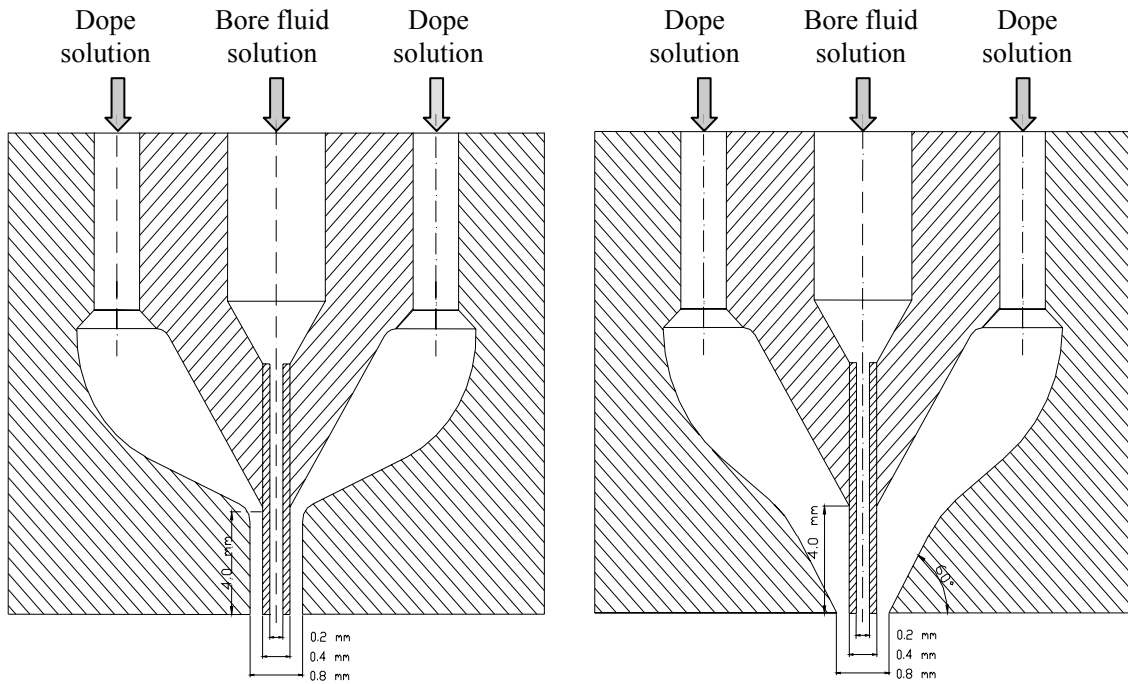
Fig. 2.3. Schematic diagrams of spinnerets with different flow angles (90º and 60º)

The process of hollow fiber spinning is schematically shown in Figure 2.4. The formulated dope and bore fluid solutions were degassed before spinning, and filtered by a metal filter (15μm) to remove the particles in the solution during spinning. The pulse-free bore fluid and dope solution were fed into the inner tube and the annulus of the spinneret separately through flow meters by two ISCO syringe pumps. Table 2.1 lists the detailed spinning parameters. The ratio of dope flow rate over bore fluid rate was especially kept constant to reduce the complicated coupling effects (dragging, uneven demixing) of bore fluid flow rate on fiber formation during wet-spinning process. All nascent fibers did not experience additional extra drawing (i.e., no extension) after leaving the spinneret, which

means that the take-up speed of the hollow fibers was almost the same as the falling

speed into the coagulation bath.
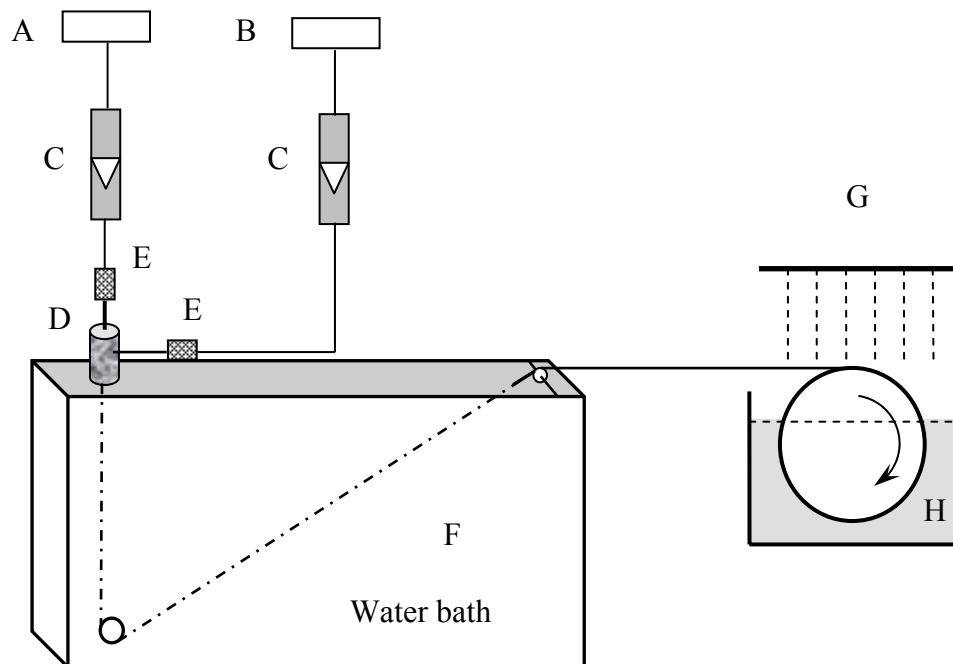
A: Bore fluid tank   B: Dope solution tank   C: Syringe pump   D: Spinneret
E: Filter   F: Coagulation bath   G: Water sprinkling   H: Fiber collecting bath

Fig. 2.4 Schematic diagram of the hollow fiber spinning line

The as-spun fibers were immersed in water for 3~5 days to remove the residual NMP and

DG. Then, the fibers were post-treated by the following two methods. Hollow fibers that

were dipped in a 50 wt% glycerol aqueous solution for 48 hr and dried in air at room

temperature were used for separation experiments. Other post-treatment was carried out

by the methanol-hexane solvent exchange method to prepare samples for the study of

morphology, thermal and mechanical properties. Hollow fibers were immersed in fresh

methanol and hexane for 0.5 hr three times separately under stirring, and then dried in air

at ambient temperature in order to gradually reduce the effect of surface tension during

fiber drying and minimize fiber deformation and pore collapse.

Table 2.1 Experimental parameters of spinning UF hollow fiber membranes

Dope solution composition (wt %)	PES/NMP/DG (23:41:36)
Dope solution viscosity (cP) at 10 s^{-1}	7873
Dope flow rate (ml/min)	0.25, 0.50, 1.00, 2.00, 3.00, 4.00, 5.00, 7.00, 10.00
Bore fluid composition (wt %)	NMP/H$_2$O (86:14)
Ratio of bore fluid to dope flow rate	0.5
Air gap distance (mm)	0 (wet spinning)
External coagulant	tap water
Coagulant temperature (ºC)	26 ± 1
Dimensions of spinneret (mm)	ID/OD (0.4/0.8)
Die length in spinneret, L (mm)	4.0
Spinneret temperature (ºC)	26 ± 1
Room relative humidity (%)	65~70

2.3.3. Morphology study of hollow fibers by scanning electron microscope (SEM)

The dried hollow fiber samples treated by the methanol-hexane procedure were immersed

in liquid nitrogen and fractured, and then sputtered with gold using a Jeol JFC-1100E Ion

Sputtering device. The cross-section, inner layer and outer layer of samples were

observed under Scanning Electronic Microscopy (SEM, JEOL JSM-5600LV) and Field

Emission Scanning Electronic Microscopy (FESEM JEOL JSM-6700).

2.3.4. Ultrafiltration experiments with hollow fiber membranes

The schematic diagram of the testing instrument to measure water flux and solute separation performance is illustrated in Figure 2.5. Three testing modules with filtration area about 30 cm^2 were made for each hollow fiber sample. Since the outer surface of hollow fiber is the selective layer, the feed was pumped into the shell side and the permeate was collected from the lumen side of the fiber.
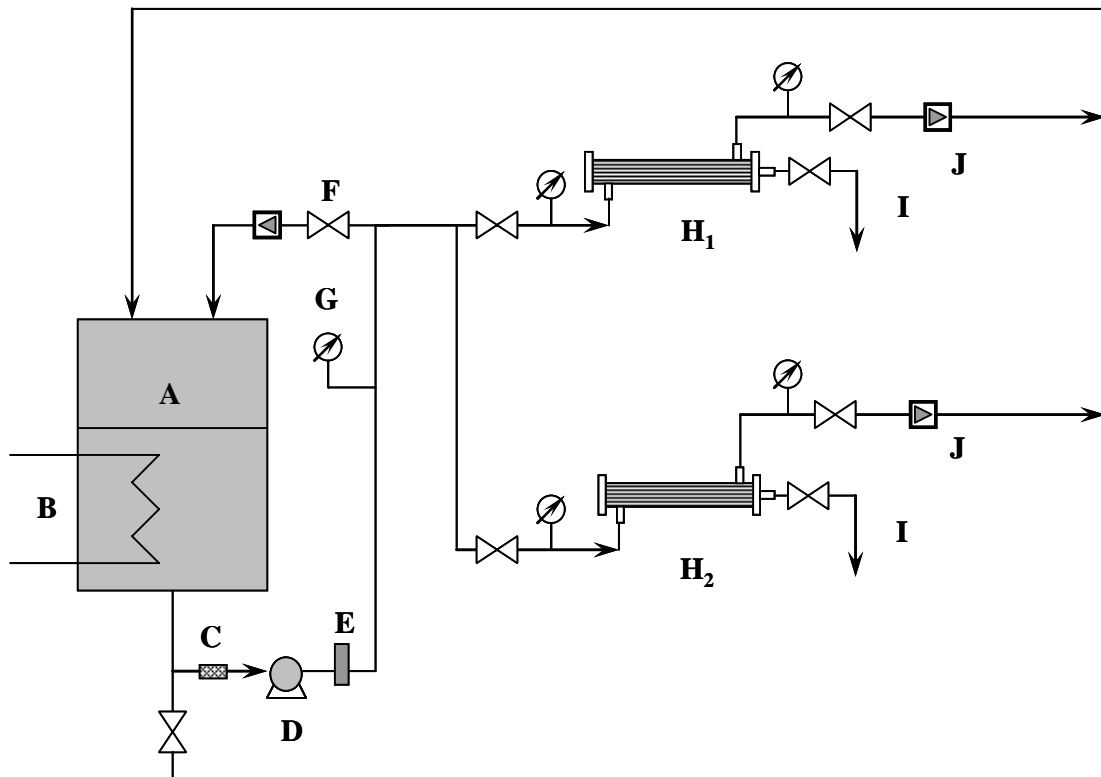
A = Feed tank, B = Cooling coil, C = Filter, D = High pressure pump, E = Pulsation damper,
F = Bypass valve, G = Pressure gauge,   H = Permeation cell,   I = Sampling valve, J = Rotameter

Fig. 2.5. Schematic diagram of the measuring instrument for water flux and separation
performance of UF hollow fiber membranes.

According to the common method proposed by Sourirajan and Matsuura [1985], the hollow fiber membranes will be characterized in terms of pure water permeability and solute separation with different dimensional solutes dissolved in the ultrapure water. The feed concentration was kept around 200 ppm, the trans-membrane pressure about 5.0 bar (gauge) and the feed solution was circulated maintaining turbulent flow conditions which could minimize the effect of concentration polarization (Reynolds number, *Re* > 2500). Each fiber sample was firstly subjected to pure water permeation experiment to get rid of glycerol and measure pure water permeation flux. The normalized pure water permeability (*PWP*, liter m^{-2} bar^{-1} hr^{-1}) was calculated by the following equation:

$$PWP = \frac{Q}{A \cdot \Delta P}$$
(2.12)

where *Q* is the water permeation volumetric flow rate (liter hr^{-1}), *A* is the effective filtration area (m^2), *ΔP* is the trans-membrane pressure (bar).

After the pure water permeation experiment, the feed was switched from pure water to a PEG feed solution. The PEG solution was circulated for about 1.0 h until the whole system reached the steady state. The permeate was then collected for a predetermined period and the volume was measured, before being subjected to analysis. The ultrafiltration experiments were carried out with solutes of progressively higher molecular weights. The module was thoroughly flushed with distilled water between runs of different MW solutes. The concentration of feed and permeate were determined by a total organic carbon analyzer (SHIMADZU ASI-5000A). The solute separation was calculated by using the following equation:

$$R = \left(1 - \frac{C_p}{C_f}\right) \times 100 \qquad\qquad (2.13)$$

where C_p and C_f are the solute concentration in the permeate and in the feed solution, respectively. During the water permeate and solute separation tests the temperature of feed was maintained at 25°C. The solute separation data were further used for estimating the mean pore size and the pore size distribution of the selective layer.

2.4. Results

2.4.1. Effects of flow angle within spinneret and the shear rate on the structure of the as-spun hollow fiber membranes

Tables 2.2 and 2.3 summarize the calculated dope extrusion speed of nascent hollow fibers at the outlet of the spinneret, take-up speed and the dimension of as-spun hollow fibers. The outer diameter and wall thickness of hollow fibers increase significantly with an increase of dope flow rates although water can accelerate coagulation during spinning. This may be due to the effect of die swell when a pressurized polymer solution is extruded from the spinneret although water is used as a strong coagulant. Figures 2.6 ~ 2.9 show the SEM images of the cross-section, inner edge, outer edge, inner surface and outer surface of hollow fibers, respectively, which were spun from different dope extrusion speeds but with a constant ratio of dope flow rate to bore fluid flow rate.

For the 90° straight spinneret, the SEM pictures (Figures 2.6 and 2.7) indicate that hollow fibers were full of long finger-like macrovoids across the cross-section and some small macrovoids scattered around the inner skin when the dope flow rate was 0.25ml min^{-1}. This is probably due to the rapid liquid-liquid demixing process with high precipitation rates. However, a clear double-layer structure of macrovoids could be observed when the dope flow rate was increased to 1.0 ml min^{-1} and the size of the previously observed long finger-like macrovoids was significantly reduced. Interestingly, most macrovoids disappeared when the dope flow rate was further increased to 3.0 ml min^{-1} or over. For the 60° conical spinneret, the same phenomenon could be observed at low dope flow

Table 2.2 Outer diameter, inner diameter and wall thickness of UF hollow fibers (from the 90º spinneret)

Fiber ID	Dope flow rate (ml min^{-1})	Dope extrusion speed v_1 (m min^{-1})	Take-up speed v_2 (m min^{-1})	Ratio of v_2 / v_1	OD (μm)	ID (μm)	Wall thickness (μm)
UF 90A	0.25	0.66	0.71	1.76	650	400	125
UF 90B	1.00	2.65	2.10	0.79	760	440	160
UF 90C	3.00	7.96	4.60	0.78	880	520	180
UF 90D	7.00	18.57	8.24	0.44	1,020	600	210
UF 90E	10.00	26.53	11.14	0.42	1,040	630	215

Table 2.3 Outer diameter, inner diameter and wall thickness of UF hollow fibers (from the 60º spinneret)

Fiber ID	Dope flow rate (ml min^{-1})	Dope extrusion speed v_1 (m min^{-1})	Take-up speed v_2 (m min^{-1})	Ratio of v_2 / v_1	OD (μm)	ID (μm)	Wall thickness (μm)
UF 60A	0.25	0.66	0.80	1.21	640	380	130
UF 60B	1.00	2.65	2.14	0.81	740	440	150
UF 60C	3.00	7.96	4.74	0.60	880	530	175
UF 60D	7.00	18.57	8.09	0.44	1,060	620	210
UF 60E	10.00	26.53	10.81	0.41	1,080	630	225

rates. However, the situation changed at high shear rates. It appears that, at high flow

rates, although the first-layer long finger-like macrovoids were suppressed, the 2nd-layer

macrovoids around the inner layer grew with increasing flow rate. This is probably due to

the complicated flowing pattern within the 60° conical spinneret.
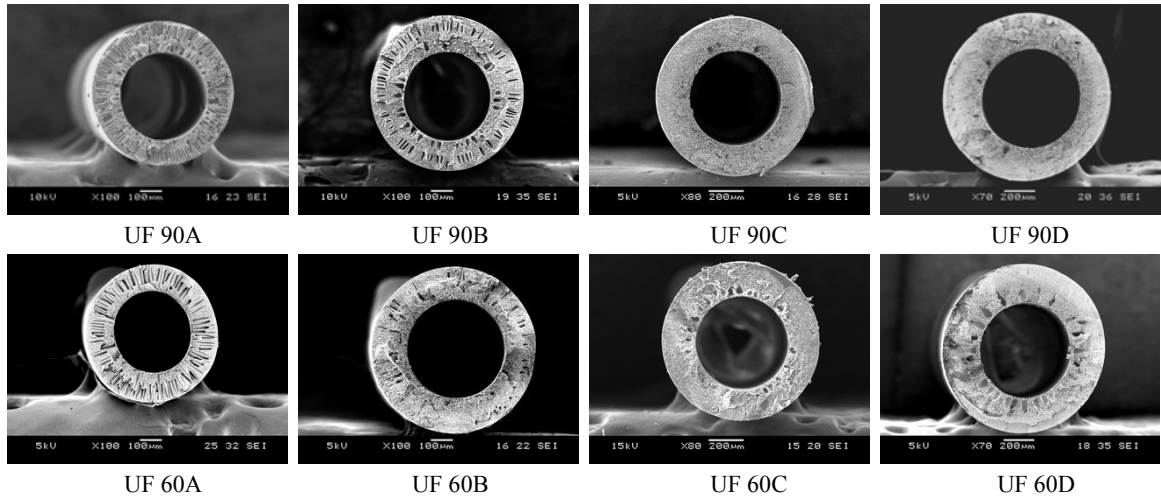
Fig. 2.6. The overall cross-section of UF hollow fibers spun at different dope flow rates.
(Left-hand side four images: the scale bar 100μm; right-hand side four images: the scale bar 200μm)
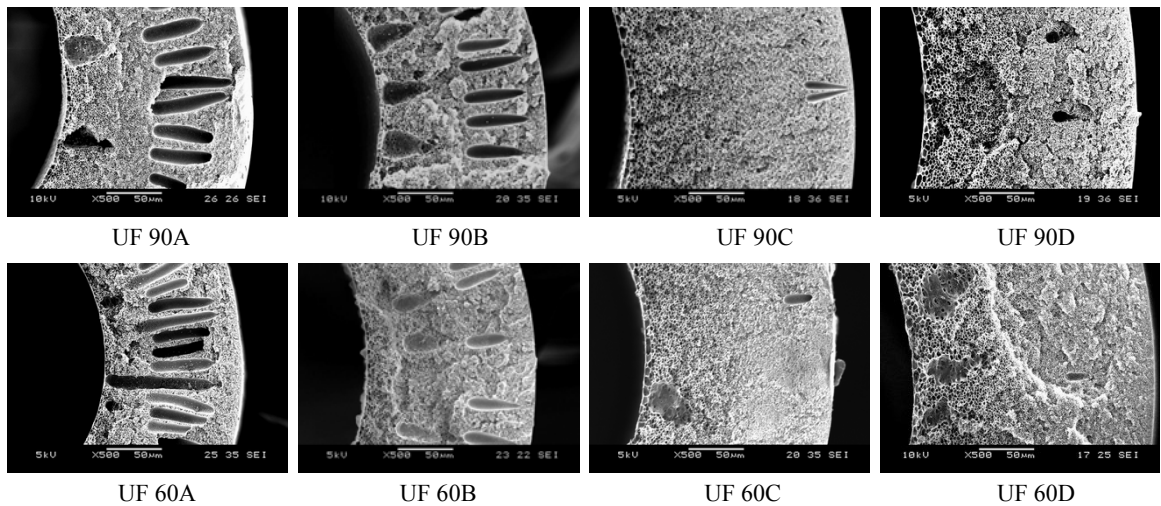
Fig. 2.7. The partial cross-section of UF hollow fibers spun at different dope flow rates.
(The scale bar 50μm)

Figure 2.8 indicates that the inner surface of hollow fibers was fully porous. This is due to the delayed liquid-liquid demixing process taking place at the fiber inner surface because of high solvent concentration in the bore fluid, i.e. the polymer concentration was lower at this particular region, leading to the nucleation and growth of the localized polymer-rich phase that produced low integrity polymer agglomerates.

| UF 90A | UF 90B | UF 90C | UF 90D |
| UF 60A | UF 60B | UF 60C | UF 60D |
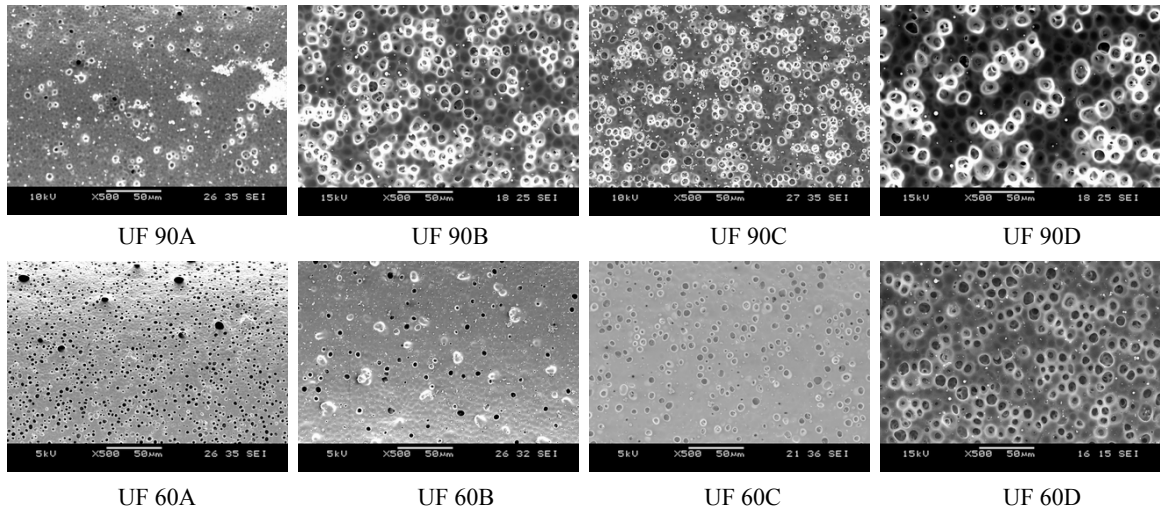
Fig. 2.8. The inner surface of UF hollow fibers at different dope flow rates (the scale bar 50 μm)

| UF 90A | UF 90B | UF 90C | UF 90D |
| UF 60A | UF 60B | UF 60C | UF 60D |
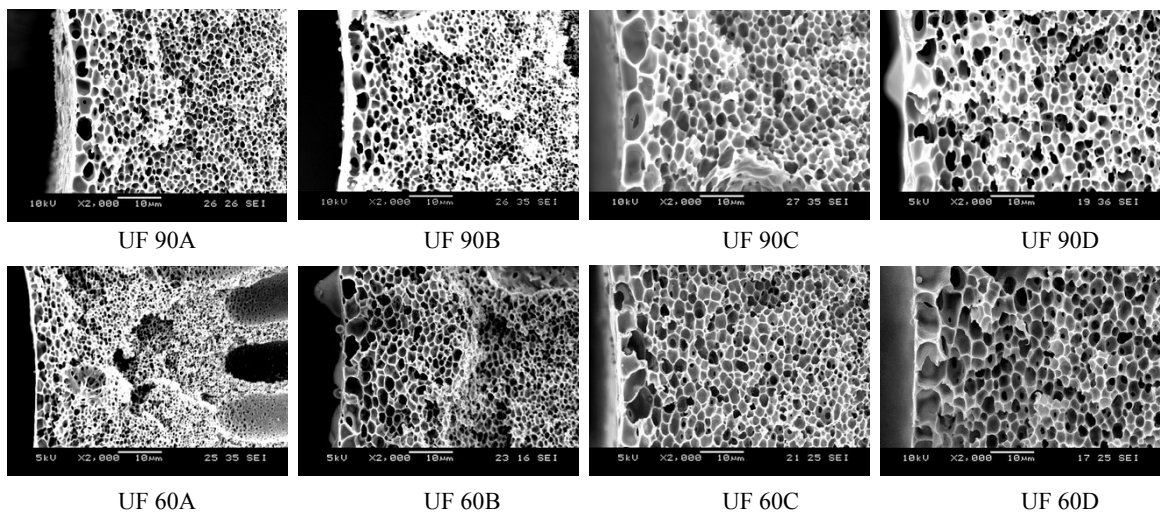
Fig. 2.9. The inner edge of UF hollow fibers spun at different dope flow rates (the scale bar 10μm)

56

Upon the completion of the slow precipitation, the resulting morphology near inner layer was an interconnected open-cell structure which can be seen from Figure 2.9. The middle part of the hollow fiber is very porous from Figure 2.10. As a result, the transport resistance brought by the inner layer and middle layer could be reduced to the minimum.

| UF 90A | UF 90B | UF 90C | UF 90D |

| UF 60A | UF 60B | UF 60C | UF 60D |
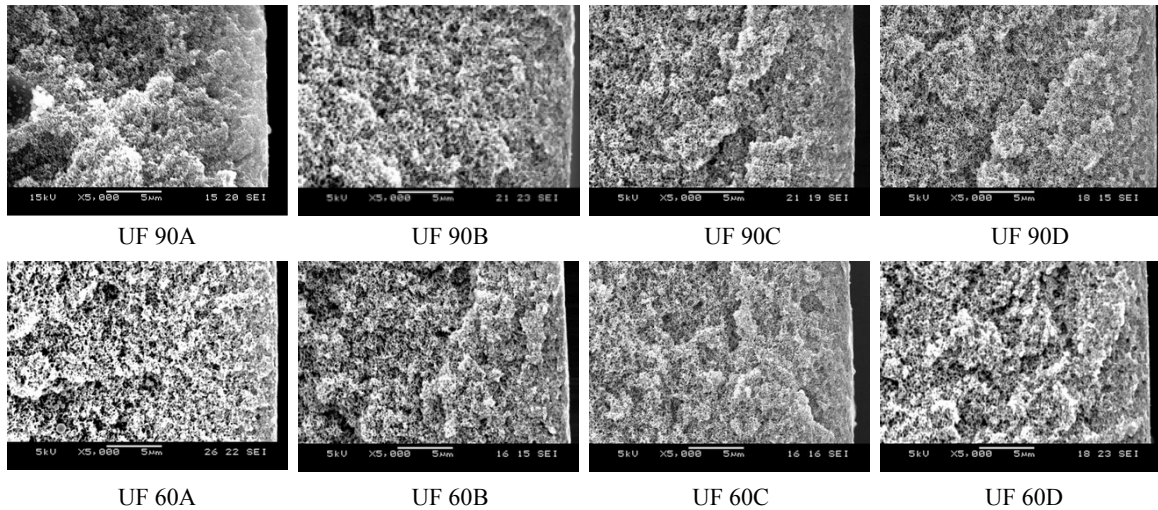
Fig. 2.10. The outer edge of UF hollow fibers spun at different dope flow rates (the scale bar 5μm)

| UF 90A | UF 90B | UF 90C | UF 90D |

| UF 60A | UF 60B | UF 60C | UF 60D |
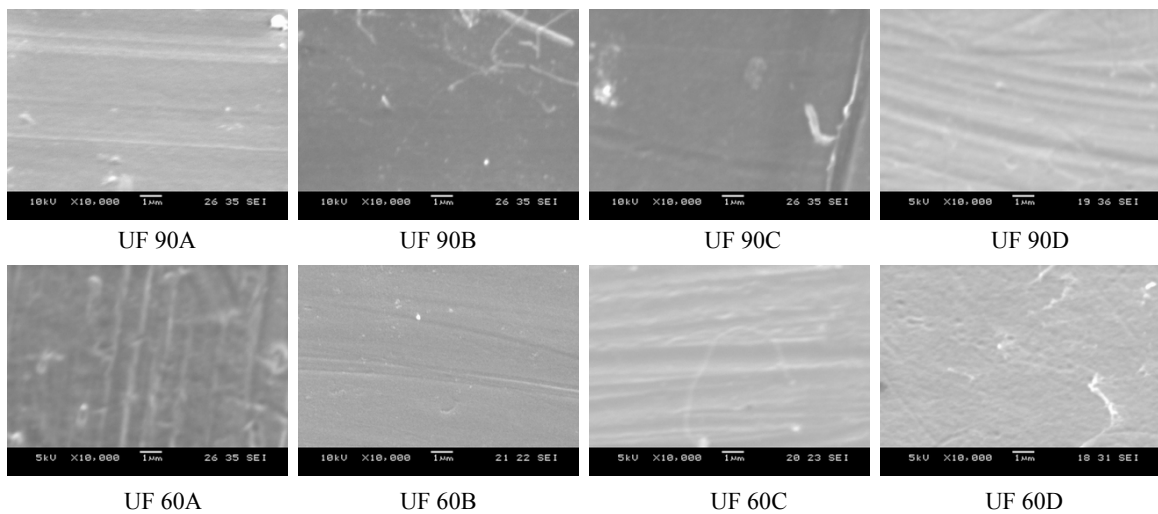
Fig. 2.11. The outer surface of UF hollow fibers at different dope flow rates (the scale bar 1μm)

From Figure 2.11, it can be observed that the outer surface is a dense layer regardless of low or high shear because an outer skin was formed on the top of an open-celled substructure due to instantaneous liquid-liquid demixing process by using water as the coagulant.

2.4.2 Effects of flow angle within spinneret and the shear rate on the separation performance of the as-spun UF hollow fiber membranes

Figure 2.12 shows that the *PWP* dropped sharply with an increase in the dope flow rate and then leveled off at 13.7 and 16.5 liter m^{-2} bar^{-1} hr^{-1} for 90º and 60º spinneret, respectively. Moreover, hollow fibers spun from the 90º spinneret had larger *PWP* values than hollow fibers spun from the 60º spinneret at same dope flow rate (for example, the largest difference of PWP was up to 10.0 liter m^{-2} bar^{-1} hr^{-1} between the 90º spinneret and 60º spinneret at the dope flow rate of 1.0 ml min^{-1}). The effect of increased in the dope solution velocity in producing tighter skin of fibers is explained by the shear forces in the annular orifice of spinneret. It is known that polymer molecules under shear flow tend to align themselves in the direction of flow. The results also confirm the effects of tighter molecular packing and molecular chain orientation induced by the 60º flowing channel which squeezes the polymer solution out. From the Hagen-Poisseuille equation:

$$J = \frac{\varepsilon \cdot r^2}{8\eta\tau} \frac{\Delta p}{l} \qquad (2.14)$$

This implies that the porosity (ε) of the outer layer decreases with an increase in the dope flow rates, if assuming the same pore radius (in fact the pore sizes will be different) and

pore length for all hollow fibers and neglecting the transport resistance of the support

layer.
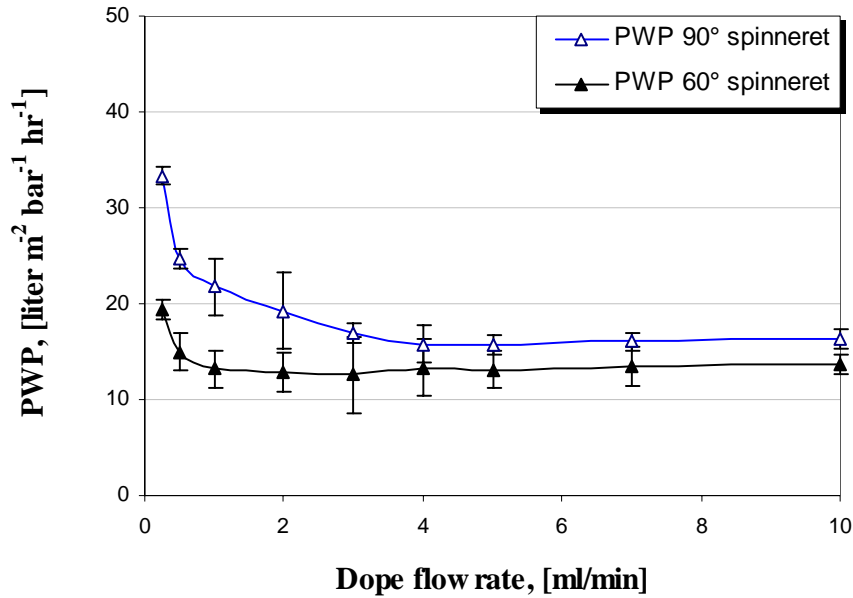
Fig. 2.12. Effects of dope flow rates and flow angles on PWP of UF hollow fibers.

From Figure 2.13, the solute rejection for a particular solute increased sharply with an

increase of dope flow rate (for example, the solute separation coefficient of PVP 10,000

increased from 18% at the dope flow rate of 0.25 ml min^{-1} to 44.5% at the dope flow rate

of 0.5 ml min^{-1} for 90º spinneret; while same trend can be observed for 60º spinneret),

which indicates that the outer skin of the hollow fiber membrane has become more

selective. After reaching a maximum, the solute rejection decreased slowly with an

increase of dope flow rate, possibly due to the shear-thinning effect which may result in

the formation of looser outer skin at high shear stresses.
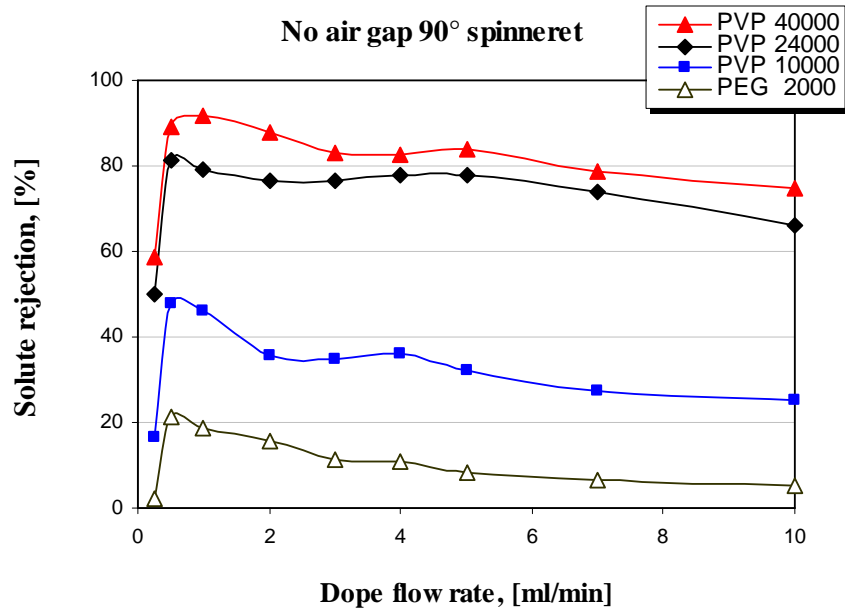
(a)
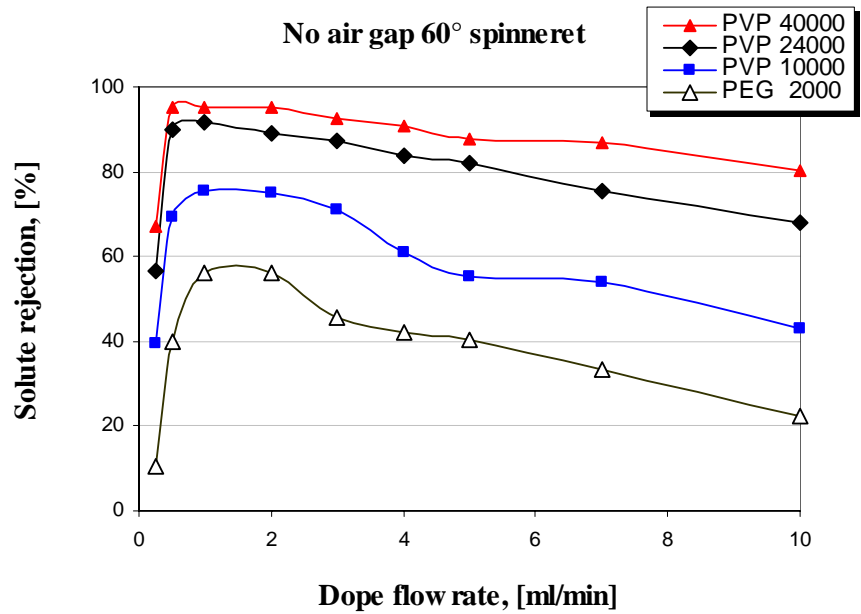
(b)

Fig. 2.13. Effect of dope flow rate on the separation performance of UF hollow fiber membranes spun from a) 90º flow angle spinneret and b) 60º flow angle spinneret

Although the same trend in solute separation performance was observed for the hollow fibers spun from both 60° and 90° spinnerets, hollow fibers spun from the 60º spinneret showed a higher solute separation for a given solute for the same dope flow rate, while hollow fibers spun from the 90º spinneret showed a lower solute separation for a given solute separation (for example, for the rejection of PVP 10, 000, the solute separation coefficient was 75.5 % for 60º spinneret while the solute separation coefficient was 46.5 % for 90º spinneret at the dope flow rate of 1 ml min^{-1}). Clearly, the flow angle within spinneret may play an important role on the water permeate flux and the separation performance of spun hollow fibers.

2.4.3 Mean Pore Size and Pore Size Distribution determined from the Solute Transport Method

Log-normal plots of solute separation versus solute diameter are shown in Figure 2.14 for UF hollow fiber membranes spun from spinnerets with a) 90º and b) 60º flowing angles. Straight lines could be fitted to the data with reasonably high correlation coefficient ($r^2 \geq$ 0.96) for the outer layer of all hollow fibers. The mean of effective pore size μ_p and the geometric standard deviation σ_p were obtained according to the method described in the experimental section and results are given in Table 2.4. The table also includes molecular weight cutoff (MWCO, the molecular weight of a solute at which 90% separation can be achieved for a certain membrane) of the spun hollow fibers. The Stokes diameter of the solute that achieves 90% separation can be obtained from Figure 2.14, and the corresponded M$_w$ (MWCO) can be calculated from Eq. (2.15).

$$r = 8.40 \times 10^{-12} \times M^{0.593} \tag{2.15}$$

(a)

(b)
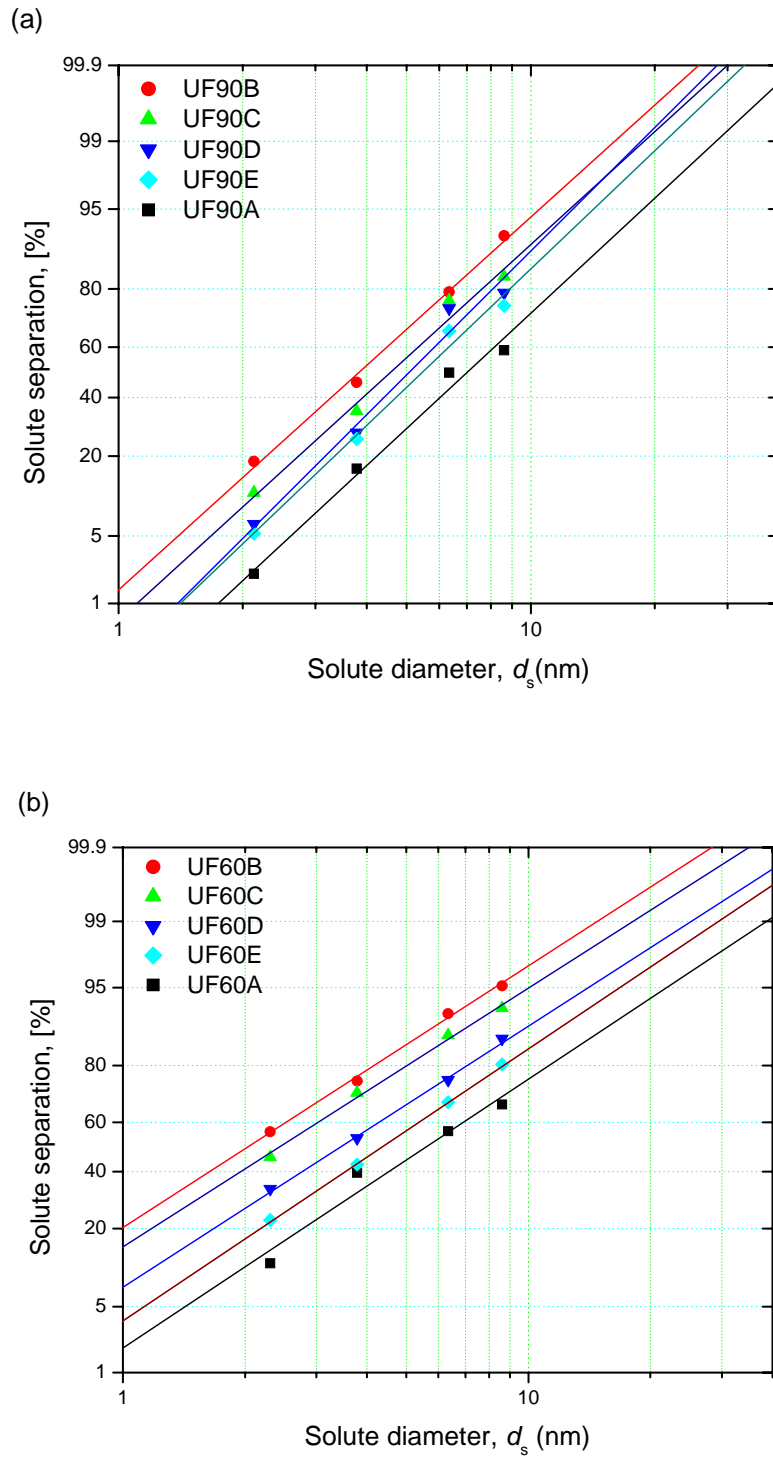
Fig. 2.14. Solute separation curves plotted on a log-normal probability coordinate system of UF hollow fiber membranes spun from spinnerets with a) 90º and b) 60º flow angles under different dope flow rates.

It seems that hollow fibers spun from the 60° spinneret had lower mean pore size and higher geometric standard deviation, compared to those spun from the 90° spinneret, when the comparison was made at the same dope flow rate. In addition, Table 2.4 shows a minimum in the mean of effective pore size in radius (μ_p 4.11 nm for 90° spinneret and μ_p 2.03 nm for 60° spinneret, respectively) which brought about maximum separation performance. This phenomenon was also recorded in other work [Qin et al., 2000]. The most probable reason may be that the dope solution with a polymer high concentration reveals different rheological behavior under low and high shear rate.

Table 2.4. Mean effective pore size (μ_p) in diameter, geometric standard deviation (σ_p) and the molecular weight cut-off (MWCO) of the fabricated UF hollow fiber membranes calculated from the solute transport experiments

Fiber ID	μ_p (nm)	σ_p [-]	MWCO (kDa)	Fiber ID	μ_p (nm)	σ_p [-]	MWCO (kDa)
UF 90A	7.38	1.85	96.8	UF 60A	5.85	2.31	121.1
UF 90B	4.11	1.86	38.7	UF 60B	2.03	2.46	22.3
UF 90C	4.81	1.86	51.3	UF 60C	2.45	2.42	30.7
UF 90D	5.34	1.76	54.7	UF 60D	3.46	2.45	55.0
UF 90E	5.71	1.80	66.1	UF 60E	4.46	2.32	75.0

The cumulative pore size distributions of the hollow fiber membranes are also given as well as the probability density function curves generated from the values of the mean effective pore size μ_p and the geometric standard deviation in Figure 2.15.

Regarding the effect of the flow angle within the spinneret, smaller mean pore sizes of the membranes spun from the 60° spinneret may be attributed to the effect of molecular

chain orientation and packing induced by radial momentum vector [Ismail et al., 1997; Qin et al., 2001], while higher standard deviations (σ_p) are due to the unsteady fluid flow within the spinneret. It is also interesting to note that some of MWCO data for the hollow fibers spun from 60° spinneret were larger than those of 90° spinneret (at dope flow rate of 10 ml min^{-1}, MWCOs were 75.0 and 66.1 kDa for 60° spinneret and 90° spinneret, respectively) although the mean pore sizes of the former hollow fibers were smaller than the latter (μ_p 4.46 nm for 60° spinneret and μ_p 5.71 nm for 90° spinneret, respectively). This may be due to the larger standard deviation of the hollow fibers spun from 60° flow angle spinneret. Thus, flow angle of the spinneret provides another means to control the pore size and the pore size distribution of UF hollow fiber membranes.
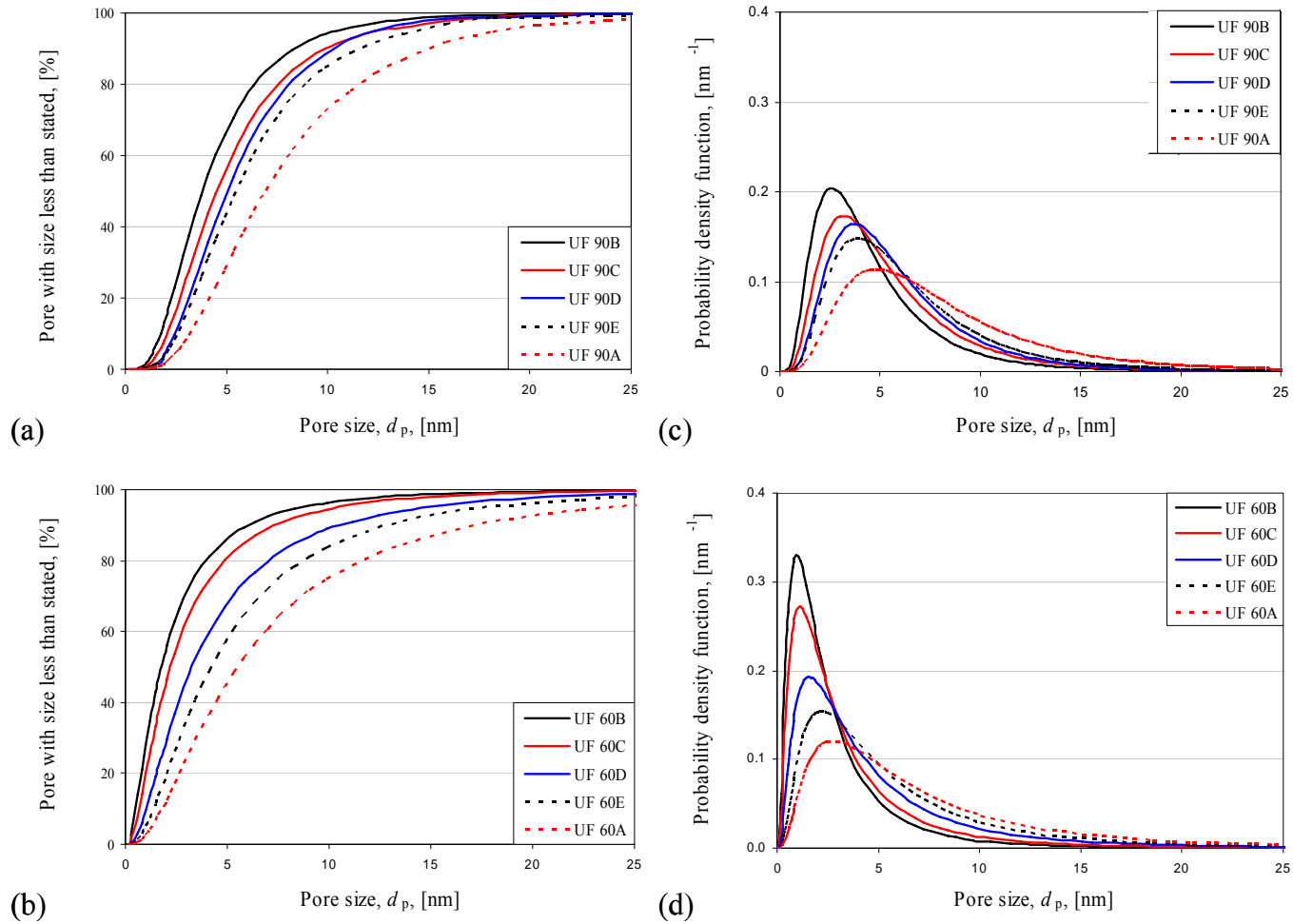
Fig. 2.15. a) & b) Cumulative pore size distribution and c) & d) probability density function curves of UF hollow fiber membranes spun from spinnerets with 90º and 60º flow angles under different dope flow rates.

2.4.4 Shear rate and velocity distribution within spinneret

Table 2.5 gives the shear rate and the shear stress induced in the outer surface of nascent hollow fiber at the outlet of the straight (90º) spinneret as estimated from the power-law fluid model [Bird et al., 1987; Shilton, 1997]. Figure 2.16 illustrates the linear velocity and shear rate distribution of polymer solution at the outlet of the spinneret for different dope flow rates. The detailed calculation process is illustrated in the Appendix A. For the conical (60º) spinneret, on the other hand, both axial velocity and radial velocity exist along with the unsteady fluid flow, which makes the rheological behavior of the non-Newtonian fluid complicated, and the shear stress induced by shear rate cannot be easily calculated from simple analytical solutions. Future work will study the shear stress induced orientation by the axial velocity gradient and the elongation of the molecular chains induced by the radial velocity gradient within the conical spinneret simulated by using the *Fluent* software.

Table 2.5 Dope flow rate, shear rate, shear stress induced in the outer surface of hollow fibers at the outlet of spinneret during spinning (90º spinneret)

Fiber ID	Dope flow rate (ml min^{-1})	Shear rate (s^{-1})	Shear stress (N m^{-2})
UF 90A	0.25	323	1,327
UF 90B	1.00	1,293	4,004
UF 90C	3.00	3,879	9,609
UF 90D	7.00	9,051	18,875
UF 90E	10.00	12,930	25,080

However, although flow angle can suppress the formation of finger-like macrovoids through increasing shear rate within spinneret, finger-like macrovoids inside hollow fibers cannot be completely eliminated during the wet spinning. Another approach may be efficient to make the finger-like macrovoids disappear during dry-jet wet spinning. The following part will study the effect of elongational rate on the microstructure of the resultant hollow fibers.
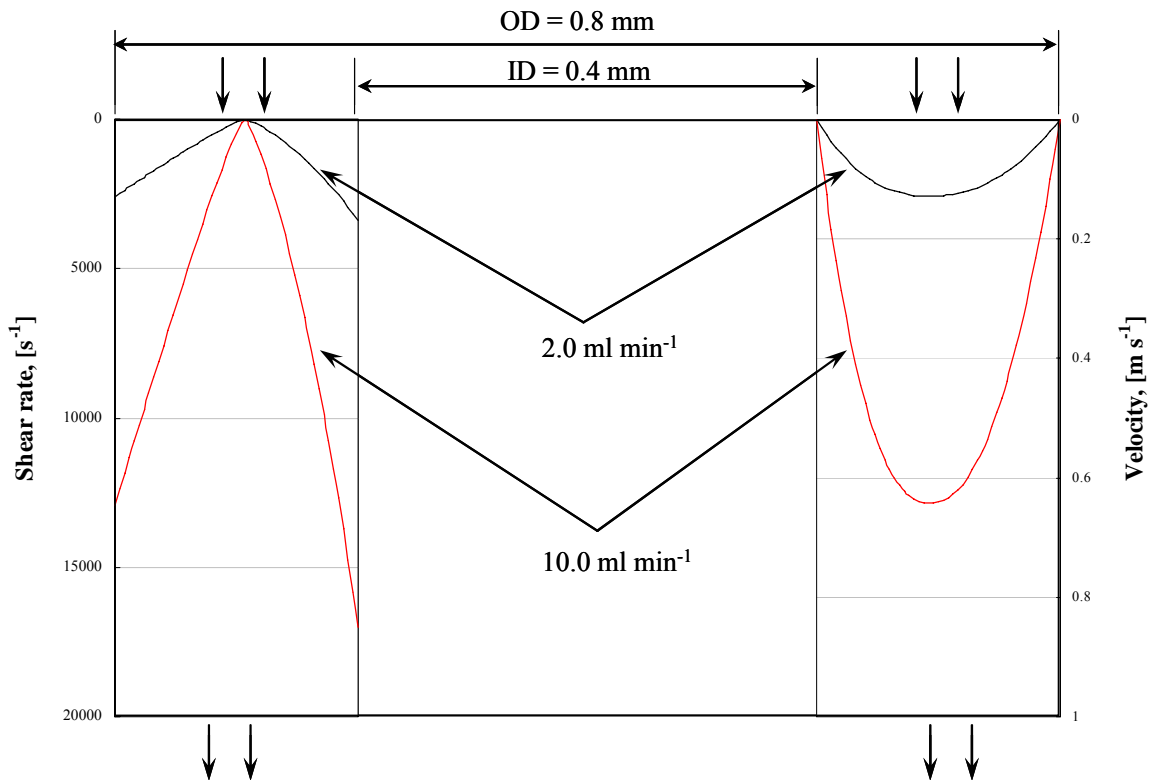
Fig. 2.16 The velocity and shear rate distributions of polymer dope solution at the outlet of the spinneret for different dope flow rates (90° spinneret)

2.4.5. Effect of elongation rate on the morphology of the as-spun UF hollow fibers

In this part, the same polymer dope solution of PES/NMP/DG (23/41/36 wt %) and the 90° straight spinneret were used as the Section 2.3. The dry-jet wet spinning (with air gap of 10 mm) was applied to investigate the effect of elongational rate on the hollow fiber membranes. The elongational draw ratio, φ, can be defined as the ratio of the cross-section area of the spinneret for dope flow to the solid cross-section area of the precipitated hollow fiber membrane as follows,

$$\varphi = \frac{(OD^2 - ID^2)_{spinneret}}{(OD^2 - ID^2)_{hollow\ fiber}} \tag{2-2}$$

Figure 2.17 illustrates the evolution of macrovoids in the cross-section of hollow fiber membranes with the take-up speed and the calculated elongational draw ratio. For free falling (i.e., no elongational drawing), a clear double-layer structure of macrovoids could be observed in the hollow fibers (Figure 2.17a). One layer near the outer skin edge was finger-like; whereas the other layer near the inner skin edge was teardrop-like. When the take-up speed was doubled, the number of finger-like macrovoids decreased. Some finger-like macrovoids were apparently elongated closer to the inner layer. In addition, only a very few teardrop-like macrovoids existed around the inner skin edge. When the take-up speed was tripled, only single layer of finger-like macrovoids could be observed. However, the size and dimension of macrovoids became larger and longer and their total number was clearly reduced (Figure 2.17c). Further increasing the take-up speed, Figures 2.17d) and 2.17e) showed that the finger-like macrovoids decreased sharply and disappeared at 53.5 m/min which was about 6 times of the free falling speed. The SEM

results suggest that macrovoid-free PES hollow fibers can be produced with a sponge-like

structure at an elongational draw ratio of 15.2.
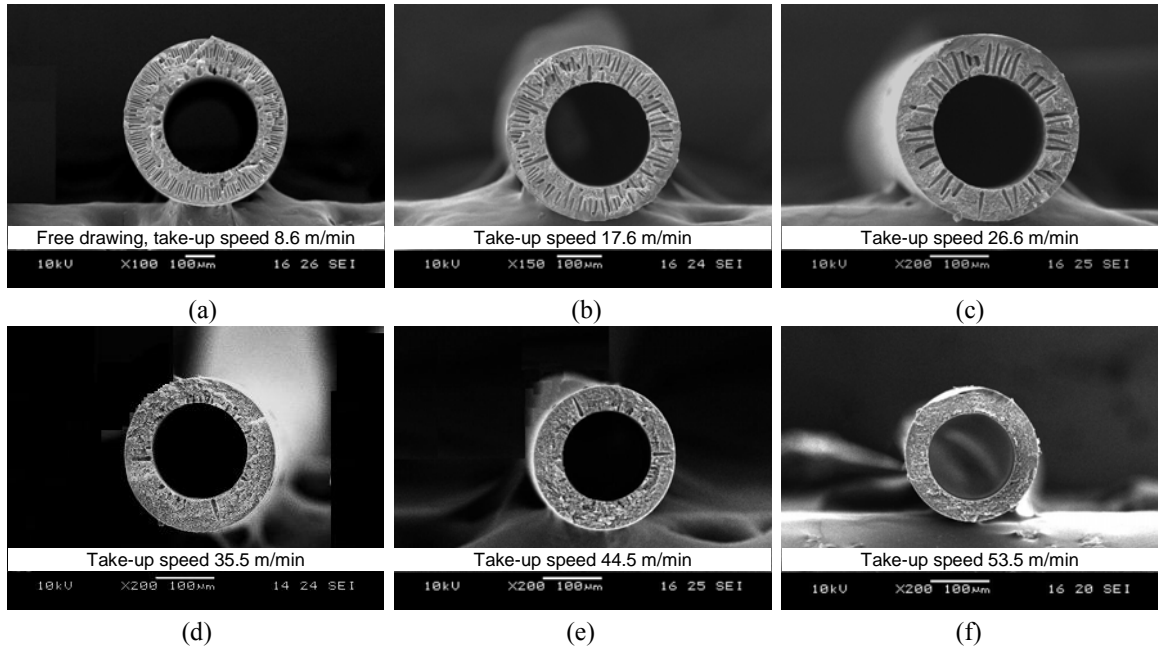
Fig. 2.17   Effects of elongational ratio (dry-jet wet spinning) on the morphology of hollow fiber membranes at different drawing speeds. (Spinneret: OD/ID 0.8/0.4 mm, coagulant: water) Elongational ratio: a) $\varphi = 2.42$, b) $\varphi = 4.55$, c) $\varphi = 7.31$, d) $\varphi = 9.78$, e) $\varphi = 12.00$, f) $\varphi = 15.20$

During wet spinning, from the SEM images of Figure 2.18 a) & b), it is found that pores

in the surface of membranes were elongated in the flow direction as a result of the

alignment of polymer chains under high shear rate, which corresponded to Porter's result

[1990]. If there is an air gap before coagulation, the effects of elongation and relaxation

will play important roles simultaneously. The elongation stresses (mostly outside the

spinneret) from gravity and spin line stresses complicate the kinetics and dynamics of the

phase inversion process. In addition, non-Newtonian polymer solutions may exhibit die

swell and relaxation after exiting from spinneret due to the relaxation of polymeric macromolecules. From SEM images in Figure 2.18 c)-f), pore size on the surface of outer layer decreases without deformation (from about 21.2 nm to 11.5 nm) with the increase in elongation rate. Moreover, after a certain high drawing speed (26.6 m/min), the apparent pore size seemed to keep unchanged at 11.5 nm. It is believed that the morphology of the outer skin presents detailed information of the effect of spinning conditions and determines the final results although the substructure under the apparent surface pore can affect the separation performance of the hollow fiber membranes. Therefore, it seems that the separation performance of the resultant hollow fiber membrane can be adjusted through changing elongation rate during dry-jet wet spinning.
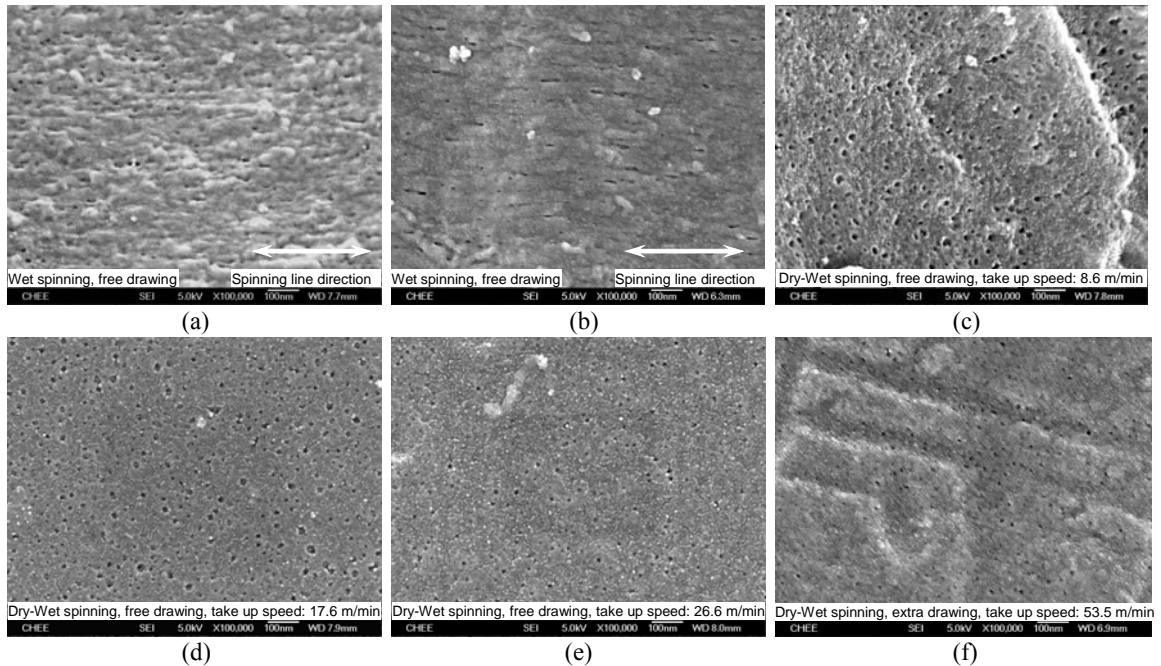
Fig. 2.18 Effects of shear rate and elongation rate on the morphology of the outer layer surface of the fabricated hollow fibers.   a) Wet spinning, dope flow rate: 0.25 ml min^{-1}; b) Wet spinning, dope flow rate: 2.0 ml min^{-1};   c), d), e) and f) Dry-jet wet spinning, dope flow rate: 2.0 ml min^{-1}

2.5. Discussion and Conclusions

In this part, effects of spinning conditions on the structure and separation performance of resultant hollow fiber membranes were studied. Two spinnerets with different flowing angles were used to investigate effect of spinneret design on the phase inversion process of polymer solution. Moreover, through increasing the shear rates and elongation rates, efforts were focused on eliminating finger-like macrovoids inside the resultant hollow fiber membranes. Hollow fiber membranes free of finger-like macrovoids can sustain higher operating pressures, which have potential application in the liquid separation.

From this research, ultrafiltration hollow fiber membranes could be fabricated without finger-like macrovoids under higher shear rates during wet spinning with the 90° straight spinneret. Moreover, it seemed that hollow fibers spun from the 60° flow angle had smaller mean pore size and higher geometric standard deviation, compared to those spun from the 90° flow angle, when the comparison was made at the same dope flow rates. Thus, flow angle within spinneret becomes another important factor in the improvement of the molecular packing by shear rate within spinneret, which can generate a denser and more selective skin.

Generally, polymeric hollow fiber membranes are fabricated from the phase inversion when a polymer solution is extruded from a spinneret to contact with coagulant. Many factors can influence the formation of hollow fiber membranes. Through increasing shear rates, these hollow fibers showed a minimum in the mean effective pore size resulting in the maximum separation performance, similar to others' work [Qin et al., 1999; Chung et

al., 2000]. The most probable reason may be that the dope solution with a high polymer concentration reveals different rheological behavior under low and high shear rate. There may be two opposing effects of the shear rate on the hollow fiber membranes. The first is that the molecular chains tend to align themselves better and pack more closely to each other, leading to a denser or higher selective skin. The other is a decrease in solution viscosity that may occur at high shear rates because of the reduction of coiled molecular chain entanglement (shear thinning). This is characteristic of a non-Newtonian power-law fluid, which consequently results in a looser skin. If the first factor is dominant, the membrane skin will become tighter at a higher shear rate, leading to a higher solute separation. If the second factor plays a competitive role after a certain shear rate, it may offset the impact from the first factor to facilitate a looser skin. The shear-rate induced molecular chain orientation and shear thinning effect of a higher concentration viscoelastic polymer dope solution play roles on the chain packing simultaneously.

Therefore, the shear rate may exert significant impact on the flux and the solute separation of hollow fiber membranes. The elongated pores on the outer layer surface also demonstrate the effects of shear rate on the alignment of polymer chain. Hollow fibers spun from the 90º straight spinneret have larger PWP values than hollow fibers spun from the 60º conical spinneret. This result confirms the enhanced packing of macromolecules brought about by the 60º flow angle at the outer surface.

So far, experiments have proven that shear rate affects the state of solution and phase separation [Wolf, 1984; Horst & Wolf, 1992], but few reports are available on elongation

effects. If there is an air gap before coagulation (dry-jet wet spinning), effects of elongation and relaxation will play important roles. The elongation stresses (mostly outside the spinneret) from gravity and spin line complicate the kinetics and dynamics of phase inversion. On the other hand, non-Newtonian polymer solutions may exhibit die swell and relaxation of the coiled polymeric macromolecular chains after exiting from spinneret. Therefore, through increasing elongational draw rates, the finger-like macrovoids in asymmetric hollow fiber membranes can be suppressed and even be completely eliminated at high elongational draws.

Four factors may have caused this dramatic morphology change from elongation draw:

1) Transformation of the state of spinning solution under a high speed spinning process, which may affect the formation of macrovoids [Ekiner & Vassilatos, 2001];

2) Extra phase instability and the facilitated spinnodal decomposition created by the external elongation stresses, which are relatively uniform across the membranes [Chung, 1997d];

3) Molecular chain packing induced by the high elongational rates [Cao et al., 2004], which may retard the penetration of external coagulant;

4) Radial outflow induced by the process of rapid shrinkage of fiber diameter during the elongational stretch, which hinders the capillary intrusion or diffusion of coagulants and eliminates the chance of forming finger-like macrovoids.

As a result, shear stress within the spinneret and elongation stress in the air gap can dramatically increase the molecular orientation and polymer chain packing, respectively,

and subsequently influence the phase inversion process since it has been confirmed that finger-like structure comes from instantaneous de-mixing while sponge-like structure comes from delayed de-mixing [Smolders et al. 1992]. Therefore, improved molecular orientation and packing will retard instantaneous phase inversion process, subsequently suppressing the formation of sponge-like macrovoids.

Since hollow fiber configuration is the favorite choice for industry membrane systems and hollow fibers with sponge-like macrovoids have potential application, this research may have great impact on membrane science and future membrane development. Future work should study the relationship of the flowing pattern and the fluid dynamics of the polymer solution under higher shear rates within the conical spinneret. For the conical (60º) spinneret, both axial velocity and radial velocity exist with unsteady fluid flow, which makes the rheological behavior of the non-Newtonian fluid complicated. Therefore, the orientation of polymer macromolecular chains induced by shear stress produced from the axial velocity gradient and the elongation of polymer macromolecular chains induced by the radial velocity gradient within the conical spinneret should be further studied.

Although the scheme of eliminating finger-like macrovoids through increasing shear rates and/or elongation rates can be applied to fabricate porous ultrafiltration hollow fiber membranes, for dense membranes, because of other related consideration based on the higher concentrated polymer solution, composition of the polymer solution may play a much important role on the structure of the hollow fibers.

CHAPTER THREE

CHARACTERIZATION OF TWO COMMERCIAL NANOFILTRATION MEMBRANES AND THEIR APPLICATION IN THE SEPARATION OF PHARMACEUTICALS

3.1. Introduction

This chapter will emphasize on the characterization and application of nanofiltration membranes in pharmaceutical separation. Pharmaceutical synthesis frequently produces intermediate reaction mixtures containing both organic compounds of different molecular weights and inorganic salts in the organic solvent or aqueous solutions. The subsequent separation and purification processes to extract the interesting product and organic solvent from mixture are crucial to increase product yield and quality. Because most pharmaceutical materials are thermally labile, special conditions are required to handle these intermediates or final products solutions if one uses conventional separation processes (i.e. distillation, ion-exchange and chromatography [Wang, et al., 2002]. Moreover, the molecular weights of most pharmaceuticals range from 300 to 1000 Da [Paul et al., 1990], which is in the scale of nanofiltration. Furthermore, membrane separation can be operated at the ambient temperature or even lower, which makes nanofiltration preferrable for the athermal solvent exchange in the pharmaceutical synthesis process. Nanofiltration has been adopted in the separation of amino acids and

peptides by varying pH [Tsuru et al., 1994; Li et al., 2003]. Amino acids having similar molecular weight but quite different pI (Isoelectric point, the pH at which a molecule carries no net electrical charge) can be separated by the NF membrane NTR 7410 [Rautenbach & Groschl, 1990]. Selective separation of 9 kinds of amino acids into acidic amino acids (pI below 3) and basic amino acids (pI above 9) was demonstrated using a charged inorganic nanofiltration membrane [Garem et al., 1997].

Compared with the traditional concentration processes, membrane-based separation technique may have an improved efficiency and reduced operating cost for the recovery and concentration of antibiotics [Rautenbach & VoBenkaul, 2001]. Different from traditional pharmaceutics syntheses in organic solvents, antibiotics are mainly produced by fermentation, and are harvested from the broths by selective solvent extraction and concentrated by vacuum distillation. Similar to amino acids, some antibiotics contain both amino and carboxyl groups. Depending on the solution pH, these groups determine the charge sign of the molecules.

Cephalexin, a semi-synthetic cephalosporin, was chosen in this study because it is therapeutically advantageous and important for its broad antibacterial activity. Cephalexin is a zwitterionic molecule containing amino group and carboxyl group and is synthesized either by the reduction of phenyleglycyl 7-ACA (7-aminocephalosporanic acid) with aminoacid esters or by the chemical or enzymatic acylation of 7-ADCA (7-amino 3-deacetoxycephalosporanic acid) [Maladkar, 1994]. The ionization states of cephalexin molecules vary with pH in the aqueous solution (Figure 3.1).

Characterization of Two Commercial Nanofiltration Membrane and
their Application in the Separation of Pharmaceuticals

Chapter III
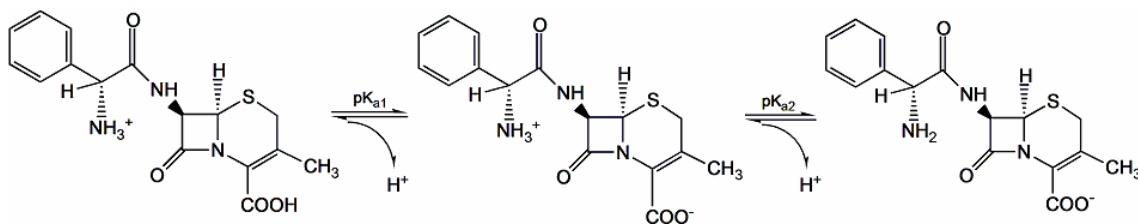
Fig. 3.1 Ionization states of cephalexin at different pH, pK_{a1} = 2.56, pK_{a2} = 5.88

The traditional solvent extraction cannot be used to recover it from fermentation broths. Sahoo [Sahoo et al., 1997 & 1998] studied non-dispersive reactive extraction using emulsion liquid membranes and bulk liquid membranes to recover cephalexin from dilute solutions. The extraction process was based on the pH dependence of cephalexin distribution ratio between membrane and aqueous phases. Supported liquid membranes separations have been extensively studied on the lab-scale [Ghosh et al., 1995; Wijers et al., 1998]. However, it seems difficult to be adopted in the large-scale industrial utilization due to certain problems related to the stability of liquid membranes although it can be increased by placing a thin polymer layer on top of the liquid membrane of the feed side [Strathmann, 2001]. Nanofiltration could be used to separate and purify the cephalexin aqueous solution by adjusting pH values. This study will investigate the separation performance of nanofiltration membranes for aqueous cephalexin solutions.

Characterization of Two Commercial Nanofiltration Membrane and
their Application in the Separation of Pharmaceuticals

Chapter III

3.2. Fundamentals of the characterization scheme of Nanofiltration membranes from solute separation data

Nanofiltration membranes can be characterized by the mean pore size and the pore size distribution obtained from neutral solute transport experiments [Nakao, 1994]. In general, the Stokes radius is used to describe the dimension of solutes for the evaluation of steric hindrance based on the assumption of rigid molecules with spherical shape. The Stokes radius of a macromolecule can be calculated from the Stokes-Einstein equation [Einstein, 1956]:

$$D_s = \frac{kT}{6 r_s \pi \mu} \tag{3.1}$$

where D_s is the diffusivity of solute molecule in a dilute solution (m^2/s), k is the Boltzmann constant, r_s is the Stokes radius of the solute (m), and μ is the solvent viscosity (the viscosity of water at 18°C is 1.056×10^{-3} N s m^{-2}). It is assumed that the diffusivity of solute in the membrane matrix is equal to that in bulk solutions approximately.

3.2.1 Real rejection obtained by concentration polarization model

Generally, the solute rejection performance is evaluated through the observed rejection:

$$R_{obs} = 1 - \frac{C_p}{C_b} \tag{3.2}$$

where C_p and C_b are solute concentrations in the permeate and bulk feed side, respectively. However, due to the effect of concentration polarization which decreases

Characterization of Two Commercial Nanofiltration Membrane and
their Application in the Separation of Pharmaceuticals

Chapter III

the driving force, the solute concentration C_m at the membrane surface is much higher than that in the bulk solution because of the reversible accumulation of the rejected solute when the permeate flux is large, as shown in Figure 3.2. Therefore, the real rejection R_T is defined as follows to represent the rejection ability of membranes:

$$R_T = 1 - \frac{C_p}{C_m} \tag{3.3}$$

Based on the concentration polarization model [Mulder, 1996], the permeate flux, J_v, is expressed as:

$$J_v = k' \ln \frac{C_m - C_p}{C_b - C_p} \tag{3.4}$$

where k' is the mass transfer coefficient in the polarized layer. Its value can be determined by varying the linear feed velocity, u_f, across the membrane:

$$k' = b u_f^a \tag{3.5}$$

where a and b are constants.
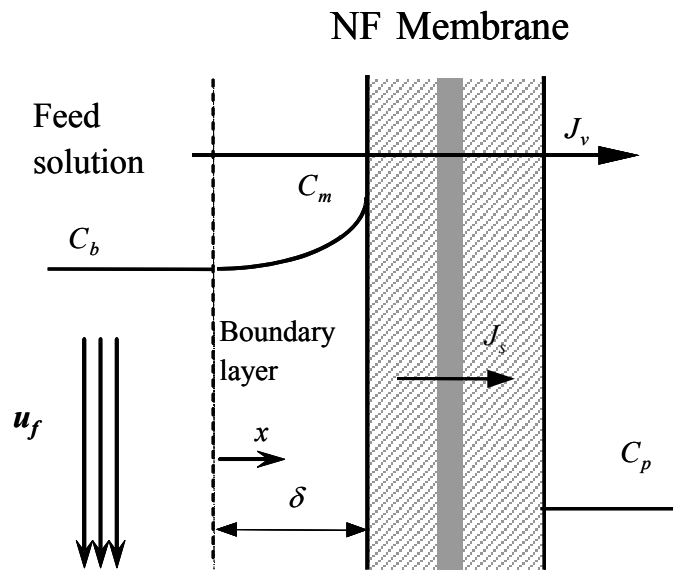
Fig. 3.2 Schematic of concentration polarization phenomena during membrane filtration

For turbulent flow in a channel, k' in the boundary layer may be expressed as [Schweitzer, 1988]:

$$Sh = \frac{k'd_h}{D_s} = 0.023 Re^a Sc^{1/3} \tag{3.6}$$

where d_h is the hydraulic diameter of channel, D_s the solute diffusion coefficient, Re the Reynolds number ($\rho d_h u_f/\mu$), Sc the Schmidt number ($\mu/\rho D_s$).

In order to determine the real rejection R_T, Eq. (3.4) can be rearranged as:

$$\ln \frac{1 - R_{obs}}{R_{obs}} = \ln \frac{1 - R_T}{R_T} + \frac{J_v}{bu^a} \tag{3.7}$$

When measuring R_{obs} at several different velocities with the same feed solution at the constant pressure, a linear plot of $\ln[(1 - R_{obs})/R_{obs}]$ vs. J_v/u^a can be obtained if the value of exponent a is correct, then the real rejection R_T is obtained from the intersection point by extrapolating the linear line to the ordinate axis of $J_v/u^a = 0$.

3.2.2 Irreversible thermodynamic model

Kedem and Katchalsky [1958] proposed the following transport equations to describe the permeating process through membrane based on the non-equilibrium thermodynamics:

$$\begin{cases} J_v = L_P(\Delta P - \sigma \cdot \Delta \pi) \\ J_s = P \cdot (c_f - c_p) + (1 - \sigma) \cdot J_v \bar{c} \end{cases} \tag{3.8}$$

where L_p, σ, P, π and $\bar{c}$ are the membrane parameters called pure water permeability, reflection coefficient, solute permeability, osmotic pressure and mean concentration over the thickness of membrane, respectively. Spiegler and Kedem [1966] expressed the flux

J_s of solute in a different form as follows if the concentration difference between the retentate and the permeate is high:

$$J_s = -P' \cdot (\frac{\mathrm{d}c}{\mathrm{d}x}) + (1-\sigma) \cdot J_v c \tag{3.9}$$

P' is the local solute permeability defined as $P' = P \cdot \Delta x$. Integrating above equation across the membrane thickness yields the rejection R_T, the Spiegler-Kedem equation becomes as follows:

$$R_T = 1 - \frac{c_p}{c_m} = \frac{\sigma(1-F)}{(1-\sigma F)} \tag{3.10}$$

where $F = \exp(-\frac{1-\sigma}{P} J_v)$. σ and P can be determined directly from experimental data of the real rejection R_T, as a function of J_v by any best-fitting method. Because the following relation is valid,

$$J_v \to \infty : R_T \to \sigma \tag{3.11}$$

the reflection coefficient σ corresponds to the maximum rejection at an infinitely high permeate volume flux when the filtration flow overtakes solute diffusion. However, the Irreversible thermodynamic model is not able to characterize the structural and electrical properties of the membrane because the membrane is assumed to act as a black box containing no description of molecule transport mechanisms.

3.2.3 Steric-hindrance pore model (SHP)

Nakao and Kimura [1982] proposed the steric-hindrance pore (SHP) model through modifying the pore model to calculate the pore radius and the ratio of membrane porosity

to thickness $A_k/\Delta x$:

$$\begin{cases} \sigma_s = 1 - S_F\{1 + (16/9)\eta^2\} \\ P_s = D_s \cdot S_D \cdot (A_k / \Delta x) \end{cases} \tag{3.12}$$

where S_F and S_D are steric hindrance factors for permeation flow and diffusion respectively when solute molecules transport through pores, η is the ratio of solute to pore diameter d_s/d_p, A_k is the membrane porosity, the ratio of total cross-sectional pore area to the effective membrane area, Δx is the effective pore length by assuming that the spherical solutes transport the cylindrical membrane pores.

$$\begin{cases} S_F = (1-\eta)^2[2 - (1-\eta)^2] \\ S_D = (1-\eta)^2 \end{cases} \tag{3.13}$$

Based on the SHP model, membrane structure parameters, pore radius r_p and $A_k/\Delta x$ can be obtained by using values of reflection coefficient σ and solute permeability P from the Irreversible thermodynamic model for each solute.

3.2.4   Effective volume charge density through the *TMS* model

The Teorell-Meyer-Sievers (TMS) model assumes that the ion concentration and electric potential have a uniform distribution in the radial direction in the membrane [Wang et al., 1995]. By combining the extended Nernst-Planck equation and the Donnan equilibrium theory, membrane parameters σ and P can be determined for a mono-mono type electrolyte as follows:

$$\begin{cases} \sigma_s = 1 - \dfrac{2}{(2\alpha - 1)\xi + (\xi^2 + 4)^{0.5}} \\ P_s = D_s(1 - \sigma_s)(A_k / \Delta x) \end{cases} \tag{3.14}$$

where ξ is defined as the ratio of effective volume charge density (ϕX) of membrane to

the electrolyte concentration (C_m) at the membrane surface.

3.2.5   Mean pore size and pore size distribution by the solute transport method

Nanofiltration membranes have molecular scale pores on their selective layer which

determine the permeate flux and sieving performance. It has been found that the solute

rejection for synthetic membranes can be expressed by a log-normal probability function

of solute size, as described in the following equation [Michaels, 1980]:

$$R_T = erf(y) = \frac{1}{\sqrt{2\pi}} \int_{-\infty}^{y} e^{-\frac{u^2}{2}} \, du, \quad where \quad y = \frac{\ln d_s - \ln \mu_s}{\ln \sigma_g} \qquad (3.15)$$

where R_T is the solute rejection, d_s is the solute diameter, μ_s is the geometric mean

diameter of solute at $R_T = 50\%$, σ_g is the geometric standard deviation about μ_s, defined

as the ratio of d_s at $R_T = 84.13\%$ and $R_T = 50\%$. When the solute rejection factor of a

nanofiltration membrane is plotted vs. solute diameter on a log-normal probability paper,

a straight line is obtained as:

$$F(R_T) = A + B (\ln d_s) \qquad (3.16)$$

The values of μ_s and σ_g determine the position and sharpness of the rejection curves,

respectively. By considering the steric and hydrodynamic hindrance effects of the pore on

solute molecules, and neglecting the deformation of macromolecules under pressure and

shear rate [Youm & Kim, 1991; Nguyen & Neel, 1983], the solute rejection can be

written in terms of η ($\eta = d_s/d_p$, the ratio of solute diameter to pore diameter) [Zeman &

Characterization of Two Commercial Nanofiltration Membrane and
their Application in the Separation of Pharmaceuticals

Chapter III

Wales, 1981]:

$$R_T = 1 - \{1 - [\eta(\eta - 2)]^2\}\exp(-0.7146\eta^2) \qquad (3.17)$$

Thus, at $R_T = 50\ \%$ (i.e. $\eta = 0.416$), the mean pore diameter can be calculated by:

$$d_p = \frac{\mu_s}{0.416} \qquad (3.18)$$

Therefore, based on d_p and σ_p, the pore size distribution of a NF membrane can be expressed as the following probability density function [Aimar et al., 1990] by the derivative of the equation (15) with respect to R_T:

$$\frac{\mathrm{d}\,R_T(d_p)}{\mathrm{d}\,d_p} = \frac{1}{d_p \ln \sigma_p \sqrt{2\pi}} \exp\left[-\frac{(\ln d_p - \ln \mu_p)^2}{2(\ln \sigma_p)^2} \right] \qquad (3.19)$$

The approach has been used to evaluate the mean pore size, the pore size distribution and the porosity from the solute separation data of aqueous PEG solutions with different molecular weights as the feed solutions in UF experiments [Singh et al., 1998].

3.3. Experimental

3.3.1. Chemicals

Uncharged neutral solutes, glycerol, glucose, saccharose, raffinose and PEG 1000, from Aldrich, USA and several analytical-grade salts, NaCl, $MgCl_2$, $MgSO_4$ and Na_2SO_4, from Merck, Germany, were used to characterize membrane structure parameters. Molecular weight, diffusivities and Stokes radii of these solutes are shown in Tables 3.1 [Bowen & Mohammad, 1998; Newman, 1991]. NaOH (1.0 N) and HCl (1.0 N) solutions were used to modify the pH of feed solutions. **Cephalexin**, $C_{16}H_{17}N_3O_4S \cdot H_2O$, MW 365.4, a white crystalline powder, was purchased from MP Biomedical Inc., Germany. All chemicals were used as received in experiments without further purification. The pure water used in all experiments was produced by a Milli-Q unit (MilliPore, USA) with a resistivity of 18 $M\Omega$ cm. The temperature of feed solution in all experiments was maintained at $18 \pm 0.1°C$ by a cooling coil (controlled by a water circulator, Julabo F32-MV, Germany) inside the feed tank.

Table 3.1 Diffusivities and Stokes radii of neutral solutes in aqueous solutions (at 18ºC)

Solute	MW or M_w [g·mol^{-1}]	D_s [×10^{-9} m^2·s^{-1}]	r_s [nm]
Glycerol	92	0.78	0.260
Glucose	180	0.57	0.365
Saccharose	342	0.43	0.471
Raffinose	504	0.35	0.584
PEG 1000	1000	0.21	0.784
NaCl	58.5	1.33	0.152

3.3.2. Composite Nanofiltration Membranes

Two commercial flat sheet nanofiltration membranes, NADIR$^®$ N30F and NF PES-10 were supplied by NADIR Filtration GmbH (Wiesbaden, Germany). The selective layer of these composite membranes was made of permanently hydrophilic polyethersulfone-polyvinylpromidone copolymer on the polypropylene support (Ernst et al., 2000). The information of membranes provided by the supplier is summarized in Table 3.2.

Table 3.2 Nadir$^®$ Nanofiltration membranes characteristics provided by supplier

*Membrane		N30F	NF PES 10
Material of separating layer		Hydrophilic	Hydrophilic
Pure water flux	$(l\,m^{-2}\,hr^{-1})$	40 - 70	200 - 400
MWCO	(Da)	400	1000
NaCl rejection	(0.5 %)	25 - 35	10 - 20
Na_2SO_4 rejection	(1.0 %)	85 - 95	40 - 70
Lactose retention	(4.0 %)	70 - 90	30 - 50
pH range	(-)	0 - 14	0 - 14
Max. temperature	(ºC)	95	95

*Test conditions: 40 bar, 20°C, stirred cell (700rpm)

3.3.3   Experimental set-up

Nanofiltration experiments were conducted in a consecutive lab-scale filtration unit, described in Chapter II, which contains a cross-flow permeation cell with the effective filtration area of 17.35 cm^2 supported by the porous stainless steel disc. The detail of the

permeation cell is shown in Figure 3.3. The temperature of feed solution in all experiments was maintained at 18°C by a cooling coil inside the feed tank. The trans-membrane pressure was varied from 0 bar to 25 bar. Pressures and feed flow rates were adjusted through controlling the back pressure valves and bypass valves. The retentate and permeate flow back into the feed tank to form a closed cycle, which can make feed concentration constant approximately.

Fig. 3.3 Diagram of nanofiltration permeation cell

3.3.4 Chemical analysis

The concentrations of neutral solute and Cephalexin solutions were measured with a total organic carbon analyzer (TOC ASI-5000A, Shimazu, Kyoto, Japan). The concentration of single electrolyte solutions was measured with an electric conductivity meter (Horiba

ES-12, Japan). The concentrations of different ions in electrolyte mixtures were measured with ion selective electrodes (Na^+ and Cl^- combination electrodes, Orion). The pH of solution was measured by a pH meter (Orion PerpHect pH meter 370, USA). The composite membranes were immersed in liquid nitrogen and fractured, and then sputtered with platinum using a Jeol JFC-1100E Ion Sputtering device. The surface and cross-section morphology were observed under SEM (JEOL JSM-5600LV).

3.3.5 Experimental procedure

The experimental procedures were as follows:

1) Each membrane sample was firstly subjected to compaction at about $\Delta P = 22$ bar for 12 hrs by filtering pure water, then the pure water permeate flux was measured at different pressures.

2) The feed solutions were prepared by dissolving neutral solutes in pure water at a concentration of 200 ppm except for those otherwise specified. The feed solution was circulated for about 0.5 hr. The permeate was collected for a predetermined period and the volume flux was measured before being subjected to analysis at a constant pressure (starting from the lowest ΔP) and different circulation flowing rates (starting from the highest rate); then filtration was performed at another pressure.

3) The nanofiltration experiments were carried out with solutes of progressively higher molecular weights. The membrane was thoroughly flushed with pure water between runs of different solutes. The solute separation data were further used for estimating the mean pore size and the pore size distribution of the membrane.

Characterization of Two Commercial Nanofiltration Membrane and
their Application in the Separation of Pharmaceuticals

Chapter III

4) The electrolyte solutions were prepared by dissolving single salts in the pure water with the concentration of 1.7 mol m^{-3}. The same procedure was employed to measure the salts rejection performance as step (2).

5) NaCl solutions with different concentrations were prepared. The salt rejection by membranes was measured at different pressures.

6) The NaCl/Na$_2$SO$_4$ binary salt mixture solution was prepared. The ion rejection performance of membranes was measured at different pressures and a constant circulation rate.

7) Cephalexin solutions at different pH were prepared, the solute rejection experiments were performed as the same as the step (2). The effect of NaCl concentration on the cephalexin separation was also investigated at pH = 7.1.

3.4. Results and discussion

3.4.1. Morphology of NF flat sheet membranes

Figure 3.4 shows the morphology of the two composite membranes. Macroscopically, these two membranes have similar structures. Both consist of three layers: 1) a non-woven fabric support, 2) a middle layer full of finger-like macrovoids near the bottom and sponge-like pores near the top layer, and 3) a dense selective layer with a thickness of around 40 and 20 nm for N30F and NF PES10, respectively. Even at a magnification ratio of 50 000, no visible pores can be observed for both NF membranes.

N30F membrane

Bottom   Cross-section   Cross-section of top layer   Surface

NF PES10 membrane

Bottom   Cross-section   Cross-section of top layer   Surface
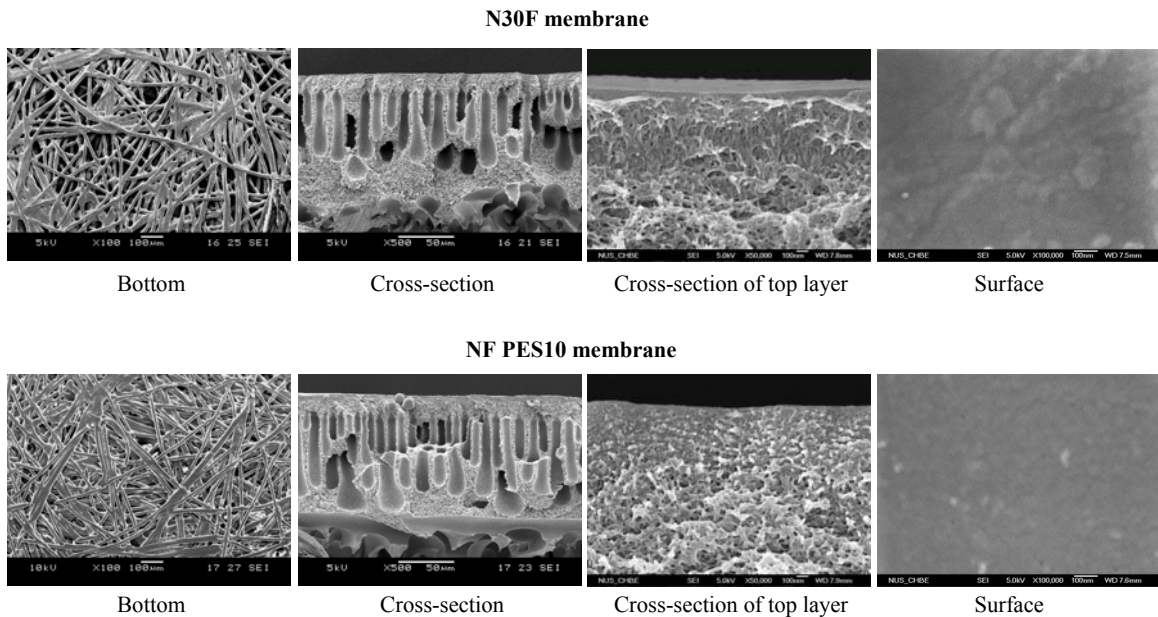
Fig. 3.4 Morphology of the nanofiltration composite membranes from SEM
(Scale bar: 100μm, 50μm, 100nm, 100nm from left to right)

3.4.2 Permeate flux and the separation performance as to neutral solutes

Permeate flux through the tested membranes as a function of applied pressure follows the

Hagen-Poisseuille equation:

$$L_p = J_v / \Delta P = \frac{r_p^2}{8\mu} \frac{A_k}{\Delta x} \tag{3.20}$$

The pure water permeability of N30F and NF PES-10 are 1.83 liter m^{-2} bar^{-1} hr^{-1} and 7.38 liter m^{-2} bar^{-1} hr^{-1}, respectively.

The relationship between Stokes radius r_s and M_w established for known solutes (glycerol, glucose, saccharose, raffinose, PEG1000) can be fitted by the following expression:

$$\log r_s = -1.4854 + 0.461 \log M_w \tag{3.21}$$

where r_s is in nm and M_w is in g mol^{-1}. From this equation the radius for a hypothetical solute at a given M_w can be back calculated.

In order to obtain the structure parameter (r_p and $A_k/\Delta x$), the real solute rejection R_T is firstly obtained from the observed rejection R_{obs} as a function of circulation flow rate and applied pressure. The real rejection corrected by the concentration polarization model as a function of Stokes radius for different solutes is obtained in Figure 3.5 at different pressures, which shows the dependency of the real rejection of membrane on permeate flux. Based on the Spiegler-Kedem Eq. (10), the membrane parameters (σ and P) can be determined by a best-fit method and results are listed in Table 3.3. Through reverse calculating by the SHP model of Eq. (12) and (13) from membrane parameters (σ and P), the average pore radii (r_p) of N30F and NF PES-10 membranes, are estimated to be 0.74 and 1.33 nm, respectively, as shown in Table 3.3 together with $A_k/\Delta x$ values. The $A_k/\Delta x$ value increases with increasing solute size which is similar to other research results

[Bowen & Welfoot, 2001]. This phenomenon is due to the fact that NF membranes

consist of a bundle of interconnected cylindrical capillaries with structural parameters

(pore radius r_p and the ratio of membrane porosity to membrane thickness $A_k/\Delta x$).

N30F membrane

NF PES 10 membrane
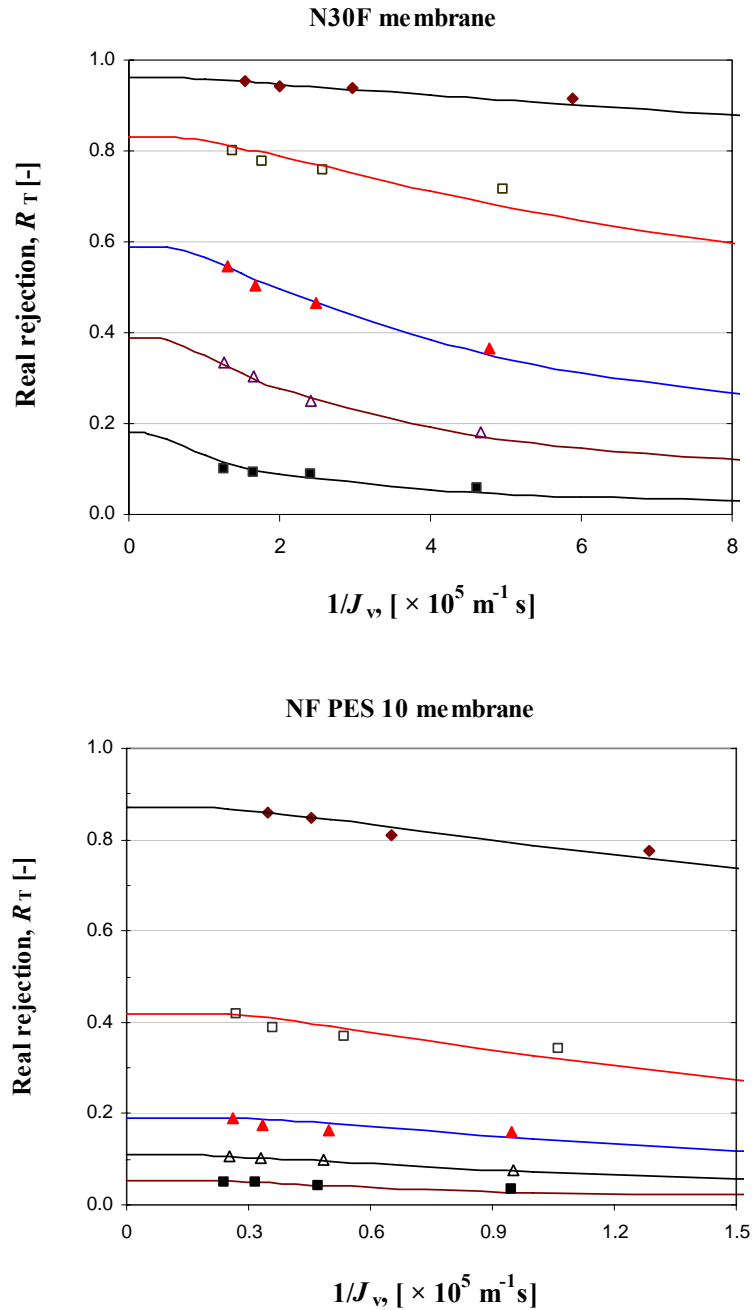
Fig. 3.5 Real rejection of NF membranes as a function of permeate flux (at 5, 10, 15 and 20 bar)
with different solutes. The curves were fitted by the Spiegler-Kedem equations.
(Feed concentration: 200 ppm, ♦ PEG 1000 □ Raffinose ▲ Saccharose △ Glucose ■ Glycerol)

Table 3.3 Membrane parameters (σ and P) by neutral solutes transport experiments from Spiegler-Kedem equations, r_p and $A_k/\Delta x$ of NF membranes determined from the SHP model

Solute	N30F membrane					NF PES10 membrane				
	σ [-]	P [3 10^{-6} m·s^{-1}]	r_p [nm]	η [r_s/r_p]	$A_k/\Delta x$ [m^{-1}]	σ [-]	P [3 10^{-6} m·s^{-1}]	r_p [nm]	η [r_s/r_p]	$A_k/\Delta x$ [m^{-1}]
Glycerol	0.17	7.10	0.78	0.33	20,377	0.06	11.5	1.45	0.17	25,806
Glucose	0.39	3.30	0.71	0.52	24,667	0.11	8.81	1.40	0.26	28,302
Saccharose	0.59	1.80	0.73	0.65	33,254	0.19	6.51	1.34	0.35	36,055
Raffinose	0.83	0.60	0.73	0.80	41,936	0.40	4.21	1.12	0.52	52,866
PEG 1000	0.96	0.14	0.73*	1.08	–	0.87	1.61	0.69*	1.14	–
average			0.74		30,058			1.33		35,757

* These data were not used for calculating average r_p.
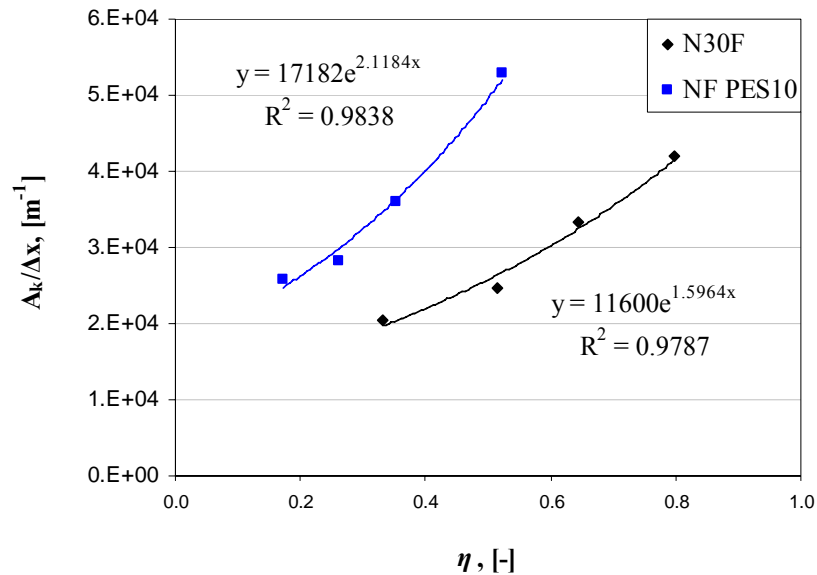
Fig. 3.6 Calculated $A_k/\Delta x$ determined from the SHP model as a function of η (r_s/r_p)

Due to the steric hindrance effect, larger solutes cannot enter into smaller pores and will have shorter transport paths in the matrix of the porous membrane, while smaller solutes and water molecules can pass though more pores and have longer paths [Bowen et al.,

997]. As a result, Figure 3.6 shows that the calculated $A_k/\Delta x$ determined from the SHP

model increases with η (the ratio of solute diameter to pore diameter).

If substituting the calculated r_p from the SHP model into Eq. (3.20), the $A_k/\Delta x$ values for

N30F and NF PES-10 membranes based on the pure water permeability are 78, 851 m^{-1}

and 97 905 m^{-1}, respectively, which are larger than those calculated directly from the

SHP model. This phenomenon is probably due to the fact that the value of A_k for water

molecules is much larger than those for the solutes because A_k is not an inherent

membrane constant but dependent on physicochemical properties of permeants.

3.4.3   Mean pore size and pore size distribution

In order to calculate these two important data, the solute rejection vs. solute Stokes radius

curves were plotted on a log-normal probability graph at two different pressures of 10

and 20 bar, as illustrated in Figure 3.7, to fit Eq. (3.16). Straight line relationships are

formed with reasonably high correlation coefficients ($r^2 > 0.95$). Therefore, the mean

solute radius μ_s at $R_T = 50$ %, and σ_g, the geometric standard deviation about μ_s, can be

obtained from the plots. Substituting the mean solute radius μ_s into Eq. (3.18), one

obtains the mean pore size d_p.

The molecular weight cutoff (MWCO, $R_T = 90$ %) can also be calculated from these

straight lines and Eq. (3.21), as shown in Table 3.4. At different pressures, the calculated

mean pore sizes have small differences because the solute rejection will increase with

increasing pressures. The water permeate flux through the membrane is linearly related to

the pressure difference applied, whereas the solute flux is both dependent on the

concentration difference over the membrane and on the water flux. When increasing the

pressure difference, the water flux increases relatively more than the solute flux. This

causes a decreasing permeate concentration and an increasing rejection [Peeters, 1997].
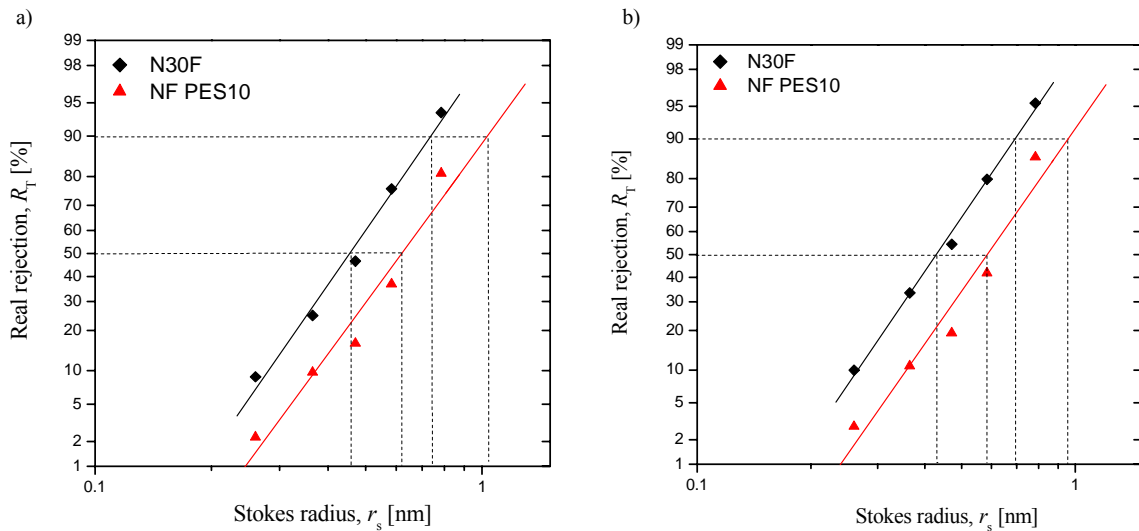
Fig. 3.7 Real rejection curves (solute rejection versus Stokes radii) plotted on the
log-normal probability ordinate system at the pressures of a) 10 bar; b) 20 bar

Table 3.4 Mean pore size (μ_p) and geometric standard deviation (σ_p) for NF membranes
calculated from solute separation data

Membrane	Pressure [bar]	Mean pore diameter μ_p [nm]	Geometric Std. Dev. σ_p [-]	MWCO [Da]
N30F	10	2.21	1.45	868
	20	2.07	1.47	782
NF PES10	10	2.98	1.48	1,816
	20	2.79	1.49	1,510

N30F membrane
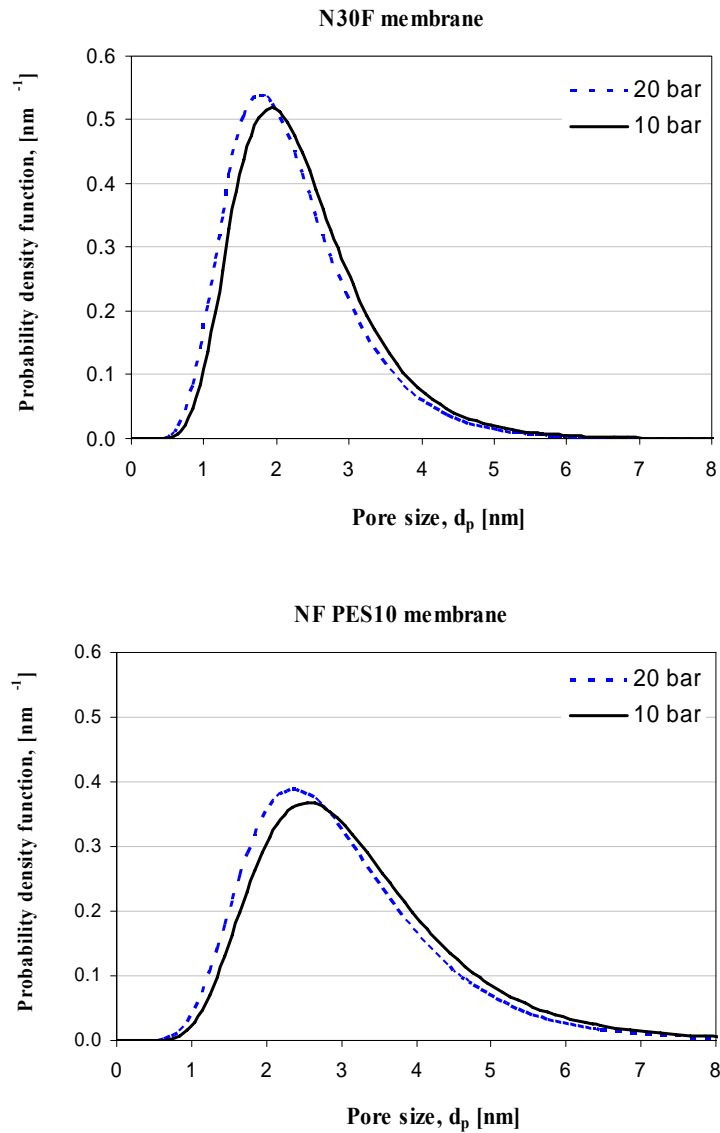
NF PES10 membrane

Fig. 3.8 Probability density function curves for (a) N30F, (b) NF PES10 membranes
at different pressures of 10 bar and 20 bar

The mean pore size from different solutes rejection is quite similar to the value from the

average membrane parameter obtained from the SHP model previously discussed in the

Section 4.2. The pore size distributions of two NF membranes calculated by Eq. (3.19)

are represented in Figure 3.8. It is found that in the Michaele's model the pore size

distribution varies with the operating pressure due to the possible plugging and deformation of membrane pores.

3.4.4   Membrane characterization using single electrolyte solution

NaCl solutions with different concentrations from 1.7 mol m^{-3} to 153.8 mol m^{-3} were used to measure the membrane rejection at different pressures. At high NaCl concentration the permeate product (permeate flux over pressure) decreases slightly compared to the pure water permeability due to the decreased driving force brought by the increased osmosis pressure of feed. The NaCl rejection decreases along with the increasing NaCl feed concentration at different pressures as shown in Figure 3.9, which can be explained by the anion screening effect on the membrane charge density. Through fitting the real rejection data to the Spiegler-Kedem model, membrane parameters (σ and P) can be determined from Figure 3.10.

Based on the TMS model from Eq. (3.14), the effective charge density (ϕX) of two NF membranes can be determined from σ at different NaCl concentrations. It seems that the membrane with a smaller pore size has higher effective charge density. It has been confirmed that the effective charge density varies with the salt concentration [Wang et al., 1995; Bowen et al., 1997; Afronso & de Pinho, 2000, Schaeo et al., 1998]. At a higher NaCl concentration, the membrane seems to have a larger calculated charge density. The effective charge density ϕX can be related to NaCl concentration by the following empirical Eq. (3.22) as shown in Figure 3.11.

$$\phi X = \text{constant}\, C_m^n \qquad\qquad (3.22)$$

N30F membrane

NF PES 10 membrane
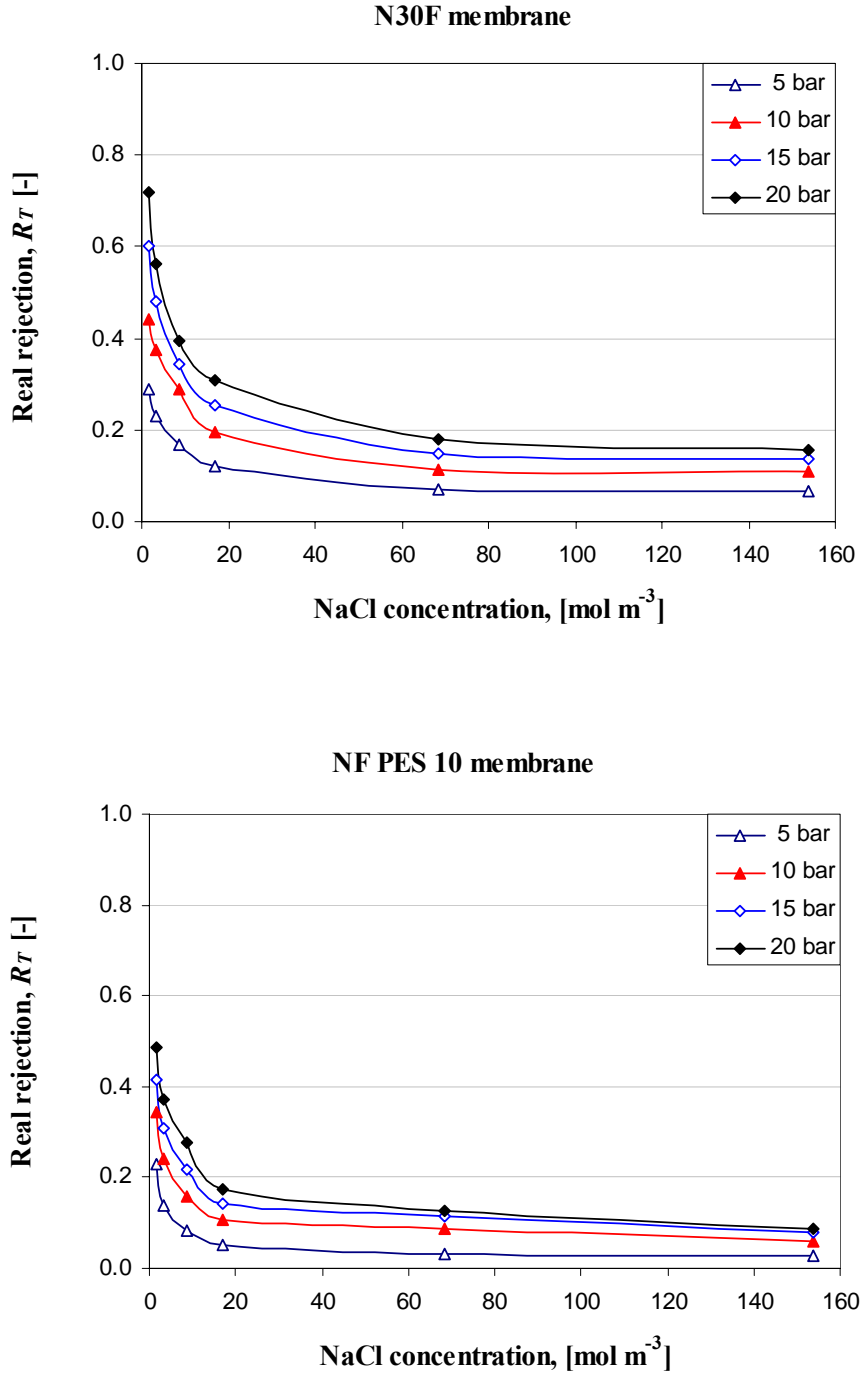
Fig. 3.9 Real rejection of NaCl against salt concentration at different pressures

N30F membrane

NF PES10 membrane
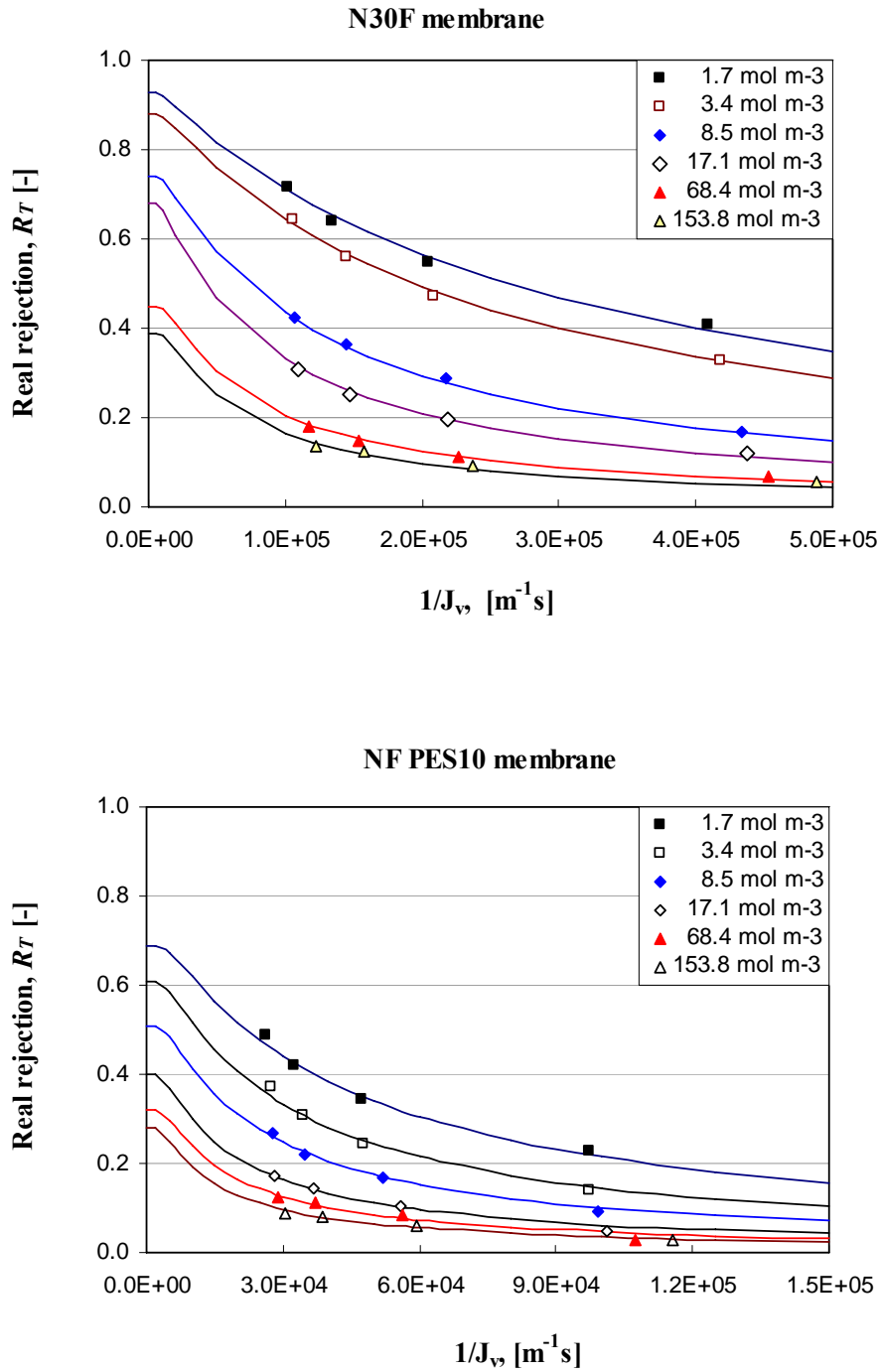
Fig. 3.10 Real rejection as a function of permeate volume flux J_v with different NaCl concentrations
The curves were fitted by the Spiegler-Kedem equations.
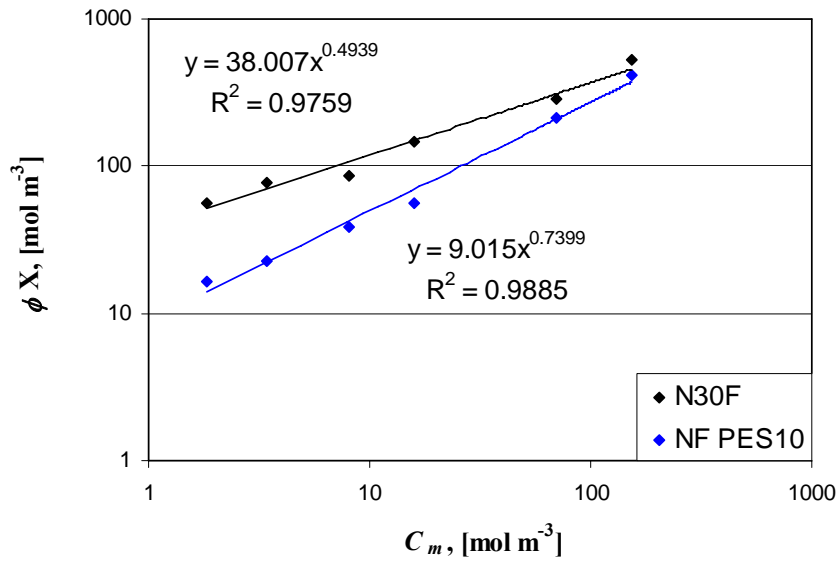
Fig. 3.11 Effective charge density (ϕX) as a function of bulk NaCl concentration
The curves are fitted according to Eq. (3.22)

Because the NF membranes are negatively charged, they show different rejection to different valent anions and cations. At the same molar concentration, the real rejection of four kinds of electrolytes are measured at different pressures, as shown in Figure 3.12, in the order of R (Na$_2$SO$_4$) > R (MgSO$_4$) > R (NaCl) > R (MgCl$_2$). The membranes show higher rejection to divalent anions with higher co-ion charge than monovalent anions, and lower rejection to divalent cations with higher counter-ion charge due to the negatively charged properties of membrane, which corresponding with Donnan exclusion.
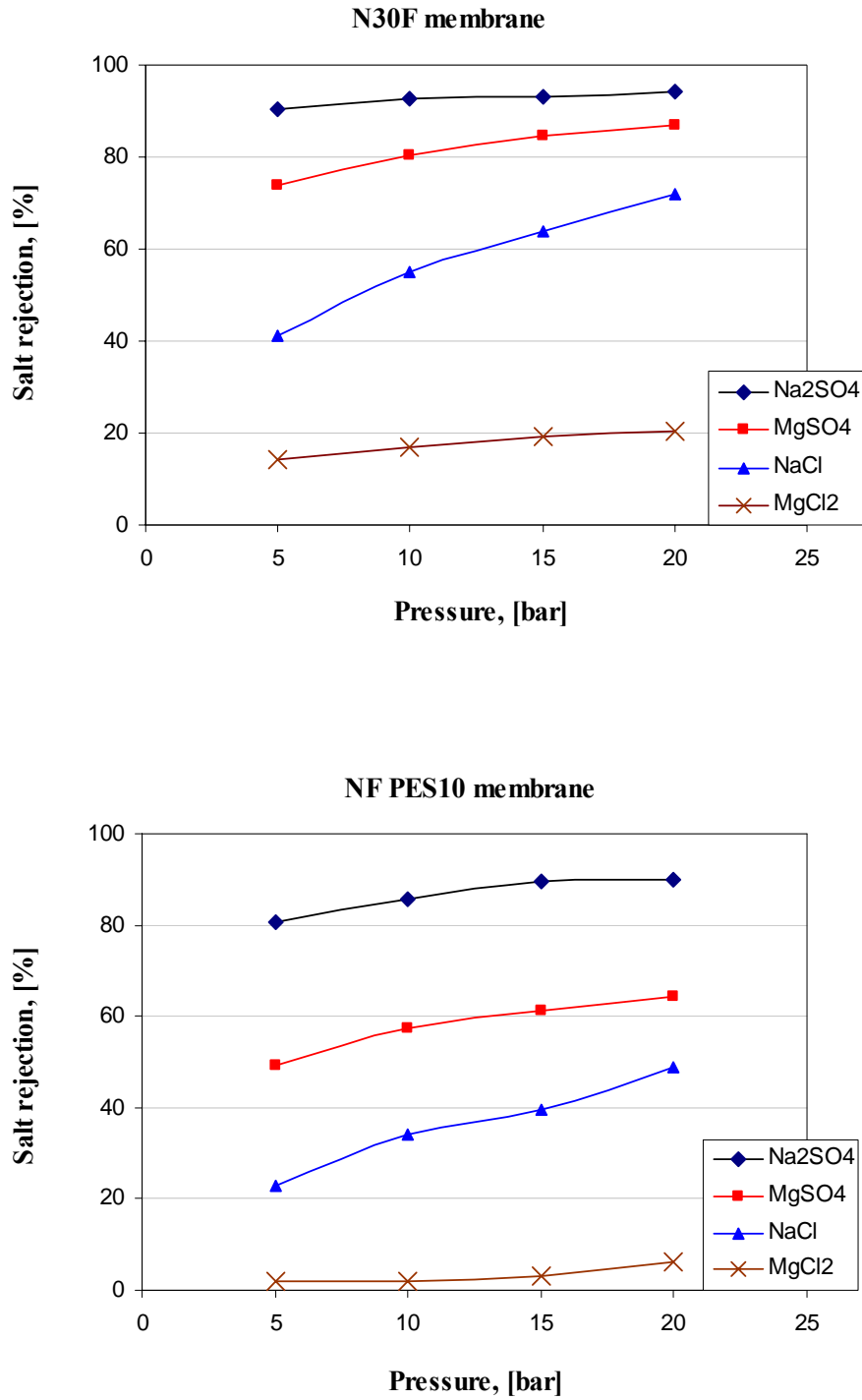
Characterization of Two Commercial Nanofiltration Membrane and
their Application in the Separation of Pharmaceuticals

Chapter III

N30F membrane

NF PES10 membrane

Fig. 3.12 The Real rejection of different salts at different pressures
(the bulk single salt concentration: 1.7 mol m^{-3})

N30F membrane

NF PES10 membrane
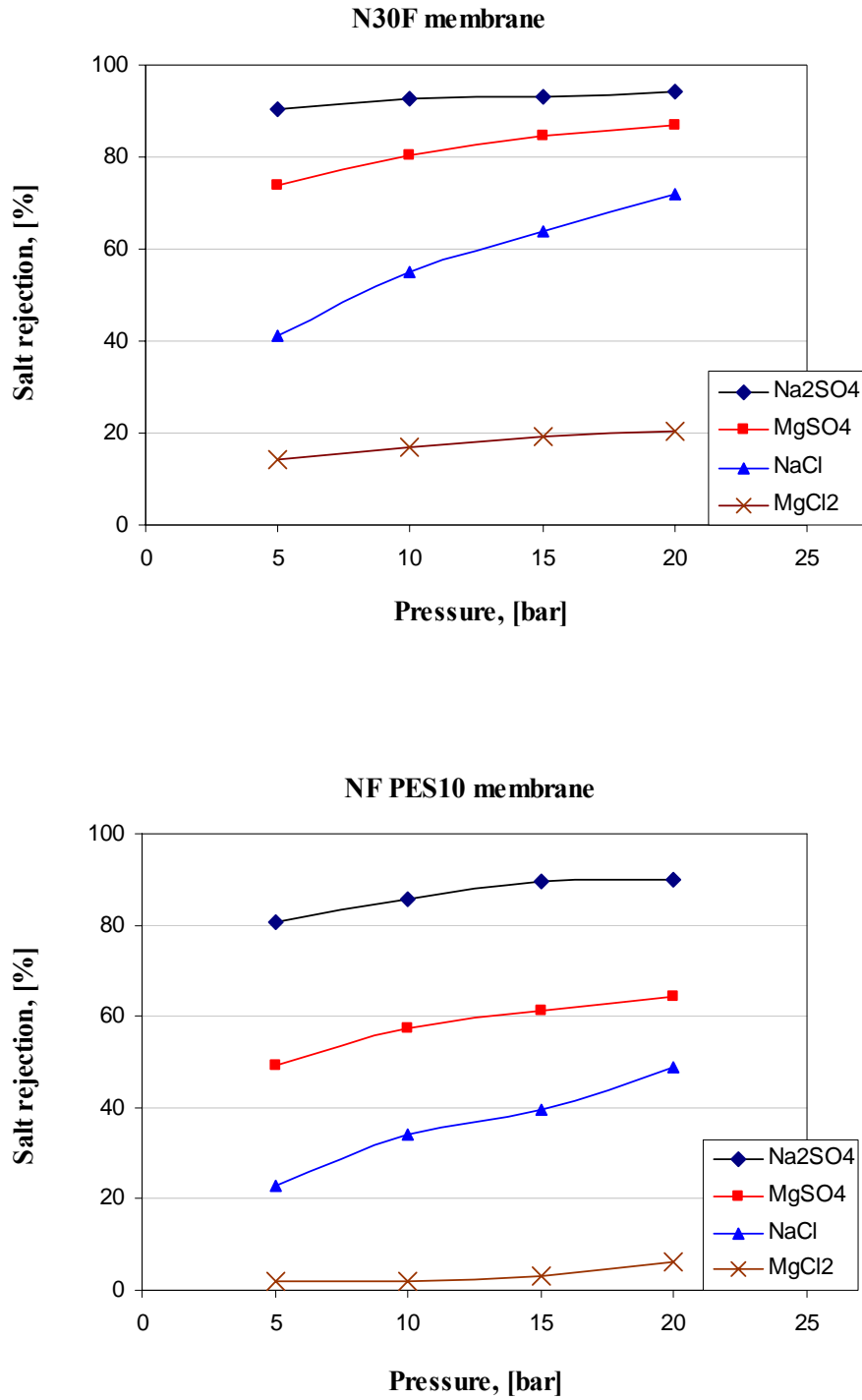
Fig. 3.12 The Real rejection of different salts at different pressures
(the bulk single salt concentration: 1.7 mol m^{-3})

3.4.5   Ion rejection of NF membrane for the electrolyte mixture solutions

In the Na_2SO_4/NaCl binary salt mixture solution with an anion molar concentration ratio SO_4^{2-}/Cl$^-$ of 2.0, Cl$^-$ ions are forced to permeate preferentially compared to SO_4^{2-} ions since Cl$^-$ has a lower valence. Na$^+$ ions also permeate membrane together with Cl$^-$ to maintain electroneutrality at both sides of the membrane in accordance with the Donnan principle. The negative rejection of chloride ions was observed at a low applied pressure as shown in Figure 3.13, which is consistent with others' research [Perry & Linder, 1989]. Along with the increasing pressure, the rejection of Cl$^-$ increases because the increased permeate flux in the pore plays an important role [Garcia-Aleman & Dickson, 2004]. The SO_4^{2-} ion and Cl$^-$ ion could be effectively fractionated by these negatively charged NF membranes.

In the NaCl/$MgCl_2$ binary salt mixture solution with a cation molar concentration ratio Mg^{2+}/Na$^+$ of 2.0, Mg^{2+} ions are attracted by the negatively charged membrane and are forced to permeate preferentially compared to Na$^+$ ions since Na$^+$ has a lower valence. Cl$^-$ ions also permeate membrane together with Na$^+$ to maintain electroneutrality at both sides of the membrane, in accordance with the Donnan principle. The ion rejection is shown in Figure 3.14. The membrane also showed low rejection to Cl$^-$ due to the screening effect of Mg^{2+} for its higher positive valence. Along with the increasing pressure, the rejection of Na$^+$ increases because the increased permeate flux in the pore plays an important role. The Mg^{2+} and Na$^+$ cations are difficult to be fractionated by these negatively charged NF membranes.

Characterization of Two Commercial Nanofiltration Membrane and
their Application in the Separation of Pharmaceuticals

Chapter III

N30F membrane

NF PES10 membrane
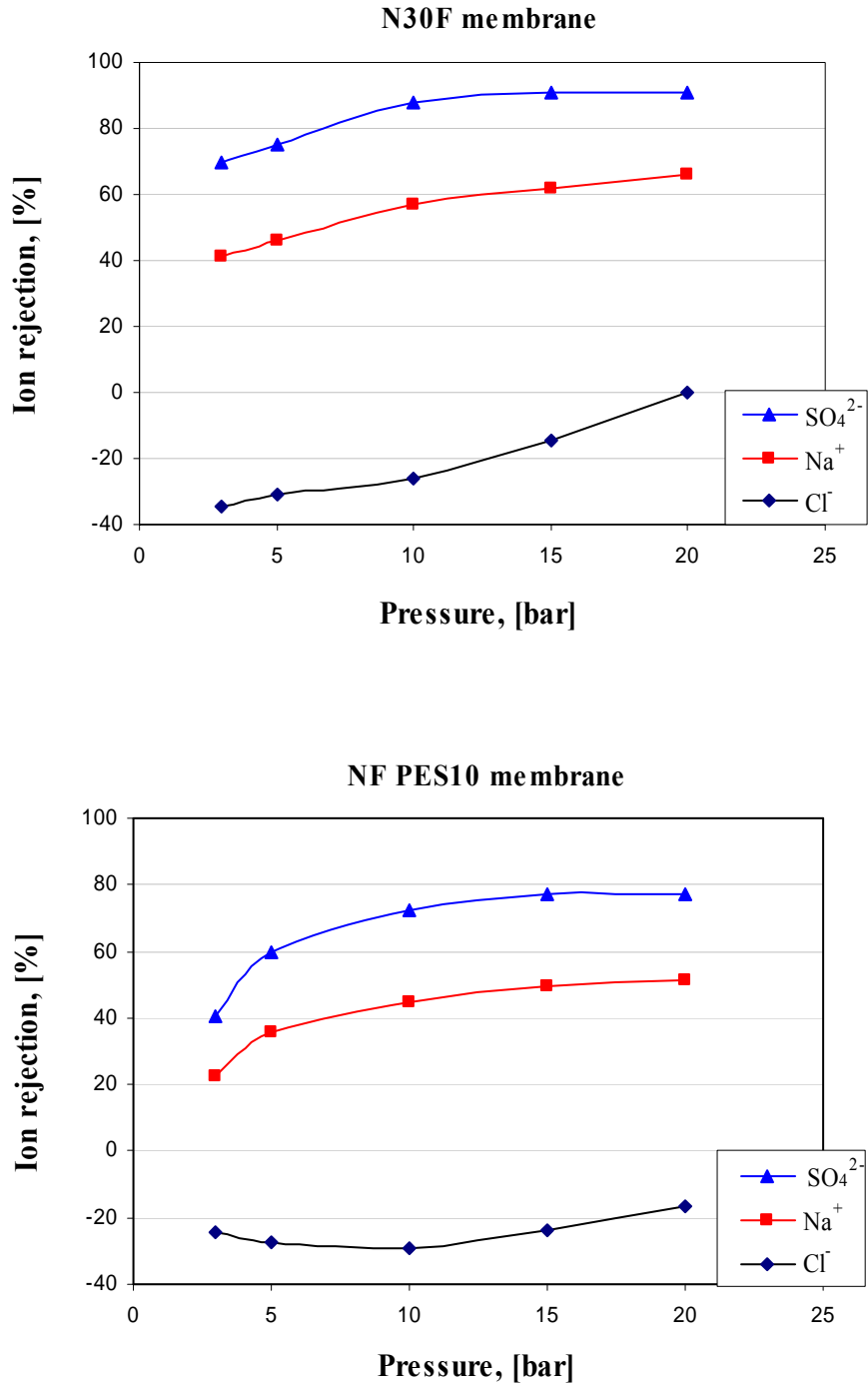
Fig. 3.13 Ion rejection in the mixture of $NaCl/Na_2SO_4$ solution as a function of applied pressure
($[NaCl]$ = 1.7 mol m^{-3}, $[Na_2SO_4]$ = 3.4 mol m^{-3})

104

Characterization of Two Commercial Nanofiltration Membrane and
their Application in the Separation of Pharmaceuticals

Chapter III

N30F membrane

NF PES10 membrane
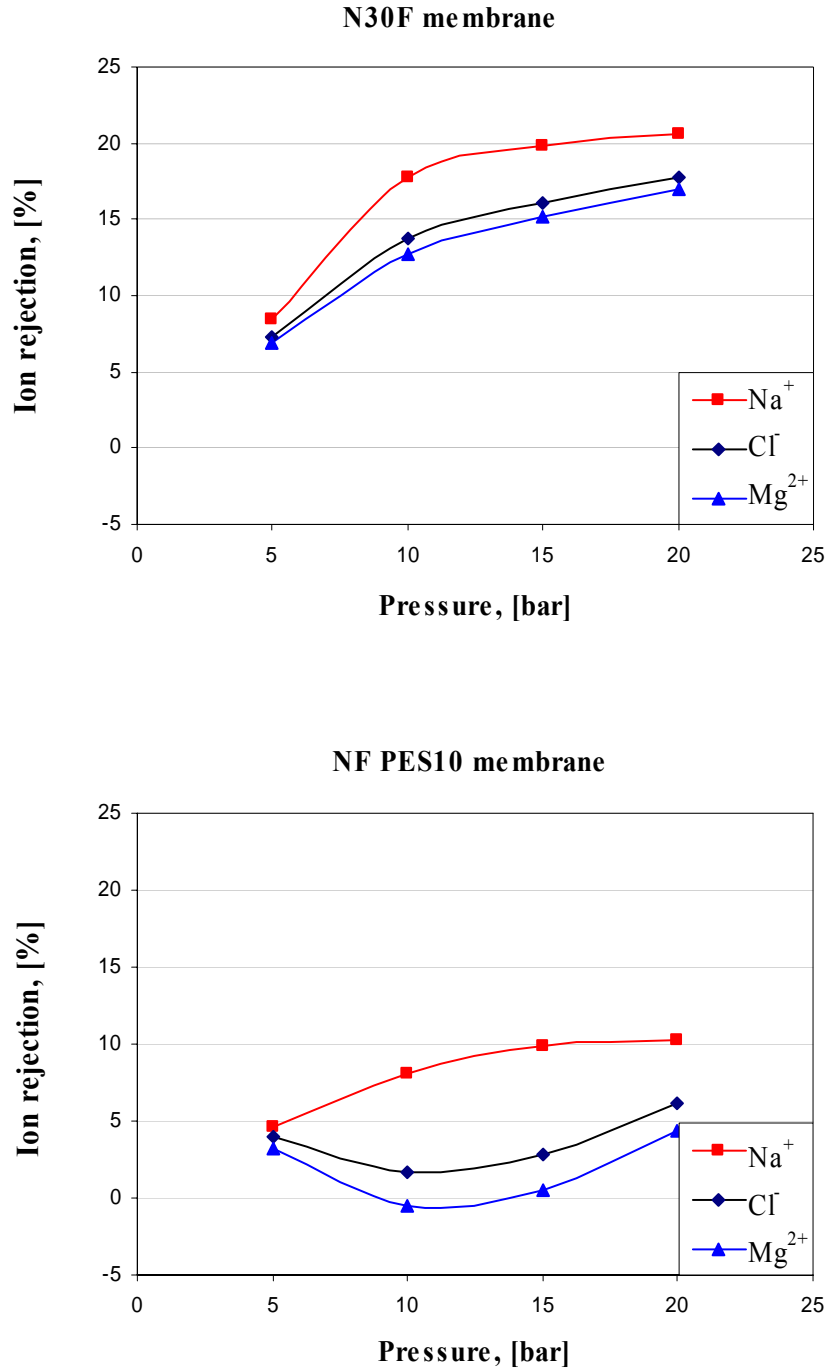
Fig. 3.14 Ion rejection in the mixture of NaCl/MgCl$_2$ solution as a function of applied pressure
([NaCl] = 1.7 mol m^{-3}, [MgCl$_2$] = 3.4 mol m^{-3})

3.4.6   Cephalexin separation performance of NF membranes

As an amphoteric electrolyte molecule in the aqueous solution, cephalexin acts as both basic (proton acceptor) and acid (proton donor) since cephalexin molecules have the amino group ($-NH_2$) and the carboxyl group ($-COOH$). Depending on the solution pH, cephalexin can be positively charged (acidic) at pH < pI (Isoelectric point, around 4.5 ~ 5.0), negatively charged (basic) at pH > pI and net neutral (dipolarions) at pH = pI. In the dipolar form, the amino group is pronated ($-NH_3^+$) and the carboxyl group is dissociated ($-COO^-$). Based on their dissociation constants (pK_as), the fraction of different ionization states of cephalexin at different pH can be expressed by the Henderson-Hasselbalch equation [Stryer, 1995] plotted on Figure 3.15 (the dashed curves):

$$\mathrm{p}H = \mathrm{p}K_a + \log(\frac{[\text{proton acceptor}]}{[\text{proton donor}]}) \tag{3.23}$$

As shown in Figure 3.15, the real rejection of cephalexin increases with an increase in pH at different pressures for two NF membranes. For N30F membrane with a small pore size, it shows higher rejection than NF PES10 membrane. Above a pH of 6.0, N30F expresses a sharp increase in rejection and cephalexin was 98 % rejected (20 bar) at pH 10; while for NF PES10 membrane, there is a sharp increasing rejection after pH 7.0 and cephalexin is 88 % rejected (20 bar) at pH 10. This shows that cephalexin rejection is dependent on the pore size (steric exclusion) and electrostatic interaction between solutes and membrane. The solution pH has the dominant effect on separation because pH determines the ionization states of cephalexin molecules and the surface charge density of the membrane.

N30F membrane

NF PES10 membrane
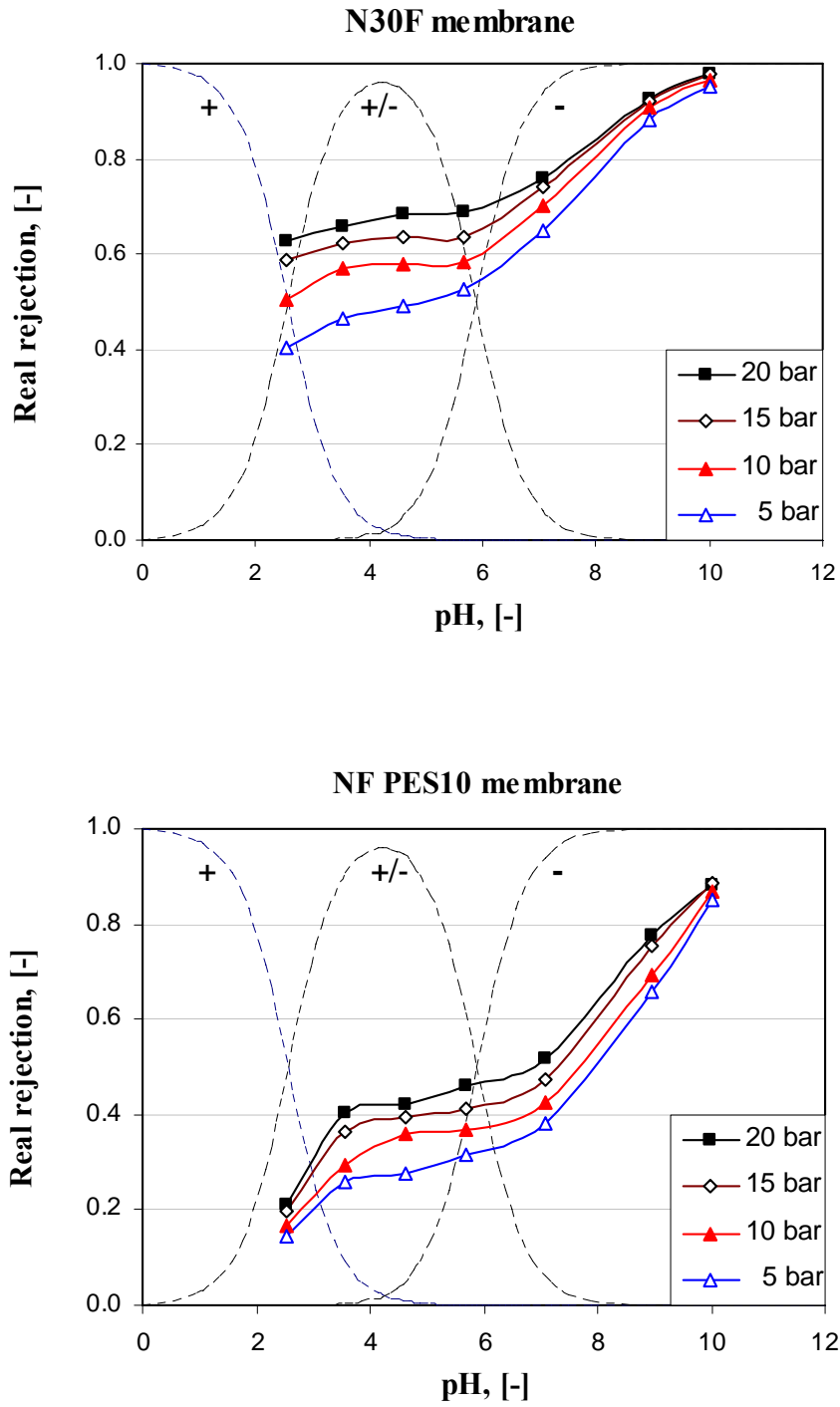
Fig. 3.15 Cephalexin rejection (200 ppm) vs. the solution pH at different pressures

Characterization of Two Commercial Nanofiltration Membrane and
their Application in the Separation of Pharmaceuticals

Chapter III

Although cephalexin has almost the same molecular weight as saccharose, the rejection of cephalexin at the pH around pI, which cephalexin molecules as a whole is zwitterionic without net charge, is much higher than that of saccharose. This may be due to the contribution of different molecular configurations to the solute transport [Kiso et al., 2001]. By taking molecular configuration into account, cephalexin molecule is more like a rod with the length of 1.6 nm away from a sphere while saccharose molecule with 1.2 nm in length and their molecular widths are quite close, which simulated from Cerius2 molecular simulation software shown in Figure 3.16. Therefore, the steric hindrance for cephalexin is much larger than that of saccharose. As a result, at the pH near pI, the steric exclusion plays a main role on the rejection of cephalexin.

Saccharose (MW: 342, 1.2 nm in length)   Cephalexin (MW: 347.4, 1.6 nm in length)
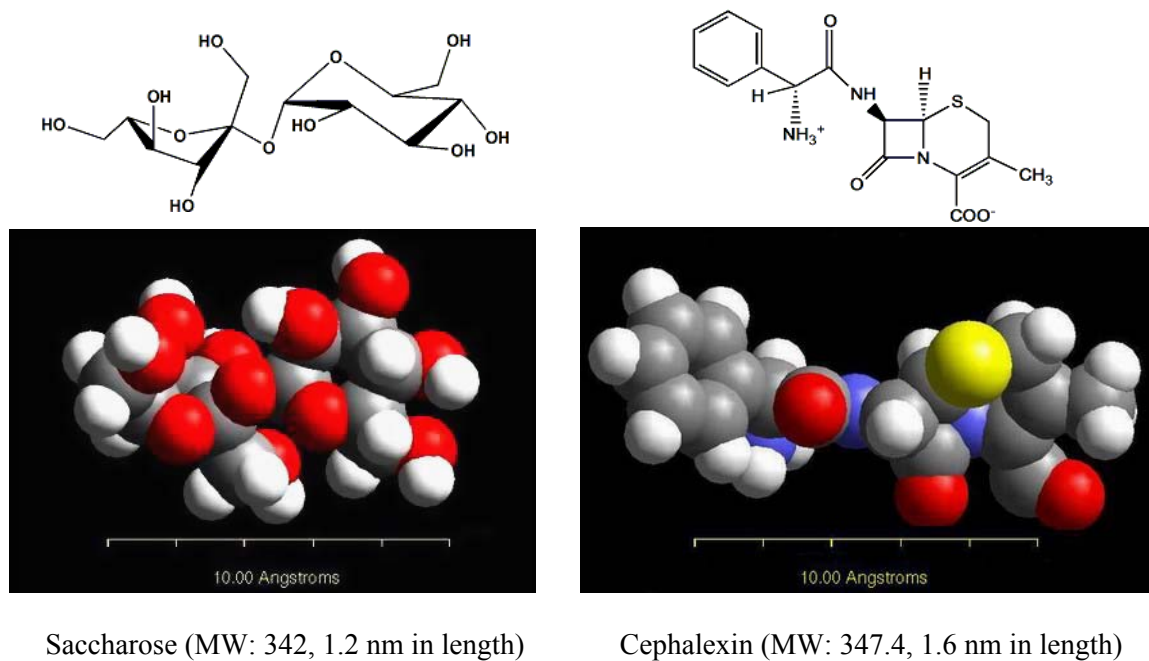
Fig. 3.16 Configuration of molecules simulated from Cerius 2.

3.4.7   Effect of NaCl concentration on the cephalexin separation

From Figure 3.17, the rejection of cephalexin increases with the adding of NaCl into the solution at pH 7.1, and levels off at high NaCl concentrations. This can be explained by the competition of coions passing through the membrane due to the Donnan effect. At pH 7.1, cephalexin molecules are in the state of monovalent anions. Cl^- anions are less rejected by the membrane and Na^+ cations are attracted to penetrate through the membrane, while cephalexin anions are much rejected for their bigger size. However, the rejection of cephalexin levels off along with the increasing NaCl concentration due to the possible screening effect on effective charge density of membrane by higher ion strength.

N30F membrane

Real rejection, [-] vs *NaCl concentration, [mol m^{-3}]*

Legend: 20 bar, 15 bar, 10 bar, 5 bar

NF PES10 membrane
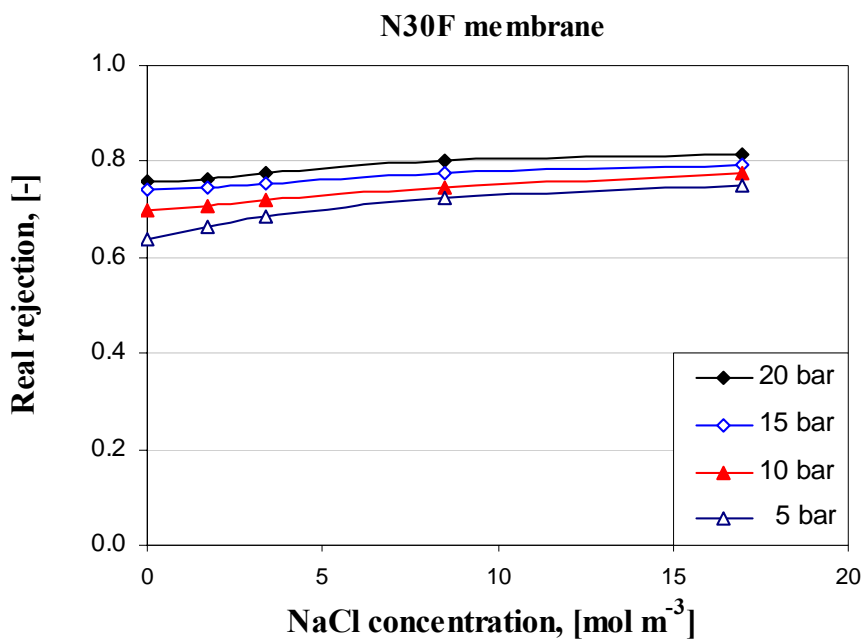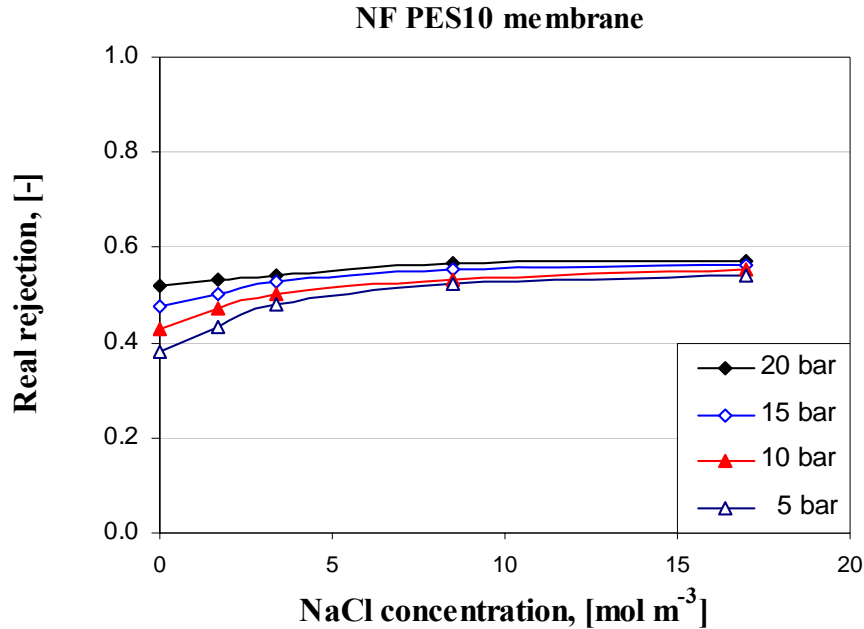
Fig. 3.17 Real rejection of cephalexin (200 ppm) as a function of NaCl concentration at pH = 7.1

3.5. Conclusions

Two negatively charged composite nanofiltration membranes were characterized by estimating their structural parameters (effective pore radius r_p and the ratio of membrane porosity to effective membrane thickness $A_k/\Delta x$) from SHP model. The mean pore size estimated from neutral solute rejection by two different methods were comparable to each other. The effective charge density (ϕX) of membranes was determined by TMS model from the rejection data of NaCl under different molar concentrations, and was related to the salt concentration of bulk solutions. These two NF membranes showed different rejections to various valent anions and cations due to Donnan exclusion in the single electrolyte solutions, i.e. higher rejection to divalent anions and lower rejection to

Characterization of Two Commercial Nanofiltration Membrane and
their Application in the Separation of Pharmaceuticals

Chapter III

divalent cations. While in the binary electrolyte mixture solution of NaCl/Na$_2$SO$_4$, negative rejection of Cl^{-1} by the membranes happened by virtue of the ion competing transport. While in the binary electrolyte mixture solution of NaCl/MgCl$_2$, the cation fractionation factor is very low. To a dipolar molecule, the rejection of cephalexin was investigated in the consecutive lab-scale experiments by adjusting the pH of aqueous solutions to modify the ionization states of cephalexin molecules. The operating pressures and ion strength of solution can also affect the rejection of cephalexin. It is possible to concentrate and purify the cephalexin solution through adjusting operation conditions with these two nanofiltration membranes.

CHAPTER FOUR

CHEMICAL MODIFICATION OF POLYBENZIMIDAZOLE
NANOFILTRATION MEMBRANE FOR THE SEPARATION OF
ELECTROLYTES AND PHAMACEUTICALS

4.1.   Introduction

Desirable nanofiltration membranes for the liquid separation must have the following characteristics: (1) suitable porosity to produce high enough volumetric permeate flux, (2) appropriate pore sizes and a narrow pore size distribution to meet the separation requirements and, (3) essential mechanical strength, chemical resistance and thermal stability to withstand the high pressure, chemical and thermal attack universally existing in the membrane operation.

The formation of a membrane with successful liquid separation performance depends firstly on the selection of suitable membrane material. The materials should have enough chemical, thermal and mechanical stability to withstand the intense separation conditions and the cleaning medium. However, most polymeric membranes proved to have inadequate chemical resistance to survive in harsh environments with different pH ranges and/or long-time resistance for separation problems on an industrial level that requires high thermal and chemical stability [Weber et al., 2003]. Therefore, synthesis or

identification of organic or inorganic materials satisfying these requirements is one of the

focuses in the development of nanofiltration membranes.

Polybenzimidazole is a generic name of a class of heterocyclic polymers, and the most

commonly concerned is the poly-2, 2′-(m-phenylene)-5, 5′-bibenzimidazole (PBI).

Polybenzimidazole is typically synthesized from a condensation reaction of aromatic bis-

o-diamines and dicarboxylates [Powers & Serad, 1986; Chung, 1997f]. The PBI chemical

structure and synthesis scheme is shown in Figure 4.1.

Diphenyl isophthalate (DPIP)   Tetraaminobiphenyl (TAB)

Poly-2, 2′-(m-phenylene)-5, 5′-bibenzimidazole (PBI),   Phenol
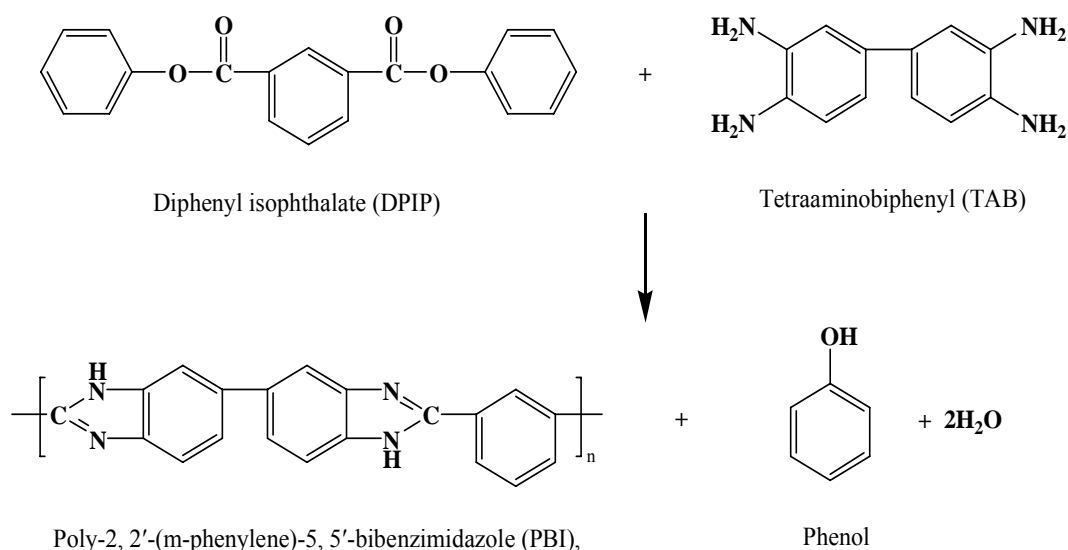
Fig. 4.1 Synthesis schematic of poly-2, 2′-(m-phenylene)-5, 5′-bibenzimidazole (PBI)

The inherent viscosity (IV) of PBI is between 0.7 and 0.75 dL/g, and it has a moisture

affinity (absorbing water up to 13 wt %). PBI was known to possess outstanding thermal,

physical and chemical stability over a wide range of pH [Model et al., 1977; Chung,

1997e], which makes it an ideal candidate material for membranes applied in liquid

separation. Composite PBI membranes have been already developed for reverse osmosis applications in desalting the brackish water, seawater desalination and wastewater recovery [Ram, 1974]. Since all NF membrane have their origins in reverse osmosis (RO) membranes, they are called loose reverse osmosis membranes or tight ultrfiltration membranes with respect to its permeate flux and separation performance [Raman et al., 1994]. It may be possible to applying PBI to fabricate nanofiltration membranes.

In addition of the choice of material, the membrane formation/modification and the membrane morphology/physiochemistry thereof, is also indispensable to achieve expected separations. Most of NF membranes have the molecular size pores on their surface and is negatively or positively charged in order to obtain desirable separation performance. The special chemical property of PBI makes membrane modification extremely attractive. In the basic imidazole group (pKa 7.2) of polybenzimidazole molecule, a heterocycle having two nitrogen atoms, the nitrogen binding with the hydrogen atom is a hydrogen bond donor while the nitrogen with the lone pair is a proton acceptor [Kreuer, 1998]. The further delocalization of proton by the imidazole group due to the adjacent benzene ring gives a charge to polybenzimidazole in the aqueous environment [Saiti et al., 2001]. Therefore, due to its alkaline nature it is possible to modify polybenzimidazole polymer with strong acid to improve its charge property. Staiti et al [2001] prepared sulfonated PBI membranes by sulfuric acid treatment on preformed PBI membranes which having low ion exchange capacity. Moreover, a higher temperature in the range from 450 ºC to 510 ºC was required to convert the ionic bond (SO_4^{2-}) to covalent bond ($-SO_3^-$) for the sulfonic acid treated PBI membranes. In the U.S.

Patent No. 4,634,530 [Kuder et al., 1987], it reported the chemical modification of a preformed PBI semi-permeable membrane (obtained from the solvent evaporation method) through the sulfuric acid treatment. Another method was based on grafting the methyl benzenesulfonate group on polybenzimidazole backbone [Glipa et al., 1997]. However, the −NH− group must be firstly activated by LiH to produce PBI anions before chemical grafting with sodium (4-bromomethyl) benzenesulfonate. Likewise, in the U.S. Patent No. 4,898,917 [Sansone, 1990], the *N*-substituted polybenzimidazole polymers were prepared through reacting with a substituted methyl halide. The polybenzimidazole must be also activated with an alkali hydride in advance.

In this study, the function of –NH- group of the heterocyclic imidazole ring is directly performed. The modified PBI nanoporous membrane exhibits different charged signs from low pH to high pH, subsequently shows high permeate flux and ion rejection properties. For the application, the fabricated PBI membrane will be utilized in the separation of cephalexin. Cephalexin, a semi-synthetic cephalosporin, is therapeutically advantageous and important for its broad antibacterial activity. Cephalexin is a zwitterionic molecule containing amino group and carboxyl group. Similar to amino acids, the ionization states of cephalexin molecules vary with pH in the aqueous solution (in Figure 3.1). The traditional solvent extraction cannot be used to recover it from fermentation broths [Sahoo, et al. 1997]. The modified PBI NF membrane may become a potential tool to separate and purify cephalexin from aqueous solution.

The Chemical Modification of Polybenzimidazole Nanofiltration Membranes
for the Separation of Electrolytes and Pharmaceuticals

Chapter IV

4.2.   Experimental

4.2.1   Chemicals

The polybenzimidazole polymer solution was same as used in Chapter Three. *N, N* -
Dimethylacetimide (DMAc), *p*-Xylylene dichloride (Figure 4.2), heptane, methanol and
ethanol were supplied from Merck, Germany. Uncharged neutral solutes, glycerol,
glucose, saccharose, raffinose and PEG 1000, from Aldrich, USA and several analytical-
grade salts, NaCl, MgCl$_2$, and Na$_2$SO$_4$, from Merck, Germany, were used to characterize
membrane structure parameters. Molecular weight, diffusivities and Stokes radii of these
solutes are shown in Tables 3.1. NaOH (1.0 N) and HCl (1.0 N) solutions were used to
modify the pH of feed solutions.

$$ClH_2C \longrightarrow \bigcirc \longrightarrow CH_2Cl$$
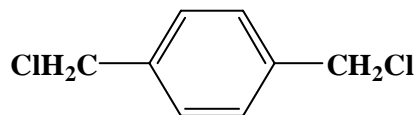
Fig. 4.2. Chemical structure of *p*-Xylylene dichloride

4.2.2   Fabrication of composite PBI nanofiltration membranes

The polar aprotic solvent, *N, N*-dimethylacetamide (DMAc), was utilized to form the
polybenzimidazole polymer solution. A preferred casting solution for fabricating
nanofiltration membrane comprises about 15 to 25 percent by weight polybenzimidazole
polymer through diluting the supplied PBI solution with DMAc. In this study, PBI casting
solution, PBI/DMAc/LiCl (21.6/76.7/1.7 wt %), was prepared by diluting the supplied
PBI solution with DMAc. The PBI solution can be firstly cast on the polyester non-woven

The Chemical Modification of Polybenzimidazole Nanofiltration Membranes
for the Separation of Electrolytes and Pharmaceuticals

Chapter IV

fabric by a casting knife with the slit of 150 μm, then dipped into tap water so that the phase inversion took place. The as-cast PBI membrane was dipped in fresh methanol for three times to replace water. Then, the membrane was soaked in the solution of substituting agent *p*-Xylylene dichloride (1.0 wt%) in heptane from 30 min to 24 hours. After taking out of *p*-Xylylene dichloride solution, the modified PBI membrane was surface-blotted and rinsed by methanol again, and then kept in water for testing. Morphology study of PBI nanofiltration membrane was performed by using by scanning electron microscopy (SEM or FESEM).

From experiment, it was found that *p*-Xylylene dichloride cannot be dissolved and hydrolyzed in water under room temperature. However, Cl⁻ anions can be detected in the *p*-Xylylene dichloride/heptane solution after putting the as-cast PBI membrane into the solution. Another phenomenon also verified the crosslinking reaction. When the modified asymmetric PBI membrane was dissolved in DMAc at ambient temperature for long time (around 30 days), a little amount of undissolved gel was left in the solution, while the as-cast PBI membrane can be totally dissolved. The possible PBI modification scheme is illustrated in Figure 4.3.

4.2.3 FTIR analysis

Figure 4.4 shows the ATR-FTIR spectra of the as-cast PBI and *p*-xylylene dichloride modified PBI membrane. According to the previous FTIR study on PBI and its derivatives [Musto et al., 1989], the strong absorption band from 2500 to 3600 cm^{-1} in the

Polybenzimidazole   *p*-Xylylene dichloride
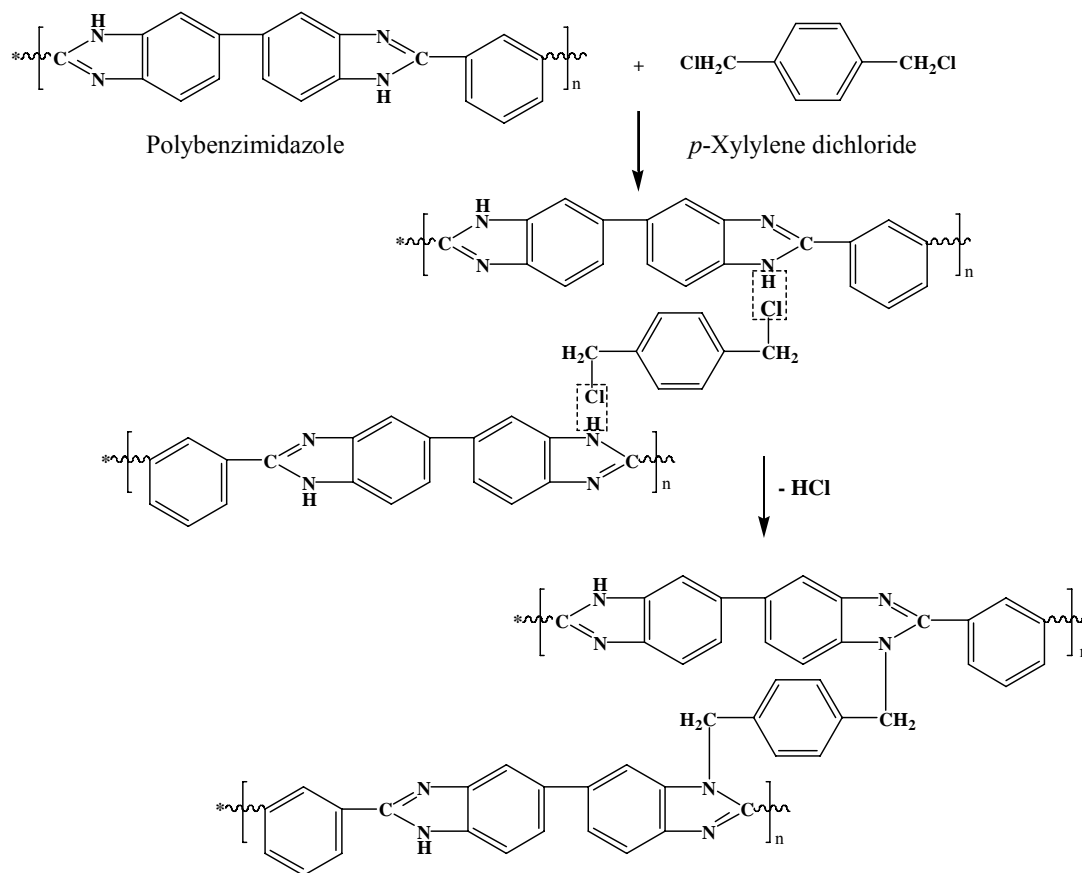
Fig. 4.3. Possible mechanism of polybenzimidazole modification by *p*-Xylylene dichloride

as-cast PBI is assigned to N-H groups of imidazole ring. In this band, the sharp peak centered at 3420 cm^{-1} may be attributed to the stretching vibration of the isolated non-hydrogen bonded N-H group, while the broad peak with the highest absorption intensity around 3080 cm^{-1} corresponds to the stretching vibration of the N-H groups involved inhydrogen bonding. After *p*-xylylene dichloride modification, the broad peak which representing hydrogen bonded N-H group moves towards bigger wave numbers and the highest absorption intensity takes place around 3200 cm^{-1}. This indicates that the hydrogen bonding between N-H groups becomes weak after *p*-xylylene dichloride

modification. Many hydrogen bonded N-H groups turn into non-hydrogen bonded due to partial *N*-substitution, as illustrated in Figure 4.3. At the same time, the p-xylylene dichloride modified PBI exhibits a new small shoulder peak located around 2920 cm^{-1}. This peak may be attributed to the C-H stretching vibrations, indicating the presence of *p*-xylylene units in the newly modified PBI structure.
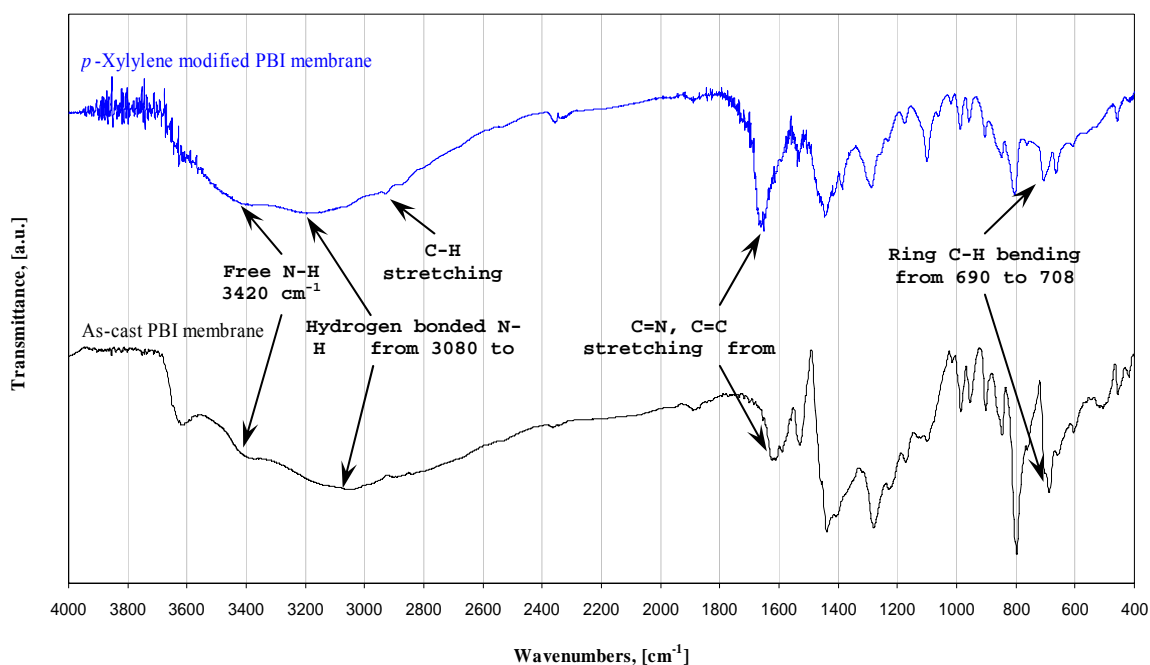
Fig. 4.4 Comparison of FTIR spectra between as-cast and modified PBI membranes

There are two additionally notable shifts. The band at 1620 cm^{-1} originally corresponding to C=N and C=C stretching vibrations in the five-member heterocyclic ring of PBI shifts to 1670 cm^{-1} after the *p*-xylylene dichloride modification. This red shift could be explained by the electronic effects of N-substitution of methylene. The N-substitution also affects the out-of-plane bending of C-H groups in the five-member heterocyclic ring. As a consequence, the absorption peak of C-H groups shifts from 690 cm^{-1} to 708 cm^{-1}.

4.2.4   XPS analysis

Elemental analysis verification by using XPS was also performed. An X-ray photoelectron spectrometer (Kratos XPS system-AXIS His-165 Ultra, England) was used to measure the surface elements of the polymer films through using the monochromatized al Kα X-ray source (1486.6 eV photos) at a constant dwell time of 100 ms and a pass energy of 40 eV. The anode voltage and anode current were 15 kV and 10 mA, respectively. The pressure in the analysis chamber was maintained at 5.0×10^{-8} Torr or lower during each measurement. All core-level spectra were obtained at a photoelectron takeoff angle of 90˚ with respect to the sample surface, and the X-ray penetration depth is about 7.5 nm for polymer materials. XPS did not detect the element of Cl in both the as-cast and modified asymmetric PBI membranes. The element concentrations analyzed from XPS are listed in Table 4.1. The C/N atomic ratio of PBI membrane had a large increase after modified by *p*-Xylylene dichloride.

Table 4.1 Atomic concentration of elements analyzed from XPS

Membrane	C	N	Cl
As-cast PBI membrane	83.97	16.03	No detect
Modified PBI membrane	91.56	8.44	No detect

4.3.   Result and discussion

4.3.1   Morphology study of PBI membrane by scanning electron microscope (SEM)

The Chemical Modification of Polybenzimidazole Nanofiltration Membranes
for the Separation of Electrolytes and Pharmaceuticals

Chapter IV

From the morphology of the as-cast PBI membranes (Figure 4.5), it can be seen that the composite PBI membrane is full of finger-like macrovoids. Near the selective surface, there is a sponge-like layer about 1.5 μm in thickness. Even at a magnification of 50, 000, no visible pores can be observed on the membrane surface. After modification, no significant morphology differences can be observed from SEM images.

As-cast composite PBI membrane

Modified composite PBI membrane
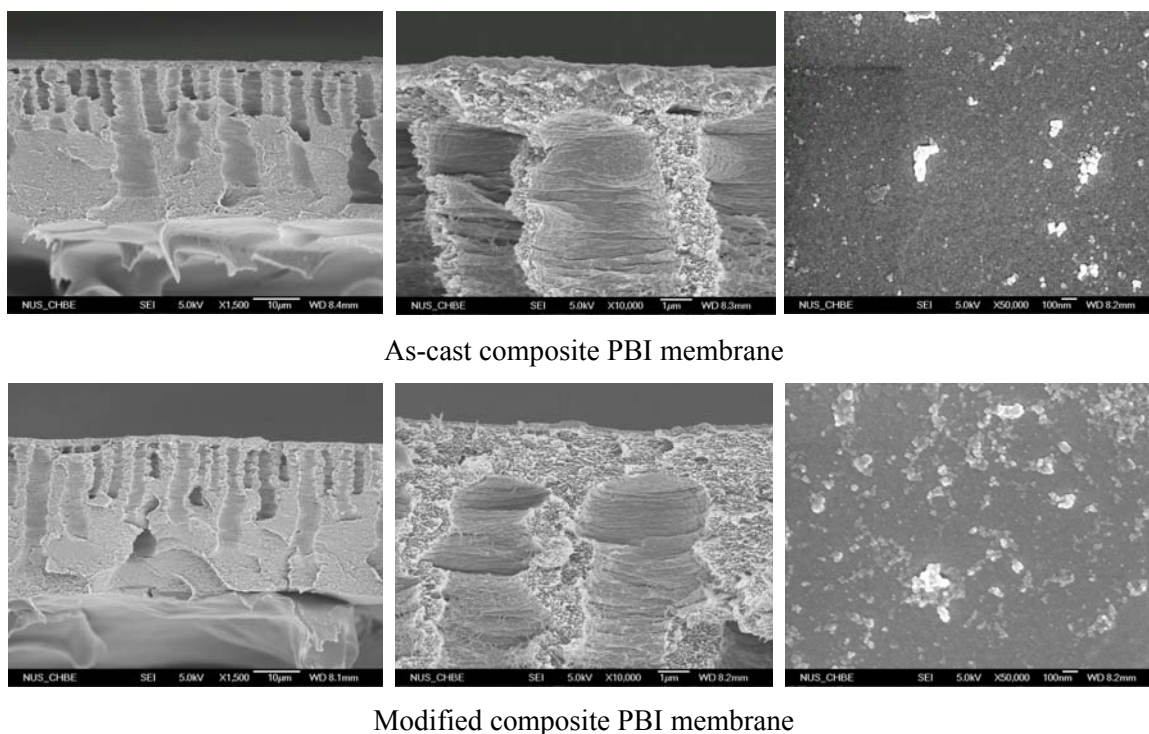
Fig. 4.5. Scanning electron micrographs of an as-cast and the *p*-Xylylene dichloride modified composite polybenzimidazole membranes (left) whole cross-section (×1,500, scale bar 10 μm), (middle) partial cross-section (×10,000, scale bar 1 μm), (right) the selective layer surface (×50,000, scale bar 100 nm).

4.3.2 Permeate flux, mean effective pore size, pore size distribution

The pure water permeability (PWP) of the as-cast asymmetric PBI membrane was 3.58 liter m^{-2} bar^{-1} hr^{-1}. Figure 4.6 depicts the pure water permeability of the modified

polybenzimidazole membrane as a function of modifying period in the *p*-Xylylene dichloride/heptane solution. Further increase in the dipping time in the solution of *p*-Xylylene dichloride after 8 hours leads the pure water permeability level off. It is possible to assume that the modification only happens on the surface of PBI membrane and pore surface inside membrane. After being dipped in the *p*-Xylylene dichloride (1.0 wt%)/heptane solution for 12 hours, the pure water permeability (PWP) of the modified asymmetric PBI membrane (used for further characterization and application) decreased to 2.25 liter m^{-2} bar^{-1} hr^{-1}.

PBI membrane modified by *p* -Xylylene dichloride
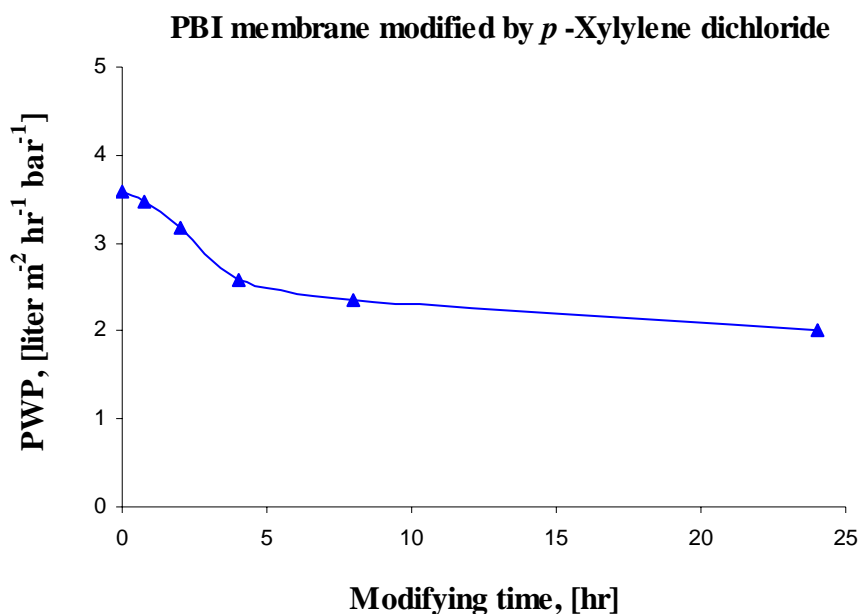
Fig. 4.6. Pure water permeability of the modified polybenzimidazole membrane as a function of modifying period in the *p*-Xylylene dichloride/heptane solution

It is found that the solute rejection for both biological and synthetic membranes can be expressed by a log normal probability function of solute size, as described in the following equation [Michaels, 1980]:

The Chemical Modification of Polybenzimidazole Nanofiltration Membranes
for the Separation of Electrolytes and Pharmaceuticals

Chapter IV

$$R_T = erf(y) = \frac{1}{\sqrt{2\pi}} \int_{-\infty}^{y} e^{-\frac{u^2}{2}} \, du, \quad where \quad y = \frac{\ln r_s - \ln \mu_s}{\ln \sigma_g} \tag{4-3}$$

where R_T is the solute rejection, r_s is the solute radius, μ_s is the geometric mean radius of solute at $R_T = 50\%$, σ_g is the geometric standard deviation about μ_s, defined as the ratio of r_s at $R_T = 84.13\%$ and $R_T = 50\%$. When the solute rejection of a membrane is plotted vs. solute radius on a log-normal probability paper, a straight line is obtained as:

$$F(R_T) = A + B(\ln r_s) \tag{4-4}$$

The values of μ_s and σ_g determine the position and sharpness of the rejection curves, respectively.

From the characterization method described in Chapter III, the mean effective pore size of the as-cast PBI membrane through the solute transport method was 1.68 nm in radius and the molecular weight cut-off is 4,032 Da at the pressure of 15 bar from Figure 4.7. The mean effective pore size of the modified PBI membrane was 0.36 nm in radius and the molecular cut off (MWCO) is 444 Da listed in Table 4.2.

Table 4.2 Pure water permeability (PWP), mean effective pore size (r_p), geometric standard deviation (σ_p) and the molecular weight cut off (MWCO) of PBI membranes from Fig. 4.7

Membrane	PWP (l m^{-2} bar^{-1} hr^{-1})	r_p (nm)	σ_p (-)	MWCO (Da)
As-cast PBI membrane	3.58	1.68	1.57	4,032
Modified PBI membrane	2.25	0.36	1.38	444

The cumulative pore size distribution curves and the probability density function curves of the PBI membranes at the pressure of 15 bar are presented on Figures 4.8 & 4.9. From Figure 4.9, it can be seen that after the modification, the pore size distribution becomes very narrow and forms a sharp peak. Thus, the membrane structure and subsequent separation performance can be effectively controlled through chemically modification on the membrane surface.
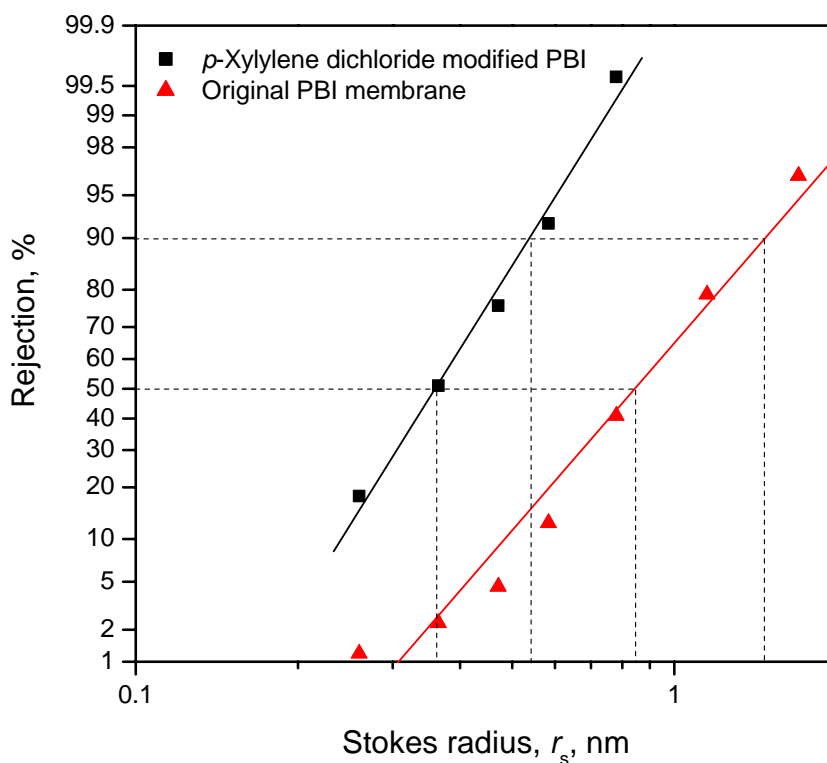
Fig. 4.7. Effective rejection curves (solute rejection versus Stokes radii) plotted on the log-normal probability coordinate system under the pressure of 15 bar
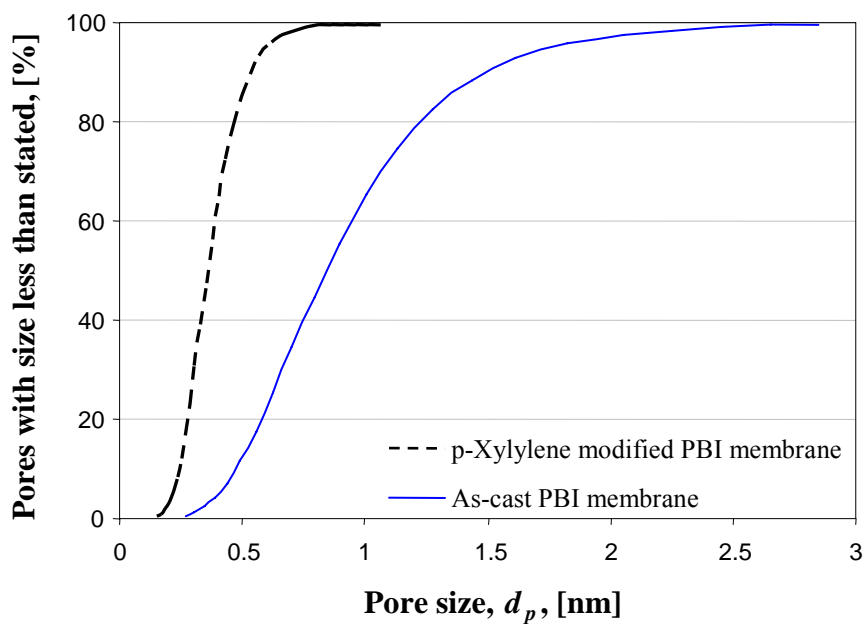
Fig. 4.8. Cumulative pore size distribution curves of PBI membranes at the pressure of 15 bar
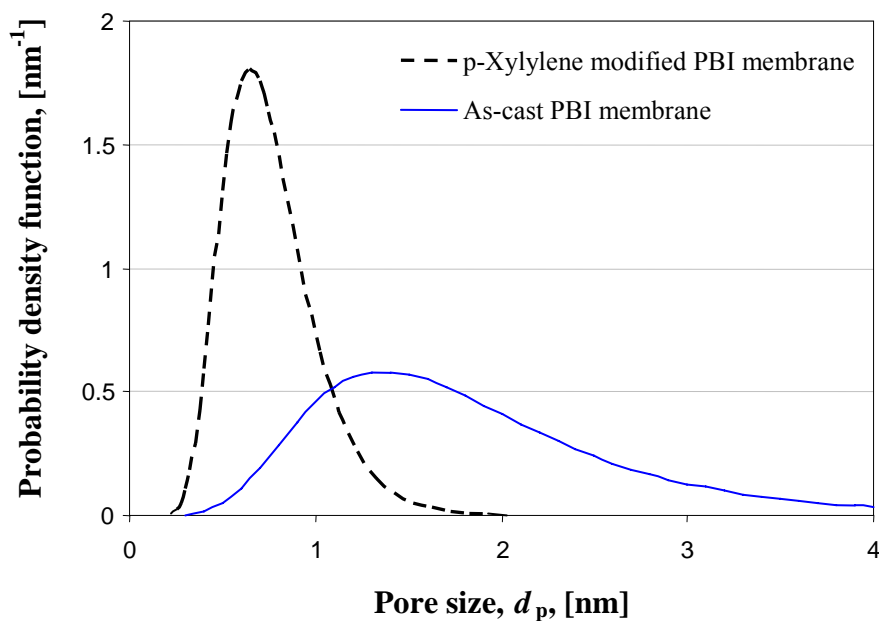
Fig. 4.9 Probability density function curves of PBI membranes at the pressure of 15 bar

4.3.3   Membrane characterization using single electrolyte solution

The rejection performance of different single salts, i.e. NaCl, $MgCl_2$ and Na_2SO_4, in the aqueous solution by the PBI membranes showed in Figure 4.10. The *p*-Xylylene modified PBI membrane presented a much higher rejection to the di-valence cation (Mg^{2+}), but a lower rejection to the di-valence anion (SO_4^{2-}) and the lowest rejection to the mono-valence ions (Na^+ and Cl^-), in the order of R ($MgCl_2$) > R (Na_2SO_4) > R (NaCl), which are similar to the trend of the as-cast PBI membrane. In addition, the solute rejection increased with increasing pressures. This is because the water permeate flux through the membrane is linearly related to the pressure difference applied, whereas the solute flux is both dependent on the concentration difference over the membrane and on the water flux. When increasing the trans-membrane pressure difference, the water flux increases relatively more than the solute permeate. This causes a decreasing permeate concentration and an increasing rejection [Garcia-Aleman & Dickson, 2004].
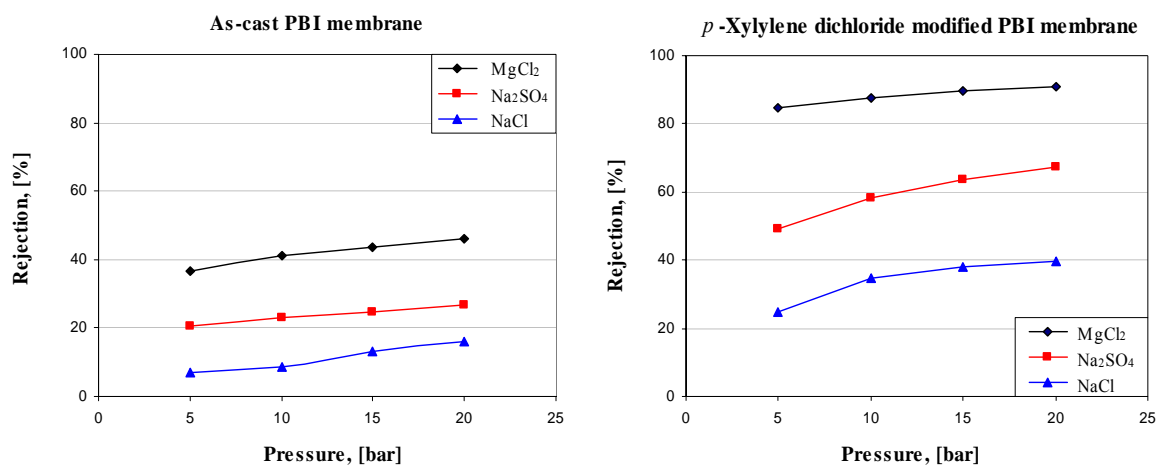
Fig. 4.10. The salt rejection by PBI nanofiltration membrane at different applied pressures
(The bulk single salt concentration: 3.4 mol m^{-3}, pH 7.0).

4.3.4   Ion rejection of NF membrane in electrolyte mixture solutions

In the NaCl/Na$_2$SO$_4$ binary salt mixture solution with an anion molar concentration ratio Cl$^-$/SO$_4^{2-}$ of 1.0, Cl$^-$ ions are forced to permeate preferentially compared to SO$_4^{2-}$ ions since Cl$^-$ has a lower valence, as shown in Figure 4.11. Na$^+$ ions also permeate membrane together with Cl$^-$ to maintain electroneutrality at both sides of the membrane in accordance with the Donnan principle. Moreover, the negative rejection of chloride ions was observed at a low applied pressure. Along with the increasing pressure, the rejection of Cl$^-$ increases because the increased permeate flux in the pore plays an important role. The SO$_4^{2-}$ and Cl$^-$ anions could be fractionated by the charged PBI NF membranes.
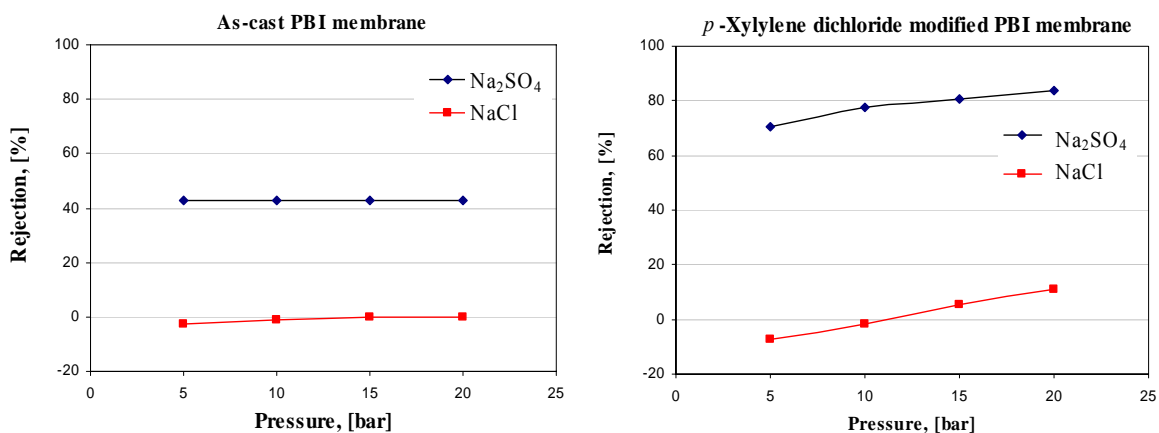
Fig. 4.11. Ion rejection in the mixture of NaCl/Na$_2$SO$_4$ solution as a function of applied pressure
([NaCl] = 3.4 mol m^{-3}, [Na$_2$SO$_4$] = 3.4 mol m^{-3}, pH 7.0)

While in the MgCl$_2$/NaCl binary salt mixture solution with a molar concentration ratio Mg^{2+}/Na$^+$ of 1.0, Na$^+$ ions are forced to permeate preferentially compared to Mg^{2+} ions since Na$^+$ has a lower valence, as shown in Figure 4.12. As a result, Mg^{2+} and Na$^+$

cations can be fractionated by the modified PBI nanofiltration membranes.
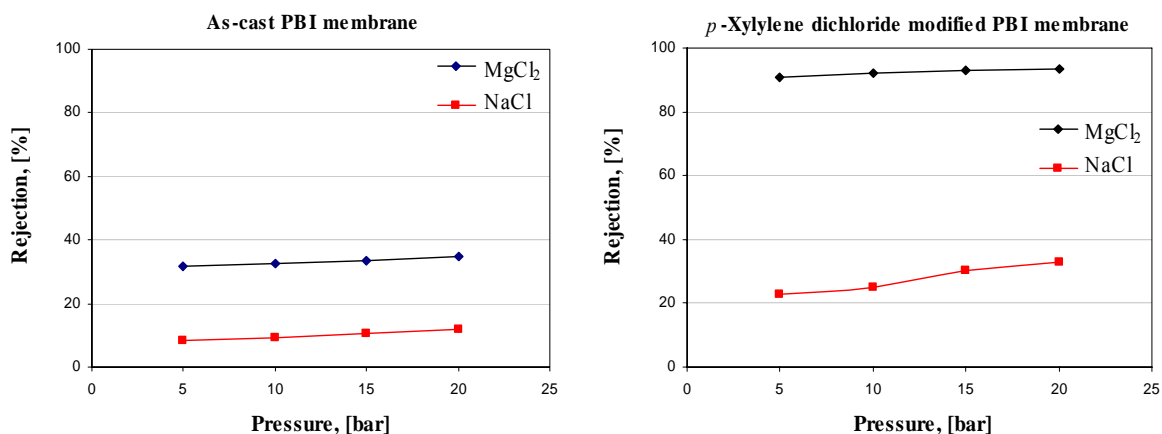
Fig. 4.12. Ion rejection in the mixture of NaCl/MgCl$_2$ solution as a function of applied pressure
([NaCl] = 3.4 mol m^{-3}, [Na$_2$SO$_4$] = 3.4 mol m^{-3}, pH 7.0)

4.3.5   Effect of solution pH on the NaCl rejection

In order to investigate the charge property of the PBI membrane at different pH, the retention experiments of Cl$^-$ and Na$^+$ in the NaCl solution were performed through adjusting the pH of solution with the addition of 1.0 N NaOH or HCl solution. Figure 4.13 indicates that the membrane showed a V-shaped trend of rejection to Cl$^-$ and Na$^+$ ions, which are quite similar to the performance of ceramic membranes [Weber et al., 2003]. It seems that the PBI membranes have an isoelectric point near 7.0, and may be positively charged at lower pH, negatively charged at higher pH. This is attributed to the chemical structure of PBI which can delocalize the proton on the other ring atoms.

p-Xylylene dichloride modified PBI membrane
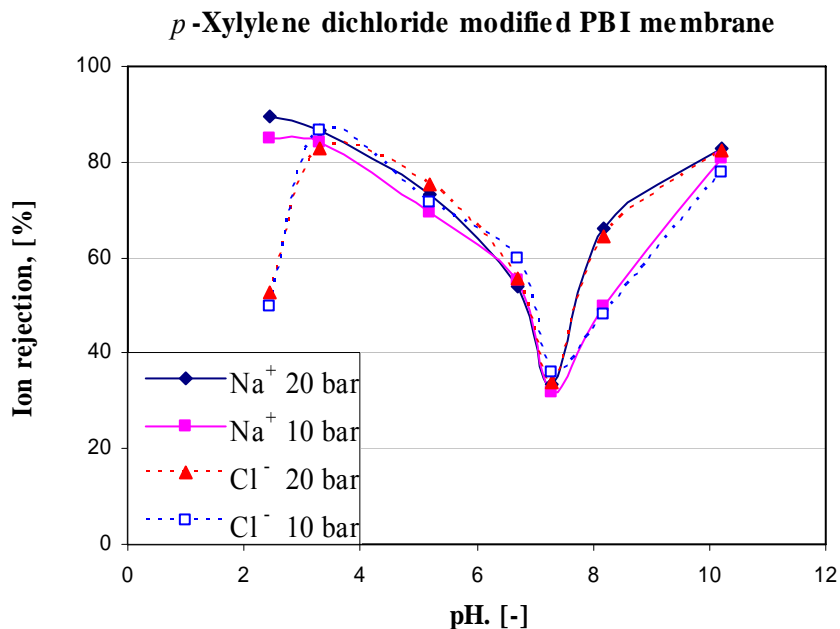
Fig. 4.13. Rejection of NaCl (3.4 mol m⁻³, 20°C) as a function of solution pH
(Solution pH was adjusted by adding 1.0 N HCl or 1.0 N NaOH)

4.3.6   Cephalexin separation performance of PBI NF membranes

As an amphoteric electrolyte molecule in the aqueous solution, cephalexin acts as both basic (proton acceptor) and acid (proton donor) since cephalexin molecules have the amino group (-NH$_2$) and the carboxyl group (-COOH). Depending on the pH of solution, cephalexin can be positively charged (acid) at pH < pI (Isoelectric point, around 4.5 ~ 5.0), negatively charged (basic) at pH > pI and net neutral (dipolarions) at pH = pI. In the dipolar form, the amino group is pronated (-NH$_3^+$) and the carboxyl group is dissociated (-COO⁻). Based on their dissociation constants (pK_as), the fraction of different ionization states of cephalexin at different pH can be expressed by the Henderson-Hasselbalch equation [Stryer, 1995] plotted on Figure 4.14 (the blue curves):

$$pH = pK_a + \log(\frac{[\text{proton\ acceptor}]}{[\text{proton\ donor}]}) \qquad (4\text{-}6)$$

As shown in Figure 4.14, the rejection of cephalexin increases with the growth of pH at different pressures for the as-cast and *p*-Xylylene dichloride modified PBI membranes. For the *p*-Xylylene modified PBI membranes with a small mean pore size, it shows higher rejection than the as-cast PBI membrane.
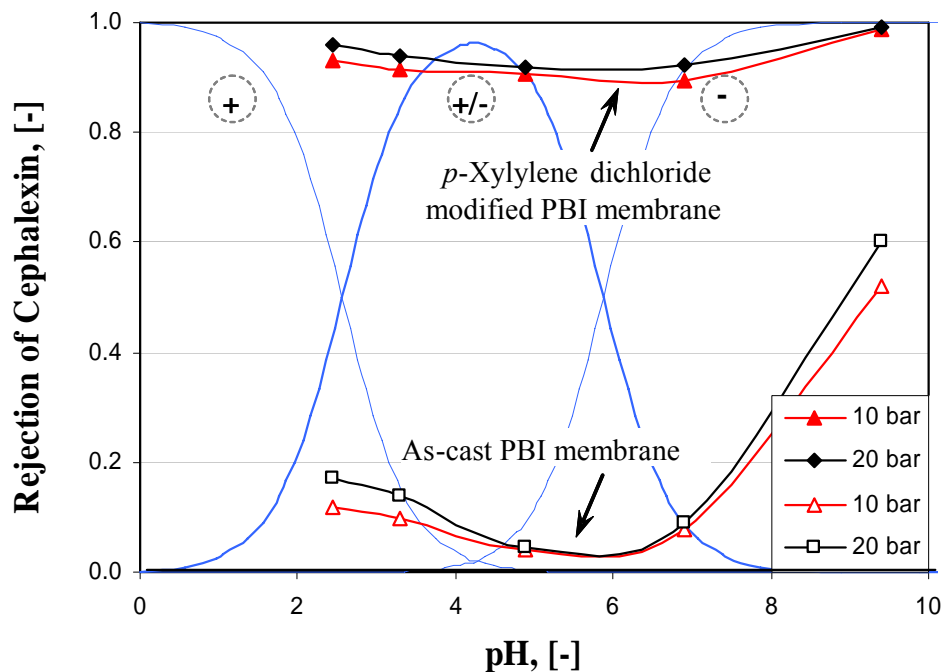
Fig. 4.14. Cephalexin rejection (200 ppm, 18ºC) vs. the solution pH at different pressures.

After pH is above 6.0, the as-cast PBI membrane expressed a sharp increasing rejection and cephalexin was 78 % rejected (15 bar) at pH 9.5. While the *p*-Xylylene modified PBI

The Chemical Modification of Polybenzimidazole Nanofiltration Membranes
for the Separation of Electrolytes and Pharmaceuticals

Chapter IV

membrane showed much higher rejection over the whole range of pH 2 to pH 10. This shows that cephalexin rejection is dependent on the pore size (steric exclusion) and electrostatic interaction between solutes and membrane. The pH of the solution has the dominant effect on separation because pH determines the ionization states of cephalexin and the surface charge density of the PBI membranes.

4.4. Conclusions

The chemically modified PBI composite flat sheet nanofiltration membrane can be fabricated through the controlled chemical modification by the *p*-Xylylene dichloride. The pure water permeability of the modified PBI membrane can be controlled through adjusting the treatment period in the *p*-Xylylene dichloride solution. Characterized by the solute transport method, the modified PBI membrane has a decreased pore size of 0.36nm in radius and the narrowed pore size distribution as compared to the as-cast PBI membrane. The resultant composite PBI nanofiltration membranes showed higher rejection to di-valence cations and anions, which can be applied to fractionate $NaCl/Na_2SO_4$ and $NaCl/MgCl_2$ binary salt mixtures. The separation performance of the PBI NF membrane depends on the pH value of the contacted solutions. The membranes showed a V-shaped trend of rejection to Cl^- and Na^+ ions along with the increase in pH, which is similar to ceramic membranes and can be applied to separate and purify cephalexin, amino acid and other pharmaceuticals from their aqueous solutions.

CHAPTER FIVE

FABRICATION OF ASSYMETRIC PBI NANOFILTRATION HOLLOW FIBER MEMBRANES APPLIED IN CEPHALEXIN SEPARATION AND CHROMATE REMOVAL

5.1   Introduction

Since Mahon [1966] proposed using hollow fiber membranes as separation apparatus in his patents four decades ago, synthetic polymeric hollow fiber membrane has advanced as a key player in separation technologies. Compared to the flat sheet membrane, hollow fiber configuration has the following advantages: 1) a much larger membrane area per unit volume of membrane module, and hence a higher productivity, 2) self mechanical support which can be back flushed for liquid separation, and 3) good flexibility and easy handling during module fabrication and system operation. Nowadays, hollow fibers are widely used in gas separation, reverse osmosis, ultrafiltration, pervaporation, dialysis and supported liquid membrane extraction [Yang & Cussler, 2000; Strathmann, 2001].

Nanofiltration has attracted increasing attention on the wastewater treatment and pharmaceutical syntheses in recent years. However, most available nanofiltration modules are still made in flat sheet, spiral-wound and tubular configurations, which may restrict its application. In addition, most NF membranes are composite membranes via

sophisticated fabrication processes. Some of them are fabricated by coating an ultrathin porous barrier layer on a microporous support, while others are through the interfacial polymerization by simultaneously cross-linking a nascent film at the interface or through chemical modification of surface with the aid of sulfonation or carboxylation [Peterson, 1993]. There is an urgent need to develop simple and direct spinning technologies to fabricate NF composite membranes in one step. However, most polymeric membranes often proved inadequate chemical resistance to survive in harsh environments with different pH ranges [Weber et al., 2003]. Polybenzimidazole (PBI) was known to possess outstanding thermal, physical and chemical stability over a wide range of pH [Chung, 1997e]. Based on this deficiency, one of the objectives of this chapter is to fabricate NF hollow fiber membranes.

Compared to reverse osmosis, nanofiltration can be operated under low pressure and high permeate flux to remove multivalent ions, such as SO_4^{2-}, AsO_4^{2-}, Cd^{2+}, CrO_4^{2-} and so on. Although Cr(III) is an essential element for living beings, playing an important role in the carbohydrate metabolism, as a species of hexavalent chromium, chromate Cr(VI) has been proved that it can induce coetaneous allergy and becomes carcinogenic after long exposures [Loyaux-Lawniczak et al., 2001]. Hexavalent chromium exists in industry effluents when producing chromate salts by the soda-ash roasting of chromite ores with sodium carbonate, and in other applications, such as metal pickling and plating operations, anodizing aluminum, chromium alloy, leather tanning, timber preservative ($CuO·CrO_3·As_2O_5$) and in the manufacture of paints (Cr_2O_3), pigments ($ZnCrO_4$ or $PbCrO_4$), electroplating (CrO_3) and wood preservatives [Jacobs and Testa, 2005].

Chromates have also been used extensively as metal corrosion inhibitors in open and closed cooling water systems. As a result, chromate has become one of the most serious groundwater contaminants especially at industrial producing sites and military facilities due to its widespread applications [Nriagu and Nieboer, 1988]. It is well known that CrVI species are highly toxic to biological systems for their high mobility across biological cell membrane and strong oxidizing potential [Visvanathan, 1989]. Due to the high toxicity of chromate which seriously pollutes underground water systems, the tolerated concentration was strictly controlled by environment norms. However, the chromium concentration in industrial discharges can often reach much more than 500 μg L^{-1} even though the limit by World Health Organization is only 50 μg L^{-1} [Katz and Salem, 1994]. Strict regulations are enforced worldwide to prevent illegal discharging of this highly toxic carcinogenic waste.

Generally, the Cr(VI) contained wastewater is of much high total alkalinity. The traditional approach for treatment of chromate is the chemical reduction of hexavalent to trivalent Cr(III) under low pH, followed by precipitation or coprecipitation as chromic hydroxide of Cr(OH)$_3$ from the solution [Kimbrough et al. 1999]. As a result, a large amount of chemicals are required while a large quantity of sludge is produced. Some approaches have been proposed to remove CrVI from aqueous solutions, such as ion-exchange [SenGupta et al. 1988; Zhao et al., 1998; Petruzzelli, 1995], adsorption [Gupta and Sharma, 1994; O'Dwyer and Hodnett, 1995; Ghiaci et al., 2004], solvent extraction [Ohashi et al., 1984; Noro et al., 2001], and membrane-based separation [Kishore et al., 2003; Baek and Yang 2004; Scindia et al., 2004]. Based on the interaction between

chromate anions and charged membranes, nanofiltration may likely become a tool to separate chromate from basic aqueous solution [Hafiane et al., 2000].

In our previous work in Chapter 4, polybenzimidazole (PBI) has been investigated and identified as an ideal material for nanofiltration. However, to our best knowledge, PBI NF hollow fibers have never been reported. Therefore, this work will investigate the formation of NF hollow fibers using PBI. At the same time, effects of bore fluid composition and the spinning conditions on the morphology and separation performance of the resultant PBI hollow fiber membranes and the charge characteristics of PBI NF hollow fibers and their ion separation performance will be explored. The separation and concentration of cephalexin, and elimination of trace chromate from water will be employed to evaluate the efficiency of the fabricated PBI NF hollow fiber membranes.

5.2. Experimental

5.2.1 Chemicals

The PBI polymer dope solution was purchased from Hoechst Celanese Corporation, Somerville, N. J., which has the composition of PBI 25.6 wt%, DMAc 72.4 wt%, LiCl 2.0 wt%. *N*, *N* - Dimethylacetimide (DMAc), ethylene glycol and dodecane were purchased from Merck, Germany. Uncharged neutral solutes, glycerol, glucose, saccharose, raffinose and PEG 1000, from Aldrich, USA and several analytical-grade salts, NaCl, $MgCl_2$, $MgSO_4$, Na_2SO_4 and $K_2Cr_2O_7$, from Merck, Germany, were used to characterize membrane structure parameters. Molecular weight, diffusivities and Stokes

radii of neutral solutes used for pore size characterization are shown in Tables 3-1 [Bowen et al., 1997].

5.2.2   Fabrication of PBI nanofiltration hollow fiber membranes

The polymer solution of PBI/DMAc/LiCl (21.6/76.7/1.7 wt%) was prepared by diluting the supplied PBI solution with DMAc. The viscosity of the PBI dope solution was 47.4 Pa s (at shear rate of 10 s^{-1}) measured by an ARES Rheometric Scientific Rheometer. Different bore fluid solutions were adopted, such as dodecane, DMAc and water mixture, DMAc and ethylene glycol mixtures. Table 5.1 lists the detailed spinning parameters. The schematic diagram of the hollow fiber spinning spinneret is illustrated in Figure 5.1. The as-spun hollow fibers were immersed in water for 3~5 days to remove the residual DMAc or/and ethylene glycol. Then, the hollow fibers were post-treated by dipping in a 50 wt% glycerol aqueous solution for 48 hr and dried in air at room temperature used for making hollow fiber modules for separation experiments.

Extraneous elongational stretching on the spinning line was performed during dry-jet wet spinning in Batch IV. The elongational draw ratio, φ, is defined as the ratio of the cross-section area of dope flowing channel in the spinneret to the solid cross-section area of the precipitated hollow fiber membrane as follows,

$$\varphi = \frac{(OD^2 - ID^2)_{spinneret}}{(OD^2 - ID^2)_{hollow\ fiber}} \tag{5-1}$$

Elongational draw ratio is a function of the take-up speed during spinning where

extraneous stretching may take place and reduce hollow fiber dimension. The effect of elongational ratio on the permeate flux and pore size on the selective outer layer will be discussed later.
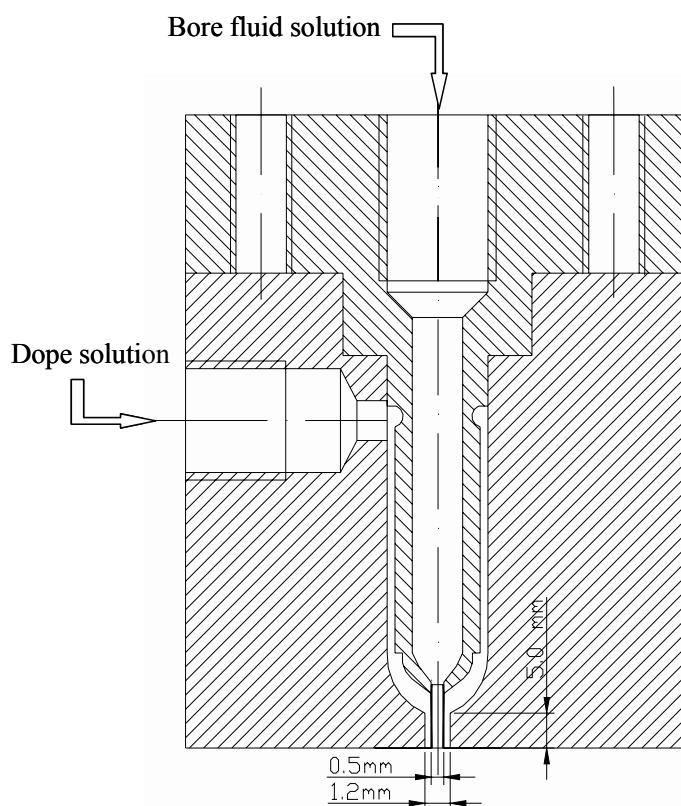
Fig. 5.1. Schematic diagram of spinneret for hollow fiber spinning

5.2.3   Chemical analysis

The concentration of Cr^{6+} was analyzed through a redox titration method with ammonium ferrous sulfate as the reduction agent and *N*-phenylanthranilic acid as the indicator [Wang and Li, 2004].

Table 5.1 Spinning conditions* of PBI NF hollow fiber membranes from PBI dope solution
(PBI 21.6 wt %, DMAc 76.7 wt %, LiCl 1.7 wt %)

		Batch I	[R]Batch II	Batch III	Batch IV	Batch V
Dope flow rate	(ml/min)	1.2 (A), 2.4 (B), 3.6 (C), 3.6 (D)	1.2 (A), 2.4 (B), 3.6 (C), 3.6 (D)	1.0 (A), 2.0 (B), 4.0 (C), 8.0 (D)	2.0 (A), 4.0 (B), 4.0 (C), 4.0 (D), 4.0 (E)	1.0 (A), 4.0 (B), 4.0 (C),
Bore fluid composition		DMAc 86 wt%, H_2O 14 wt%	Dodecane	Ethylene glycol 80 wt%, DMAc 20 wt%	Ethylene glycol 50 wt%, DMAc 50 wt%	Ethylene glycol 23.3 wt%, DMAc 76.7 wt%
Bore fluid flow rate	(ml/min)	0.75, 1.5, 2.25, 2.25	0.36, 0.72, 1.08, 1.08	0.25, 0.5, 1.0, 2.0	0.5, 1.0, 1.0, 1.0, 1.0	0.25, 1.0, 1.0
Ratio of dope/bore fluid rate (-)		1.6	3.33	4.0	4.0	4.0
Air gap	(mm)	10	10	10	16	20
Take-up speed	(m/min)	5.2, 10.7, 10.7, 21.8	3.2, 4.0, 4.9, 20.9	1.8, 4.0, 8.5, 17.4	5.7, 12.2, 18.5, 25.3, 38.4	6.0, 12.9, 26.2

* Coagulant bath: tap water, 26 ºC; Dope temperature: 26 ºC; Bore fluid temperature: 26 ºC; Relative humidity: 60 ~ 70 %.

[R] Refer to the reference [Model, 1977].

* Letters in parentheses correspond to the sample number in Figures 5.2 – 5.7.

* Air gap: the distance between the spinneret outlet and the top surface of the coagulation bath.

* Take-up speed: the speed of collecting hollow fibers.

5.2.4   Nanofiltration experiments with PBI nanofiltration hollow fiber membranes

Nanofiltration experiments were conducted in a lab-scale circulating filtration unit, described in previous chapters. Two testing modules with filtration area about 100 cm^2 were tested for each hollow fiber sample. Since the outer surface was the selective layer, the feed was pumped into the shell side and the permeate came out from the fiber lumen forming a cross-flow filtration mode. The feed velocity u_f was kept at about 0.8 m s^{-1} which could minimize the effect of concentration polarization. This was checked by the fact that the permeate flux of studied solutions was very close to the pure water permeate flux (difference less than 5 %). The temperature of feed solution in all experiments was maintained at 20 ± 0.1 °C by a cooling coil (controlled by a water bath, Julabo F32-MV, Germany) inside the feed tank.

The following describes experimental designs and separation procedures:

1) The feed solutions were prepared by dissolving neutral solutes in ultrapure water with a concentration of about 200 ppm. The feed solutions were circulated for about 0.5 hr until the whole system reached the steady state where the permeate flux and solute rejection keep unchanged. The permeate was collected for a predetermined period and the volume flux was measured at different pressures (starting from the lowest ΔP).

2) Nanofiltration experiments were conducted with solutes of progressively higher molecular weights. The membrane was thoroughly flushed with ultrapure water between runs of different solutes. The solute separation data were used for estimating of the mean effective pore size and pore size distribution of the membrane.

3) The electrolyte solutions were prepared by dissolving single salts in ultrapure water with the concentration of 3.4 mol m^{-3}. The same experiment procedures were employed to measure the salts rejection performance as described in the Step 1.

4) The NaCl/MgCl$_2$ and NaCl/Na$_2$SO$_4$ binary salt mixture solutions were prepared at pH 7.0. Ion fractionation performance of membranes was measured at different pressures.

5) NaCl solutions with different pH were prepared with the concentration of 3.4 mol m^{-3}. The ion rejection by membranes was measured at different pressures.

6) Cephalexin solutions at different pH were prepared with a concentration of 200 ppm. The solute rejection experiments were performed according to the same procedure as described in the Step 1.

7) Chromate solutions ([CrVI] = 1.0 & 10.0 mol m^{-3}) were prepared by dissolving K$_2$Cr$_2$O$_7$ in ultrapure water. KOH (1.0 N) and HCl (1.0 N) solutions were used to modify the pH of feed solutions; the solute rejection experiments were performed same as the step 1) with testing sequences from pH 5.1 to pH 12.0, finally pH 3.1.

5.3.   Results and discussion

5.3.1   Effects of spinning conditions on morphology of PBI NF hollow fibers

The first criterion of NF hollow fibers is to withstand high operating pressures. One of the keys to strengthen membrane compression properties is to reduce the numbers and sizes of macrovoids or increase the ratio of outer diameter (OD) to inner diameter (ID). Macrovoids in asymmetric hollow fibers have been considered as mechanical weak points which usually result in membrane failure under high pressures. There are many

types of macrovoids, such as finger-like and tear-drop macrovoids. The causes of their origins have been debated in the last 4 decades. Recently, Li et al. [2004a] have summarized these debates. In short, macrovoids may originate from thermodynamic aspects of chemical potential gradient [McHugh & Yilmaz, 1985; Smolders et al., 1992]; or start from local surface instability, material and stress imbalance, which induce solvent intrusion and capillary flow [Strathmann et al., 1975; Shojaie et al., 1994; Chung & Hu, 1997; Pekny et al., 2003]. Other factors such as Marangoni effects [Shojaie et al., 1994; Levich & Krylov, 1969] and osmosis pressure [McKelvey & Koros, 1996] have also been proposed. Ways to reduce macrovoids have received significant attention. Some of them are 1) using high polymer concentration solutions [Kesting and Fritzsche, 1993]; 2) the addition of high viscosity components [Boom et al., 1992]; 3) spinning at high shear rates [Ren et al., 2002]; 4) the induction of delayed demixing [Kim et al., 2001] or gelation [Lin et al., 2002]; 5) the addition of surfactants [Tsai et al., 2000] and 6) the use of elongational stretch along the spinning line [Wang et al., 2004b & Li et al. 2004b].

In this study, different spinning conditions and bore fluid composition were employed to prepare PBI NF hollow fibers. The objectives are not only to study their effects on membrane structure and separation performance, but also to find proper conditions to minimize macrovoids and to produce NF hollow fibers which can endure high operating pressures. When using an 86/14 DMAc/water (weight ratio) mixture as the bore fluid, Fig. 5.2 shows the resultant hollow fibers full of long finger-like macrovoids across the whole cross-section. Interestingly, the large and long finger-like macrovoids were connected through the inner layer pores as shown at the bottom of Fig. 5.2.

A-1 (Cross-section)   B-1   C-1   D-1

A-2 (Enlarged cross-section) B-2   C-2   D-2

A-3 (Inner surface)   B-3   C-3   D-3

Fig. 5.2. Effects of dope flow rate and elongation rate on the membrane structure of PBI NF
hollow fiber membranes from Batch I. (Bore fluid: DMAc 86 wt%, water 14 wt%)

This cross-section morphology may result from combined effects of a high bore-fluid
flow rate, a soft inner skin induced by the delayed demixing owing to application of the
86/14 DMAc/water mixture, and a rapid phase inversion and membrane shrinkage
occurring at the outer skin. A high bore-fluid flow rate may induce solvent intrusion,
while a delayed demixing may result in a soft nascent skin which is vulnerable to stress
imbalance and solvent intrusion. The water-induced rapid phase inversion and shrinkage
at the outer membrane skin may produce additional hoop stress inward, which helps the
intrusion of bore fluid into hollow fibers. As a result, the resultant PBI hollow fiber
membrane is full of finger-like macrovoids and can only withstand trans-membrane
pressures up to 10 bar. The pure water permeability of this PBI hollow fiber is in the

range of 1.9 ~ 2.5 liter m^{-2} bar^{-1} hr^{-1}, which is less than that (i.e. 3.58 liter m^{-2} bar^{-1} hr^{-1}) of

a flat-sheet composite PBI membrane cast on the polyester non-woven fabric from the

same polymer solution.

Following a previous practice to prepare PBI hollow fiber membranes for reverse

osmosis [Model et al., 1977], a non-solvent, dodecane, was used as the bore fluid to

fabricate PBI NF membranes. Dodecane is an inert hydrocarbon liquid that is immiscible

with both DMAc (the spinning solvent) and water (the external coagulant). Figure 5.3

illustrates the resultant morphology.

| A-1 (Cross-section) | B-1 | C-1 | D-1 |

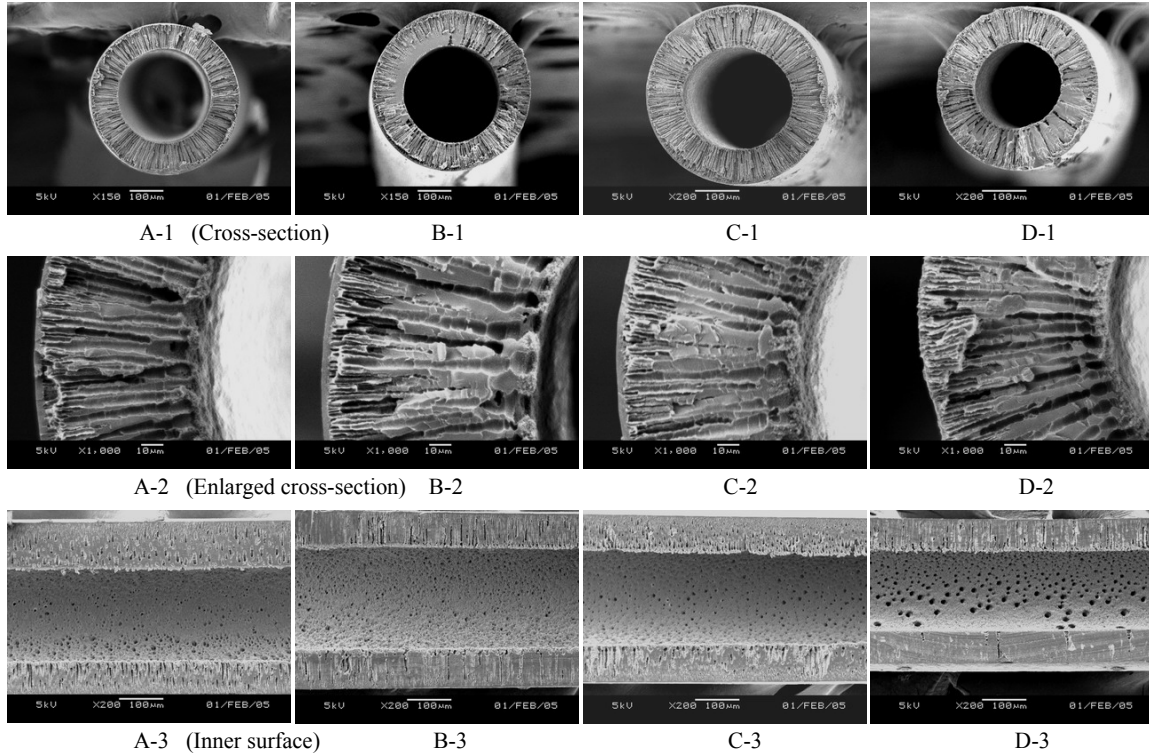| A-2 (Enlarged cross-section) B-2 | C-2 | D-2 |

| A-3 (Inner surface) | B-3 | C-3 | D-3 |

Fig. 5.3. Effects of dope flow rate and elongation rate on the membrane structure of PBI NF
hollow fiber membranes from Batch II. (Bore fluid: Dodecane)

Clearly, dodecane and DMAc/water mixture produce PBI hollow fiber membranes with different morphology. This may arise from the fact that dodecane is an inert hydrocarbon liquid which is immiscible with the spinning solution. As a result, large finger-like macrovoids are fully suppressed and a much denser structure with scattered tiny pores is formed in the cross-section near the inner skin. However, a layer of small and elongated finger-like macrovoids can be observed near the outer layer possibly due to water intrusion during the phase inversion. These PBI hollow fiber membranes can withstand trans-membrane pressures up to 30 bar with a pure water permeability of about 0.40 ~ 1.10 liter m^{-2} bar^{-1} hr^{-1}. Since the removal of dodecane from these hollow fibers is not a trivial process and the pure water permeability is just about the average, attention is given to other bore fluid composition.

Figures 5.4 and 5.5 show the morphology of PBI hollow fiber membranes using 80/20 and 50/50 ethylene glycol/DMAc mixtures as bore fluids, respectively. Similar to the dodecane case, an array of very small but elongated finger-like macrovoids is formed near the outer layer, while the cross-section near the inner skin seems to be a dense spongy structure. The inner skin appears to be relatively dense. This dense inner substructure morphology may arise from fact that ethylene glycol is highly viscous and is inert to the PBI solution. High viscosity may retard the intrusion of ethylene glycol into the hollow fiber, while inertness cannot induce much phase separation.

When the content of DMAc in the bore fluid was increased to 50 wt%, the macroscopic morphology of the resultant membranes shown in Figure 5.5 seems remain the same as

those prepared in Batch III. However, the enlarged pictures illustrated in Figures 5.5 and

5.6 indicate a porous inner skin and a porous underneath substructure. If the DMAc

content in the bore fluid was further increased to 76.7 wt% (Batch V), the integrity of

hollow fiber membranes deteriorated during the sample drying for SEM, as displayed in

Figure 5.7. The integrity of hollow fiber membranes was deteriorated by the scattered

long cracks located across the fiber wall.
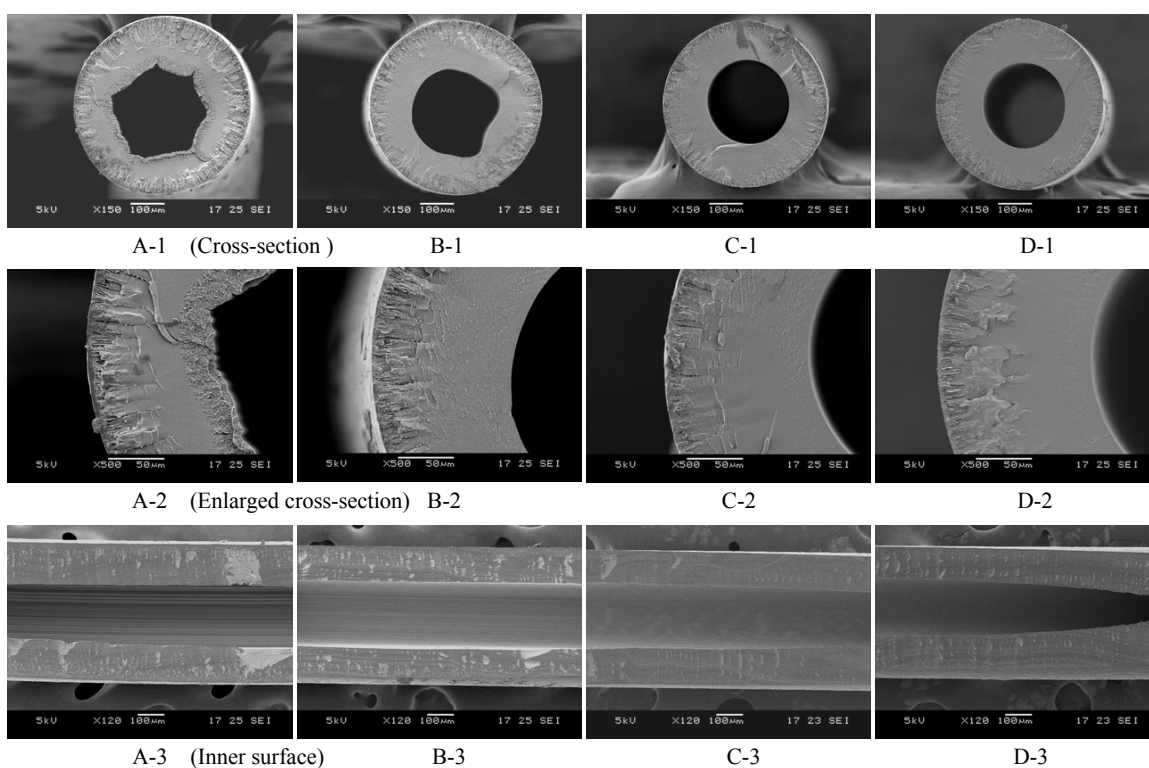
Fig. 5.4. Effects of dope flow rate and elongation rate on the membrane structure of PBI NF
hollow fibers from Batch III. (Bore fluid: Ethylene glycol 80 wt%, DMAc 20 wt%)

This phenomenon shown in Figure 5.7 may result from many factors: 1) the rich DMAc

bore fluid may result in delayed mixing and form a very porous but weak nascent inner

layer; 2) the in-balance of shrinkages across the membrane induces extra stresses for

cracking during the sample drying; and 3) the hydrophilic nature of phase inversion PBI

membranes, which absorb a large amount of water inside, leads to low mechanical

properties when drying [Chung, 1997f].

| A-1 (Cross-section) | B-1 | C-1 | D-1 |

| A-2 (Enlarged cross-section) | B-2 | C-2 | D-2 |

| A-3 (Inner surface) | B-3 | C-3 | D-3 |

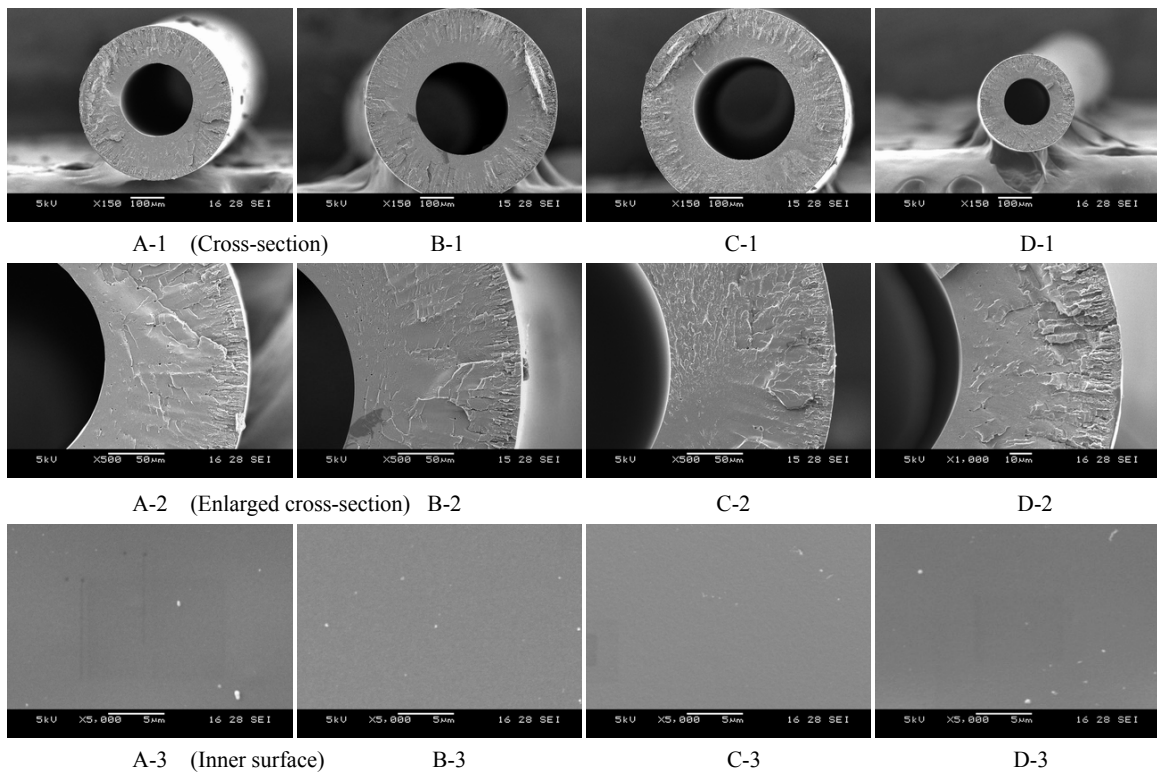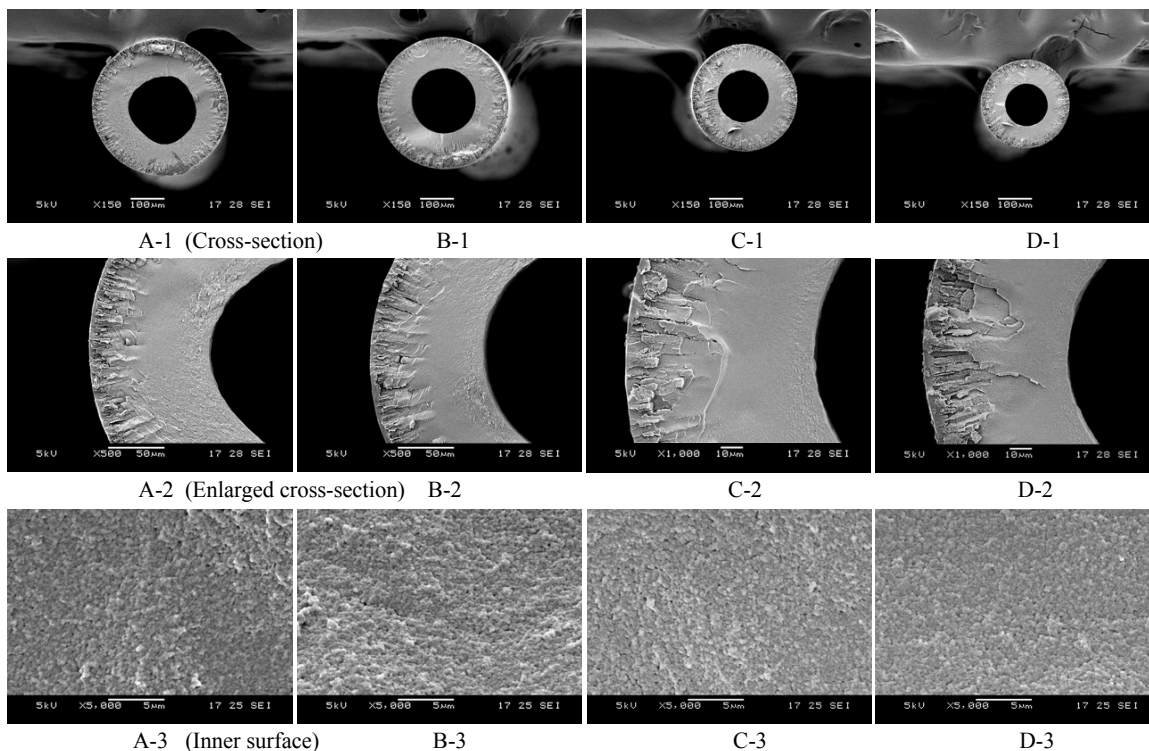Fig. 5.5. Effects of dope flow rate and elongation rate on the membrane structure of PBI NF
hollow fibers from Batch IV. (Bore fluid: Ethylene glycol 50 wt%, DMAc 50 wt%)

Apart from Batches I and V, wet PBI hollow fibers fabricated from Batch II, Batch III

and Batch IV conditions can withstand higher operation pressures up to 30 bar. The

experimental results showed the hollow fiber with a desirable structure can be prepared

by selecting an internal coagulant with a proper nonsolvent strength as indicated by its

precipitation value in the polymer/solvent system. Because Batch IV conditions produce

fibers with more desirable inner skin morphology than other conditions, PBI hollow fiber

membranes spun from Batch IV conditions were further studied for nanofiltration.
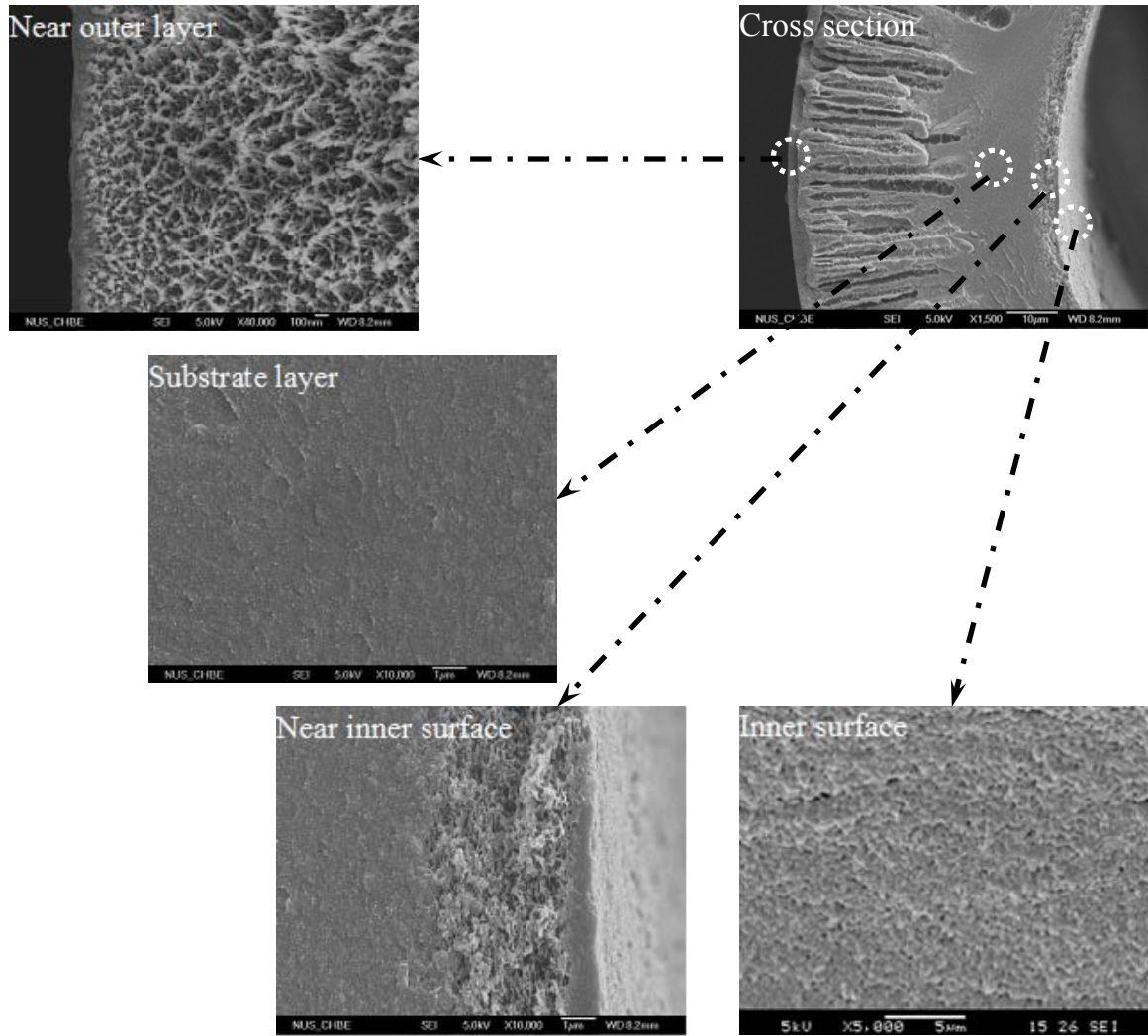
Fig. 5.6. Cross-section and inner surface of PBI NF hollow fiber membrane (*No*. IV-E). Bore fluid: Ethylene glycol/DMAc 50/50 wt %; Dope flow rate: 4.0 ml/min; Elongational draw ratio φ: 13.74

A-1   (Cross-section)   B-1   C-1

A-2   (Enlarged cross-section)   B-2   C-2

A-3   (Inner surface)   B-3   C-3
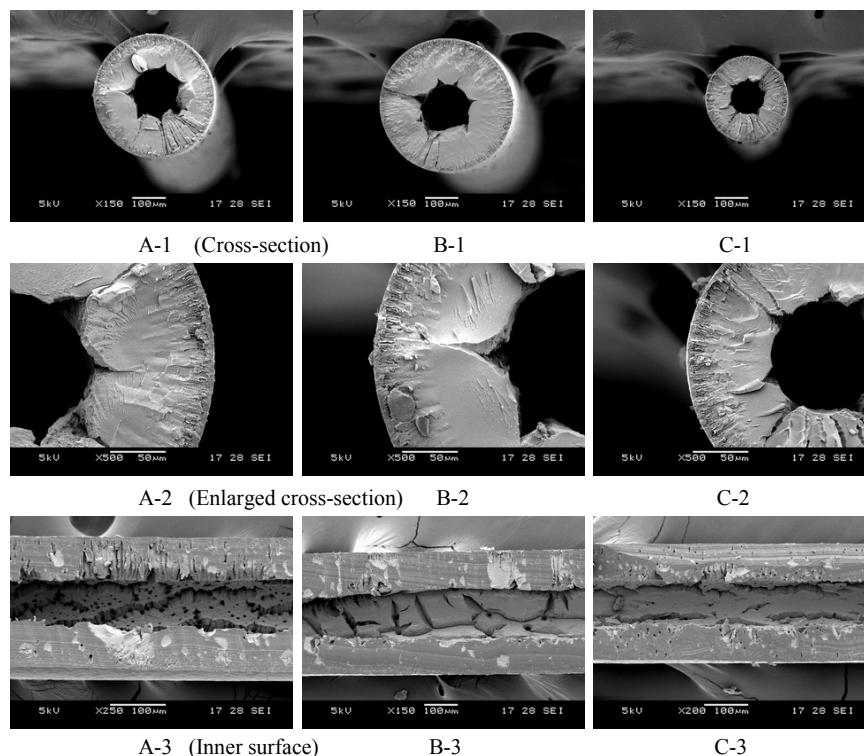
Fig. 5.7. Effects of dope flow rate and elongation rate on the membrane structure of PBI NF hollow fiber membranes from Batch V. (Bore fluid: Ethylene glycol 23.3 wt%, DMAc 76.7 wt%)

5.3.2 Mean pore size and pore size distribution characterized by the solute transport method

Nanofiltration membranes have molecular scale pores on their selective layer which determine the permeate flux and sieving performance. Characterizing the mean pore size and pore size distribution of the newly developed PBI NF membranes by means of the following solute transport method provide essential structure information to predict separation performance. The detailed characterization process can refer to Chapter III.

It has been found that the solute rejection for synthetic membranes can be expressed by a log-normal probability function of solute size, as described in the following equation [Michaels, 1980]:

$$R_T = erf(y) = \frac{1}{\sqrt{2\pi}} \int_{-\infty}^{y} e^{-\frac{u^2}{2}} \, \mathrm{d}u, \quad where \quad y = \frac{\ln r_s - \ln \mu_s}{\ln \sigma_g} \tag{5-4}$$

where R_T is the solute rejection, r_s is the solute radius, μ_s is the geometric mean radius of solute at $R_T = 50\%$, σ_g is the geometric standard deviation about μ_s, defined as the ratio of r_s at $R_T = 84.13\%$ and $R_T = 50\%$. When the solute rejection of a membrane is plotted vs. solute radius on the log-normal probability coordinates, a straight line is yielded as:

$$F(R_T) = A + B \, (\ln r_s) \tag{5-5}$$

By ignoring influences of the steric and hydrodynamic interaction between solute and pores on the solute rejection, the mean effective pore radius (μ_p) and the geometric standard deviation (σ_p) can be assumed to be the same as μ_s and σ_g, respectively [Singh et al., 1998]. Therefore, based on μ_p and σ_p, the pore size distribution of an NF membrane can be expressed as the following probability density function [Aimar et al., 1990]:

$$\frac{\mathrm{d}R_T(r_p)}{\mathrm{d}r_p} = \frac{1}{r_p \ln \sigma_p \sqrt{2\pi}} \exp\left[-\frac{(\ln r_p - \ln \mu_p)^2}{2(\ln \sigma_p)^2}\right] \tag{5-6}$$

where r_p is the effective pore radius of the membrane. The values of μ_p and σ_p determine the position and sharpness of the distribution curves, respectively.

For PBI NF hollow fibers fabricated in Batch IV, the solute rejection vs. solute Stokes radius curves are plotted on a log-normal probability graph at the pressure of 20 bar, as illustrated in Figure 5.8. By fitting Eq. (5-5), straight line relationships are obtained with

reasonable high correlation coefficients ($r^2 > 0.96$). Table 3 lists the mean effective pore

size μ_p at $R_T = 50$ %, and σ_p, the geometric standard deviation about μ_p, calculated from

the plots. The molecular weight cutoff (MWCO, molecular weight at $R_T = 90\%$) can also

be calculated from these straight lines and Eq. (5.7). The pore size distributions of the

PBI membranes calculated from Eqs. (5.4) & (5.6) are depicted in Figures 5.9 & 5.10. It

can be seen that the pore size distribution become narrow with an increase in the

elongational rate.
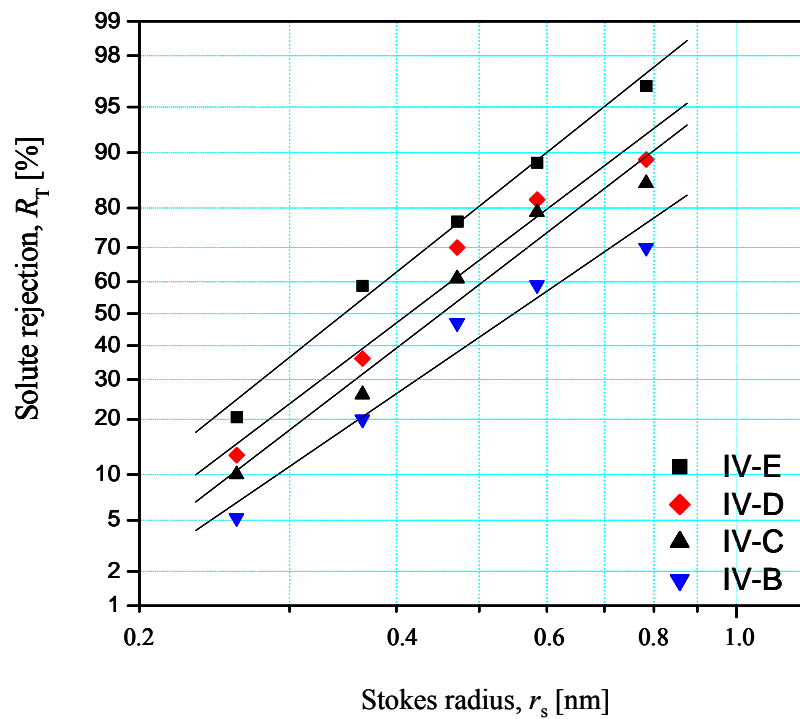
Fig. 5.8. Effective rejection curves (rejections of solutes versus their Stokes radii) plotted on the
log-normal probability co-ordinate system for PBI NF hollow fibers spun at different elongation
rates (Testing pressure: 20 bar).

Table 5.2 Outside diameter (OD), pure water permeability (PWP), mean of effective pore size (r_p), geometric standard deviation (σ_p) and the molecular weight cut off (MWCO) of PBI NF hollow fibers spun from Batch IV

Fiber ID	Elongational ratio, φ (-)	ID (μm)	OD (μm)	PWP (l m^{-2} bar^{-1} hr^{-1})	r_p (nm)	σ_p (-)	MWCO (Da)
IV-B	3.59	280	640	0.75	0.550	1.64	1,778
IV-C	5.90	220	500	1.00	0.453	1.55	1,016
IV-D	8.26	180	420	1.42	0.413	1.57	853
IV-E	13.74	160	335	1.86	0.348	1.53	551
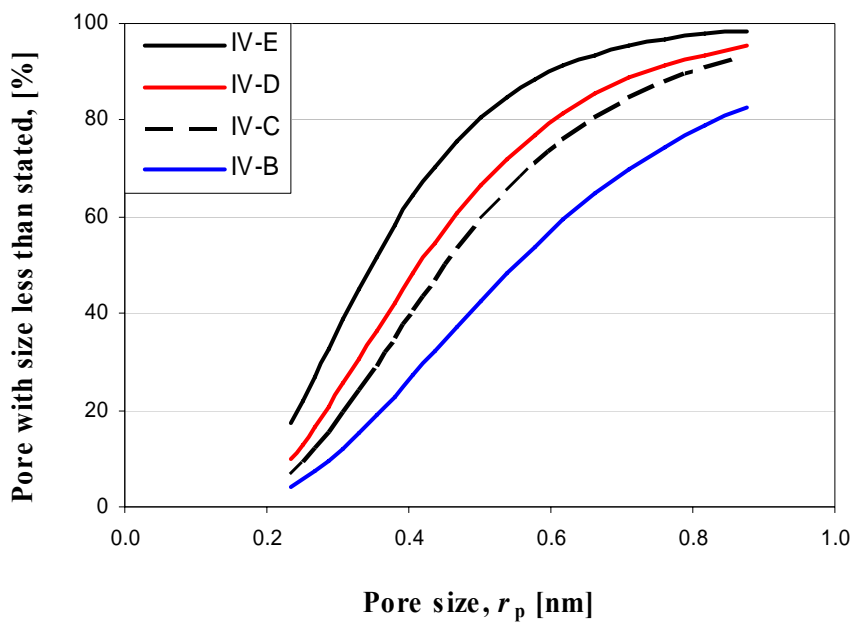
Fig. 5.9. Cumulative pore size distribution curves of the PBI NF hollow fiber membranes spun at different elongation rates.
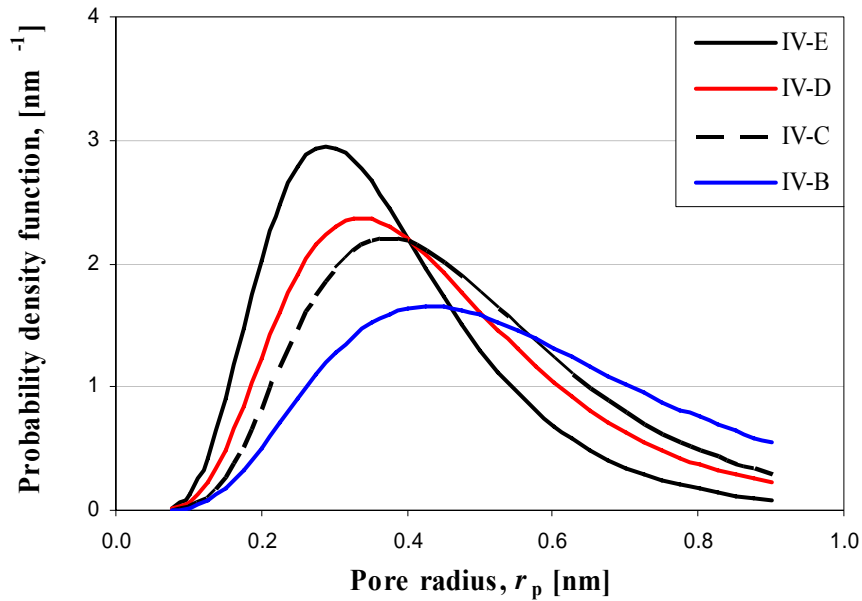
Fig. 5.10   Probability density function curves of the PBI NF hollow fiber membranes
spun at different elongation rates.

From Table 5.2, it is found that the pure water permeability increases and the mean effective pore radius decreases when increasing elongational ratio at the same dope flow rate. The results appear to confirm that the macromolecular packing and orientation induced by elongation stress intensively influence the phase inversion process [Chung, 1997c] although the microstructure transformation cannot be visibly detected from SEM observation. Since surface pores are considered as the interstices among nodules, the elongation stress may elongate the nodule dimension as well as de-aggregate nodules. The former may result in better packing and decrease in pore size, while the latter may increase in surface porosity.

In the following parts, the characterizations of ion separation performance and surface charge property of PBI NF hollow fiber membranes IV-E are performed. These NF hollow fibers have a mean effective pore size of 0.348 nm in radius and the PWP of 1.86 liter m^{-2} bar^{-1} hr^{-1} which is much less than that of flat sheet PBI composite membrane at 3.58 liter m^{-2} bar^{-1} hr^{-1} cast from the same polymer solution. Compared to flat sheet membrane, PBI hollow fiber membranes (IV-E) have a smaller mean pore size and narrow pore size distribution (Table 5.3). The cumulative pore size distribution curves and the probability density function curves of the PBI membranes are represented in Fig. 5.11. This appears to confirm the effect of macromolecular packing induced by elongational stress from gravity and extraneous stretching on the membrane structure during dry-jet wet spinning.

Table 5.3 Pure water permeability (PWP), mean of effective pore size (r_p), geometric standard deviation (σ_p) and the molecular weight cut off (MWCO) of PBI membrane fabricated from same polymer solution

Membrane	PWP ($l\ m^{-2}\ bar^{-1}\ hr^{-1}$)	r_p (nm)	σ_p (-)	MWCO (Da)
PBI hollow fiber IV-E	1.86	0.348	1.53	551
PBI flat sheet membrane	3.85	0.842	1.55	4,032

5.3.3 Ion separation and surface charge property of the PBI NF membranes using single electrolyte solutions

Because the PBI NF membranes seem to be positively charged at pH 7.0, they may show different rejections to various valent cations and anions. At the same molar concentration

a)

b)
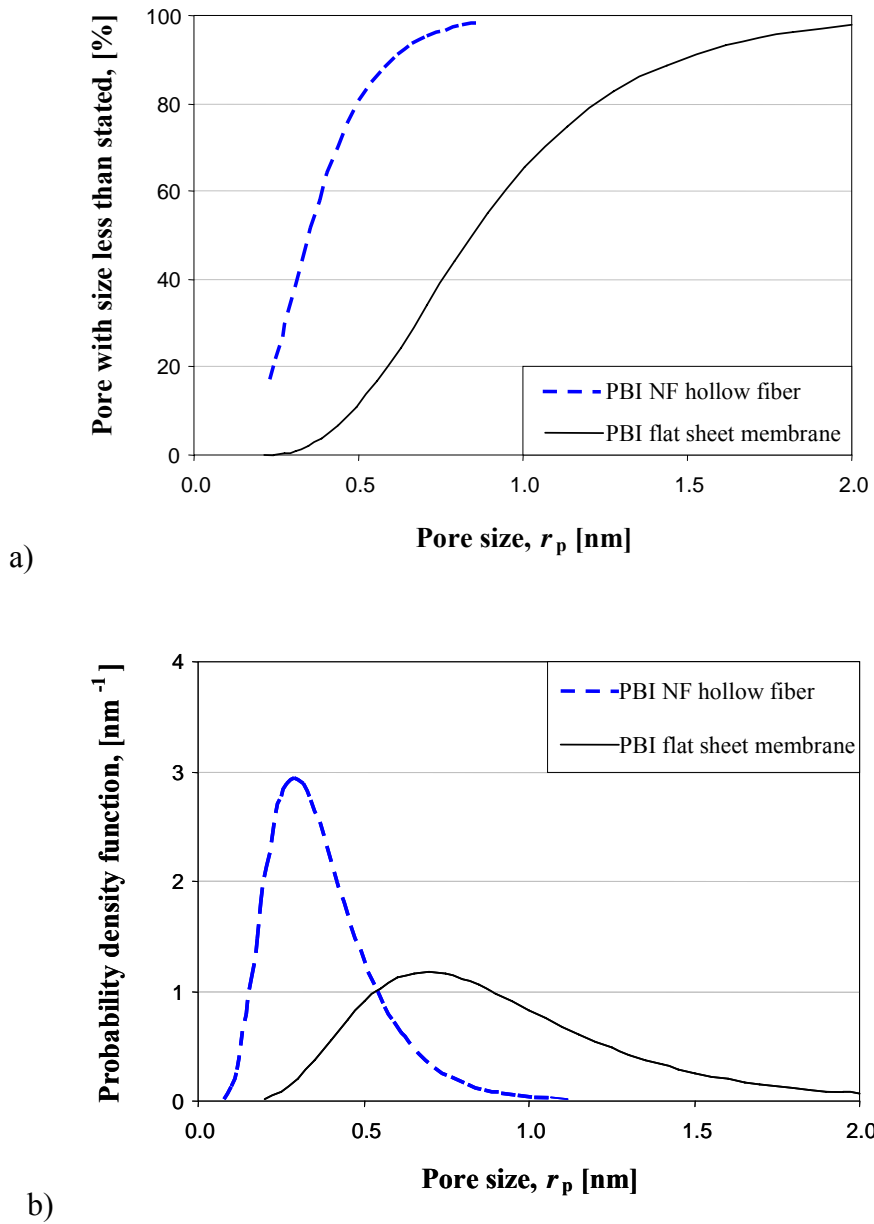
Fig. 5.11. a) Cumulative pore size distribution curves & b) Probability density function curves for the PBI hollow fiber membranes (IV-E) and flat sheet composite membranes respectively

(3.4 mol m^{-3}), the rejection of four types of single electrolytes in their solutions were measured at different pressures, as shown in Figure 5.12. They follow the order of R (MgCl$_2$) > R (MgSO$_4$) > R (Na$_2$SO$_4$) > R (NaCl). Interestingly, the PBI membranes exhibit the highest rejection to divalent cations and lower rejection to divalent anions, but

the lowest rejection to monovalent ions. This phenomenon seems to deviate from the Donnan exclusion mechanism, which has also been observed elsewhere [Schaep et al., 1998; Yaroshchuk, 2000]. This may be attributed to the amphoteric property of PBI.
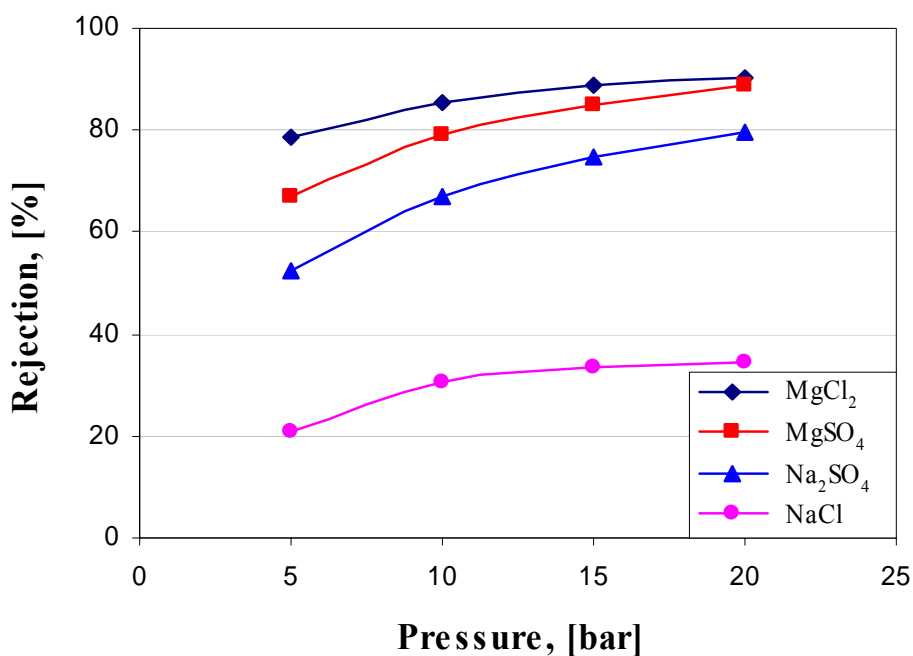
Fig. 5.12. Rejection of different salts as a function of pressure
(the bulk single salt concentration: 3.4 mol m^{-3}, pH 7.0).

In addition, the solute rejection increases with the increase in pressures. Since the water permeate flux through the membrane is linearly related to the applied pressure difference, whereas the solute flux is dependent on several factors: 1) the concentration gradient over the membrane; 2) the interaction between solute and fluid; and 3) the water permeate flux. As a result, when increasing the pressure difference, the water flux increases relatively faster than the solute flux [Garcia-Aleman & Dickson, 2004]. It causes a decrease in solute permeate concentration and an increase in solute rejection.

5.3.4   Ion fractionation by PBI NF membranes in the electrolyte mixture solutions

Generally, most electrolyte solutions may contain several salts which need to be separated through the membrane process. In this part, two kinds of binary salt mixtures were employed to test the ion fractionation performance of the as-spun PBI NF membrane. For example, as shown in Figure 5.13, a NaCl/MgCl$_2$ binary salt solution (at pH 7.0) with a cation molar concentration ratio Na$^+$/Mg^{2+}of 1.0, Na$^+$ ions are forced to permeate preferentially compared to Mg^{2+} ions since Na$^+$ ions have lower valence and smaller hydrated ionic size than Mg^{2+} ions. Cl$^-$ ions also permeate the membrane together with Na$^+$ to maintain electroneutrality at both sides of the membrane phase in accordance with the Donnan principle. As a result, Mg^{2+} ions and Na$^+$ ions could be fractionated by the PBI NF membranes due to ion competition. In addition, along with an increase in pressure, the rejection of Mg^{2+} and Na$^+$ increases because an increase in water permeate flux results in a decrease in permeate concentration.

Similarly, as shown in Figure 5.14, in the NaCl/Na$_2$SO$_4$ binary salt solution (at pH 7.0) with an anion molar concentration ratio Cl$^-$/SO$_4^{2-}$ of 1.0, Cl$^-$ ions are forced to permeate preferentially compared to SO$_4^{2-}$ ions since Cl$^-$ has a lower valence and smaller hydrated ionic size. Na$^+$ ions also permeate membrane together with Cl$^-$ to maintain electroneutrality at both sides of the membrane phase, in accordance with the Donnan principle. Moreover, the negative rejection of chloride ions (Cl$^-$ concentration in permeate is higher than that in feed solution) is observed at different pressures. Along with an increase in pressure, the rejection of SO$_4^{2-}$ increases; while the rejection of Cl$^-$

firstly decreases to a minimum, then increases. Clearly, SO_4^{2-} and Cl^- anions can be fractionated by the fabricated PBI NF membranes.
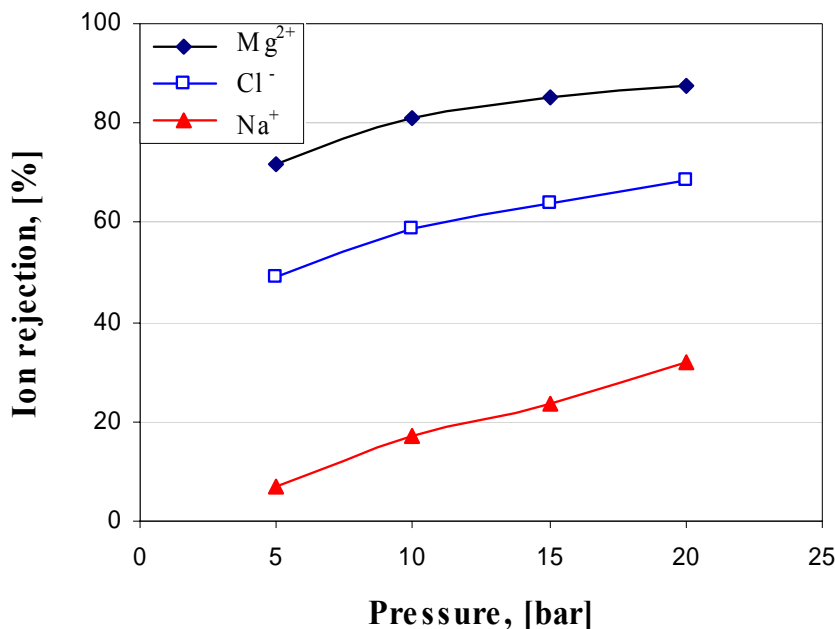
Fig. 5.13. Ion rejection in the mixture of $NaCl/MgCl_2$ solution as a function of applied pressure
($[NaCl] = 3.4$ mol m^{-3}, $[MgCl_2] = 3.4$ mol m^{-3}, pH 7.0)

The PBI membranes may be applied in the chlor-alkli process for the removal of trace sulphate form high concentrated NaCl solution to avoid damage to ion-exchange membranes [Schäfer et al., 2005]. The negative NaCl rejection and high SO_4^{2-} rejection allow achieving a high degree of purification with reduced processing cost and purge volume and lowering the environmental impact [Perry and Linder, 1989].

However, it is still not clear why the PBI NF membranes exhibit higher rejection to both divalent cations and divalent anions compared to monovalent ions at pH 7.0. The possible explanation may be due to the existence of amphoteric imidazole group within PBI molecules.
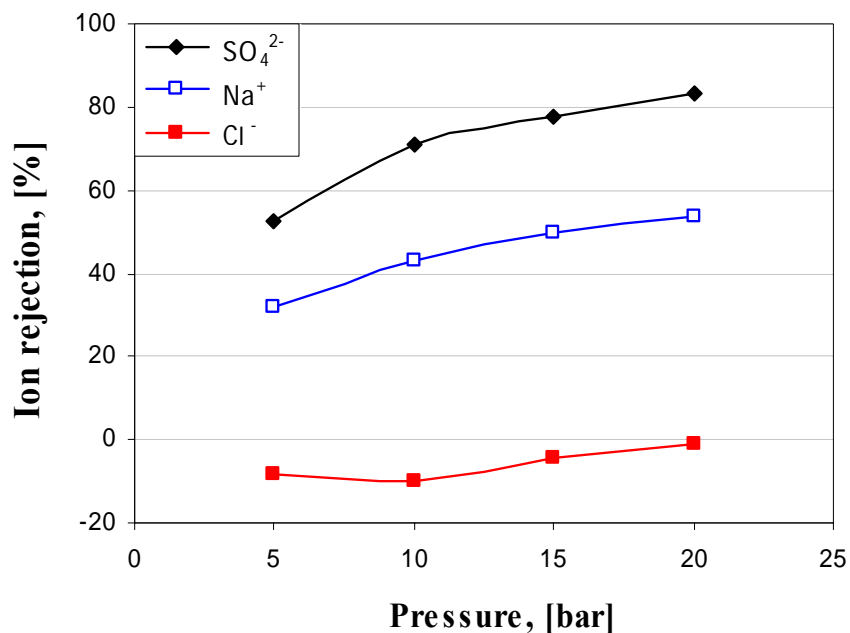
Fig. 5.14. Ion rejection in the mixture of $NaCl/Na_2SO_4$ solution as a function of applied pressure
($[NaCl] = 3.4$ mol m^{-3}, $[Na_2SO_4] = 3.4$ mol m^{-3}, pH 7.0)

5.3.5　Effects of solution pH on NaCl rejection

The separation performance of the PBI NF membrane largely depends on the surface charge which is influenced by pH of the contacted media. A V-shape trend of NaCl rejection is shown in Figure 5.15, which reflects the surface charge property under different pH values. A minimum ion rejection appears at pH 7.0 (near pKa of the imidazole group in PBI molecules). This result seems to be similar to the amphoteric behavior of metal oxide group of the inorganic membranes under different pH [Guizard & Rios, 1996; Weber et al., 2003].
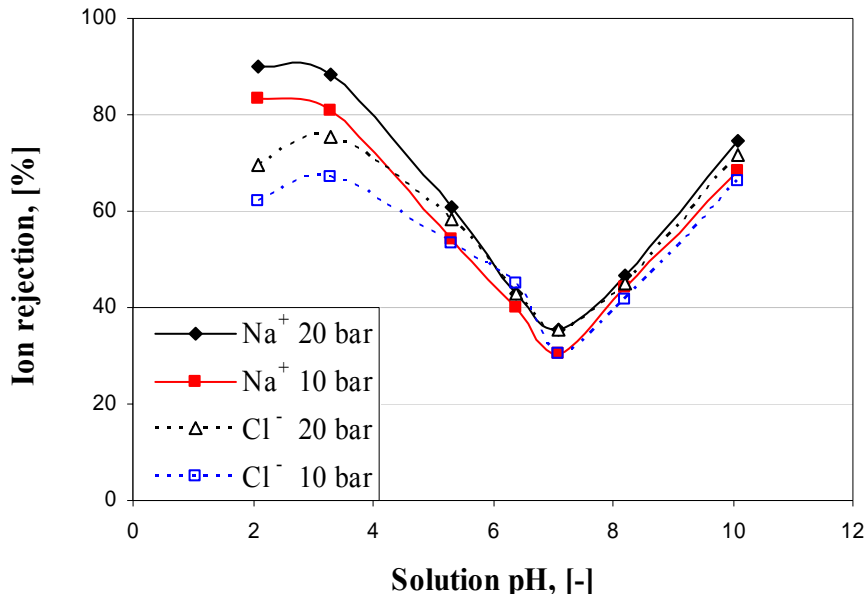
Fig. 5.15. Rejection of NaCl (3.4 mol m^{-3}, 20ºC) as a function of pH under different pressures
(Solution pH was adjusted by adding 1.0 N HCl or 1.0 N NaOH)

It is possible to speculate that the PBI membranes have different charge signs based on pH values of the media, i.e. positively charged at lower pH and negatively charged at higher pH). It is also found that at very low pH (around pH 2.0) the rejection of Cl$^-$ decreases while rejection of Na$^+$ increases along with a decrease in pH. Because HCl solution was used to adjust pH of NaCl solution, the NaCl solution contains Na$^+$, Cl$^-$ and an excess of H$^+$ ions (10 mol m^{-3}) at pH 2.0. As compared to Na$^+$, H$^+$ can preferably permeate through membrane, and Cl$^-$ permeates with H$^+$ to keep electroneutrality of the solutions. Thus, at pH 2.0, the PBI membrane shows lower rejection of Cl$^-$ but higher rejection of Na$^+$. However, under high pH over 7.0, the identical rejections of Na$^+$ and Cl$^-$ may be attributed to their similar ion sizes (around 3.6 Å in diameter) and close diffusion coefficients.

5.3.6   Cephalexin separation performance of PBI NF hollow fiber membranes

As an amphoteric electrolyte molecule in the aqueous solution, cephalexin acts as both base (proton acceptor) and acid (proton donor) since cephalexin molecules have both the amino group ($-NH_2$) and the carboxyl group ($-COOH$) similar to amino acids. Depending on the pH of solution, cephalexin can be positively charged (acidic) at pH < pI (Isoelectric point, around 4.5 ~ 5.0), negatively charged (basic) at pH > pI and net neutral (dipolarions) at pH = pI. In the dipolar form, the amino group is protonated ($-NH_3^+$) and the carboxyl group is dissociated ($-COO^-$). Based on their dissociation constants (pK_as), the fraction of different ionization state of cephalexin at different pH can be expressed by the Henderson-Hasselbalch equation [Stryer, 1995] plotted in Figure 5.16 (blue curves):

$$pH = pK_a + \log(\frac{[proton\ \ acceptor]}{[proton\ \ donor]})$$

(5.8)

As shown in Figure 5.16, the rejection of cephalexin by PBI NF membrane shows a V-shape trend along with an increase in pH at different pressures and a minimum rejection (about 86% and 78% under 20 and 10 bar, respectively) appears at around pH 5.0 (near pI of cephalexin molecules).

Although cephalexin has almost the same molecular weight with saccharose, the rejection of cephalexin (about 86.5%) at the pH around the pI (4.5 ~ 5.0) which cephalexin molecules as a whole is zwitterion without net charge, is higher than that of saccharose (around 76.8%). This may be due to the contribution of molecular shape to the solute

transport [Kiso et al., 2001]. By taking into account of molecular configuration, cephalexin molecule is more like a rod with the length of 1.6 nm away from a sphere while saccharose molecule is 1.2 nm in length while their molecular widths are quite close, which simulated from *Cerius*2 molecular simulation software shown in Figure 3.16. Therefore, the steric hindrance for cephalexin may be much larger than that of saccharose. As a result, at the pH near pI of cephalexin, the steric exclusion plays a main role on the rejection of cephalexin.
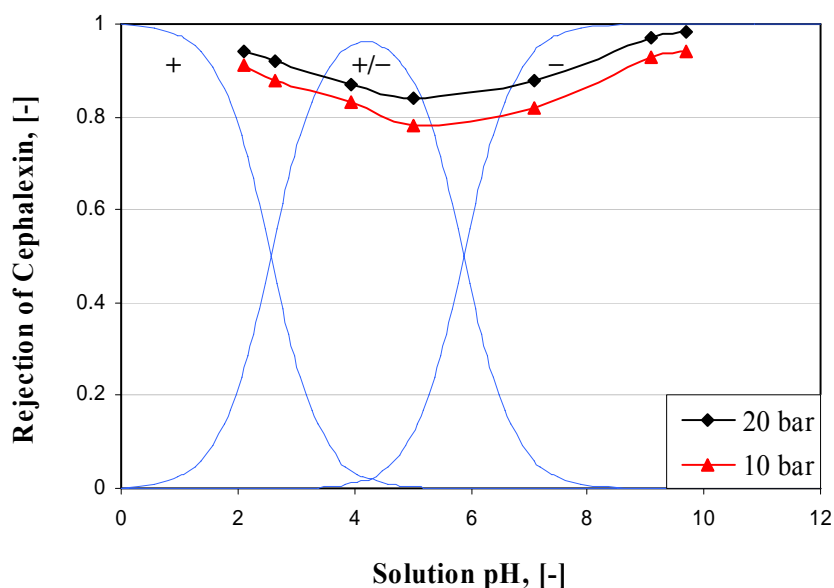
Fig. 5.16. Rejection of cephalexin (200 ppm) vs. the solution pH under different pressures
(Blue curves express the fraction of ionization states (signs) of cephalexin molecules)

These results confirm that the rejection of cephalexin is dependent on the pore size (steric exclusion) and the electrostatic interaction between solutes and membrane. The pH of the solution has the dominant effect on the separation of cephalexin because pH determines

the ionization states of the cephalexin molecules and surface charge characteristics of the PBI membranes.

5.3.7 Removal of Chromate by the PBI NF Membrane

In aqueous solutions, the pH and ionic strength will determine the major Cr(VI) species based on the Cr(VI)-H_2O equilibrium as shown in Figures 5.17 & 5.18 (the blue curves). At pH 2 ~ 5, $HCrO_4^-$ and $Cr_2O_7^{2-}$ ions coexist and their concentrations appear independent of pH, while pH > 6.5, CrO_4^{2-} ions predominates [Tandon et al., 1984]. In addition, the relative amounts of $HCrO_4^-$ and $Cr_2O_7^{2-}$ in the acidic aqueous media is highly dependent on the total Cr(VI) concentration. At lower concentration of Cr(VI), the major Cr(VI) species is $HCrO_4^-$, while $HCrO_4^-$ converts to its dimer form of divalent $Cr_2O_7^{2-}$ at higher concentration.

$$H_2CrO_4\ (aq) + OH^-(aq) \Leftrightarrow HCrO_4^-\ (aq) + H_2O\ (l) \qquad (5\text{-}9)$$

$$HCrO_4^-\ (aq) + OH^-\ (aq) \Leftrightarrow CrO_4^{2-}\ (aq) + H_2O\ (l) \qquad (5\text{-}10)$$

$$2\ CrO_4^{2-}\ (aq) + 2\ H^+\ (aq) \Leftrightarrow Cr_2O_7^{2-}\ (aq) + H_2O\ (l) \qquad (5\text{-}11)$$
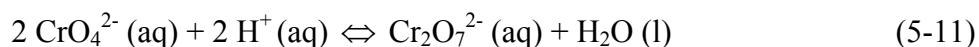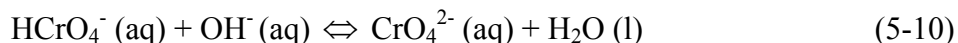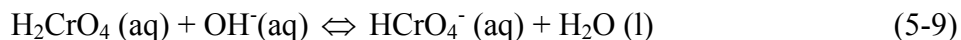
Thus, chromate chemical specifications may play an important role on the transport of chromate ions across the membrane. It can be seen that the chromate rejection by the PBI membrane exhibits a V-shape trend with the increase in pH.

From Figure 5.17 ([CrVI] = 1.0 mol m^{-3}), with the increase in pH, the chromate rejection rises up to 99.2 % at pH 9 and a minimum rejection of 27.5 % near pH 7 under the pressure of 20 bar. The pH of the solution has the dominant effect on the separation of

chromate because pH determines the ionization state of the chromate anions and the surface charge characteristics of the PBI membranes.
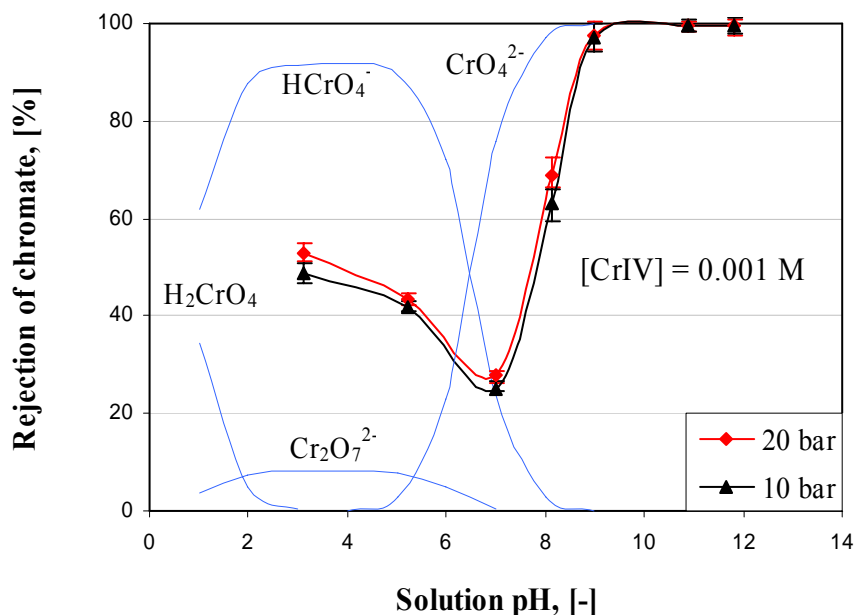
Fig. 5.17. Rejection of chromate ($[CrVI] = 1.0$ mol m^{-3}, 20ºC) as a function of solution pH under different pressures (Solution pH was adjusted by adding 1.0 N HCl or 1.0 N KOH)

While for the chromate solution with $[CrVI]$ of 10.0 mol m^{-3}, the PBI membranes show chromate rejection of only 95.7 % at pH 12 and a minimum rejection of 20 % at about pH 6 (in Figure 5.18). This result demonstrates that the ion strength is another crucial factor that decreasing the chromate rejection. In addition, in the higher concentration of acidic Cr(VI) solution, the existence of large amount of $Cr_2O_7^{2-}$ ions coupled with the positively charged property of PBI membrane at pH less than 5.0 may be contributed to the lower chromate rejection.
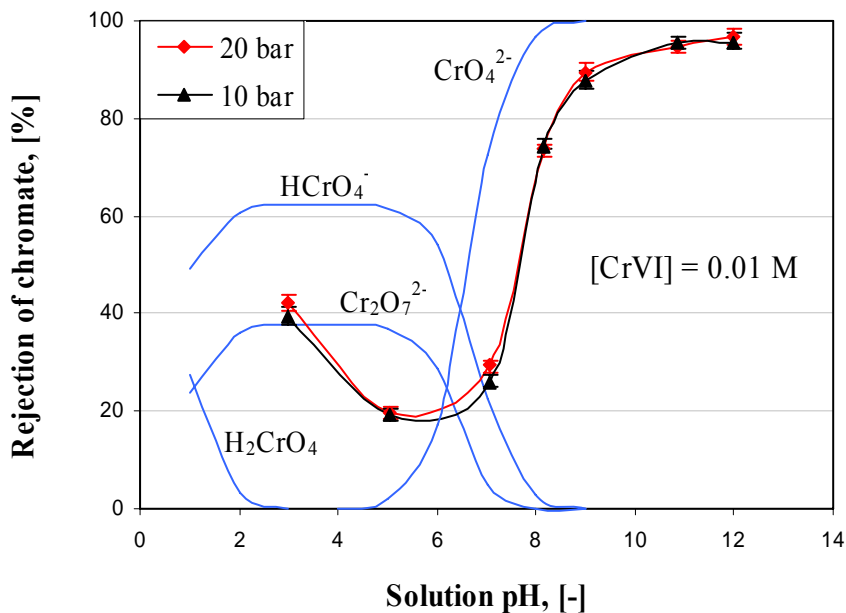
Fig. 5.18. Rejection of chromate ([CrVI] = 10.0 mol m^{-3}, 20ºC) as a function of pH under different pressures (Solution pH was adjusted by adding 1.0 N HCl or 1.0 N KOH)

As a consequence, although having lower chromate rejection at low pH, PBI NF hollow fiber membranes can be efficiently employed in the separation of CrVI from aqueous media under higher pH up to 12. Compared to the rejection at [CrVI] = 1.0 mol m^{-3}, the PBI NF membrane shows lower rejection to chromate at [CrVI] = 10.0 mol m^{-3} due to the high ion strength.

5.4 Conclusions

High pressure sustainable PBI nanofiltration hollow fiber membranes have been fabricated through the phase inversion process. Because of the strong interaction between PBI and water, the formation of finger-like macrovoids inside the PBI hollow fiber

cannot be avoided when water was employed as the external coagulant. However, by using the mixture of ethylene glycol and DMAc as the bore fluid solution, the macrovoid-free formation can be produced in the inner substrate layer of PBI hollow fiber membranes. The resultant PBI NF hollow fiber membranes can withstand higher pressures up to 30 bar. The composition and property of bore fluid play an important role on the morphology of the resultant hollow fiber membranes.

PBI NF hollow fiber membranes spun from Batch IV-E have the mean effective pore size of 0.348 nm in radius and the narrow pore size distribution, and the PWP of 1.86 liter m^{-2} bar^{-1} hr^{-1}. They show higher rejection to divalent cations, lower rejection to divalent anions and the lowest rejection of monovalent ions for single salt solutions, which seems not to be correlated with the Donnan exclusion mechanism. While for the binary NaCl/Na$_2$SO$_4$ mixture solution, the negative rejection of Cl$^-$ and high rejection of SO$_4^{2-}$ can be explained by the ion competing transport mechanism. The PBI membranes may be applied in the chlor-alkli process for the removal of trace sulphate form high concentrated NaCl solution. In addition, in the binary NaCl/MgCl$_2$ mixture solution, PBI membrane exhibits a much higher rejection of Mg^{2+} over Na$^+$. As a result, divalent ions and monovalent ions can be effectively fractionated in their mixtures by the PBI membrane.

Due to the amphoteric property of PBI molecules, the PBI membrane shows a V-shape trend of NaCl rejection under different pH values, which is attributed to the surface charge characteristics determined by solution pH. The newly developed PBI NF hollow fiber membranes can concentrate and purify cephalexin from the aqueous solutions by

adjusting operation conditions. The high cephalexin rejection is based on the interaction between the charged membrane and the ionized cephalexin molecules under different pH. Moreover, the PBI NF hollow fiber membranes exhibit higher chromate rejection that can be employed to effectively separate chromate from aqueous solutions under high pH based on the interaction between the charged PBI membrane and chromate anions.

Fabrication of Polybenzimidazole (PBI) Nanofiltration Hollow Fiber Membranes
Applied in Separation of Pharmaceutical and Removal of Chromate

165

CHAPTER SIX

CONCLUSIONS AND RECOMMENDATIONS

6.1. CONLUSIONS

In comparison to flat sheet membranes, the hollow fiber configuration is a favorite for modules in membrane separation. However, development of high pressure sustainable hollow fiber membranes for liquid separation has not yet been optimal. In general, finger-like macrovoids formed during the phase inversion are considered to be the mechanically weak points since it induces membrane collapse under higher pressures. The first part of this thesis has been focused on effects of dope flow rate and flow angle within spinnerets on morphology, water permeability and separation performance of poly(ethersulfone) ultrafiltration hollow fiber membranes. Wet-spinning was purposely chosen to fabricate the hollow fibers without extra drawing. Therefore, effects of gravity and elongation stress on fiber formation could be significantly reduced and the orientation induced by shear stress within the spinneret could be frozen into the wet-spun fibers. The ratio of dope over bore fluid flow rate was specially kept constant to reduce the complicated coupling effects (dragging, uneven demixing) of bore fluid flow on fiber formation during wet-spinning.

Experimental results suggest that higher dope flow rates (shear rates) within the straight spinneret produce ultrafiltration hollow fiber membranes with smaller pore sizes on the denser skin layers due to the enhanced molecular orientation. Hence, the pore size and the

water permeability decrease, but the solute separation increases with an increase in shear rate. *On the other hand*, hollow fibers spun from a conical spinneret has smaller mean pore sizes but with larger geometric standard deviations, which exhibiting lower water flux and greater solute separation than hollow fibers spun from a traditional straight spinneret. As a result, the flow angle in the spinneret is another variable in controlling the pore size and pore size distribution of hollow fibers' selective layer. Moreover, a maximum in the solute separation was found for hollow fibers spun from both spinnerets with different flow angles as shear rate was increased. In addition, from SEM observation, it was shown that finger-like macrovoids responded quite differently for the 90° straight and 60° conical spinnerets when shear rate was increased. Finger-like macrovoids can be significantly suppressed and almost disappear in the fibers spun from the 90° spinneret at higher dope flow rates. However, this phenomenon could not be observed for the 60° conical spinneret under similar dope flow rates.

During dry-jet wet spinning process, finger-like macrovoids in asymmetric hollow fiber membranes could be completely eliminated at higher elongational draws. It was found that the number of macrovoids and the number of macrovoid layer decreased with an increase in elongational draw ratio, while the dimension of macrovoids varied with increasing elongational draw ratio until the macrovoids were fully eliminated. This result indicated that the elongational stress induced by elongational draw may play a much more important role than other spinning factors on hollow fiber membrane morphology. These results suggest that ultrafiltration hollow fiber membranes without finger-like macrovoids can be fabricated under higher shear rates and elongational rate during phase inversion process.

The other part of this thesis engaged in dealing with the fabrication and characterization of nanofiltration membranes. Two negatively charged nanofiltration membranes (NADIR$^®$ N30F and NF PES10) were systematically characterized by estimating their structural parameters (effective pore radius r_p and the ratio of membrane porosity to effective membrane thickness $A_k/\Delta x$) from SHP model. The mean pore size estimated from neutral solute rejection by two different methods were comparable to each other. The effective charge density (ϕX) of membranes was determined by TMS model from the rejection data of NaCl under different molar concentrations, and it was related to the salt concentration of bulk solutions. The negatively charged membranes showed different rejections to different valent anions and cations due to Donnan exclusion mechanism. While in the binary NaCl/Na$_2$SO$_4$ mixture solution, negative rejection of Cl$^-$ by the membranes happened by virtue of ion competing transport. As a dipolar molecule, the rejection of cephalexin was investigated in the consecutive lab-scale experiments by adjusting the solution pH to modify the ionization states of cephalexin molecules. The operating pressures and ion strength of solution can also affect the rejection of cephalexin. It is possible to concentrate and purify the cephalexin solution through adjusting operation conditions.

Due to its outstanding thermal, physical and chemical stability, polybenzimidazole (PBI) was used to fabricate nanofiltration membranes. The chemically modified PBI composite flat sheet NF membrane was fabricated through the controlled chemical modification by the *p*-Xylylene dichloride. The pure water permeability of the modified PBI membrane can be controlled through adjusting the treatment period in the *p*-Xylylene dichloride solution. Characterized by the solute transport method, the modified PBI membrane had a

decreased mean pore size of 0.36nm in radius and the narrowed pore size distribution compared to the as-cast PBI membrane. The resultant composite PBI nanofiltration membranes showed higher rejection to di-valence cations and anions, which can be applied to fractionate $NaCl/Na_2SO_4$ and $NaCl/MgCl_2$ binary salt mixtures. The separation performance of the PBI NF membrane depends on the pH value of the contacted solutions. The membranes showed a V-shaped trend of rejection to Cl^- and Na^+ ions along with the increase in pH, which is similar to ceramic membranes and can be applied to separate and purify cephalexin, amino acid and other pharmaceuticals from their aqueous solutions.

High pressure sustainable PBI nanofiltration hollow fiber membranes have been fabricated through the phase inversion process. Because of the strong interaction between PBI and water, the formation of finger-like macrovoids inside the PBI hollow fiber cannot be avoided when water was employed as the external coagulant. However, by using ethylene glycol and DMAc mixture as the bore fluid solution, the macrovoid-free formation can be produced in the inner substrate of PBI hollow fiber membranes. The resultant PBI NF hollow fibers can withstand higher pressures up to 30 bar. With an increase in elongational rate, the pure water permeability of the resultant PBI NF membranes increased while the mean effective pore size decreased. PBI NF hollow fiber membranes (IV-E) have a mean effective pore size of 0.348 nm in radius and a narrow pore size distribution. They show higher rejection to divalent cations, lower rejection to divalent anions and the lowest rejection to monovalent ions, which seems not to be correlated with the Donnan exclusion mechanism. While for the binary $NaCl/Na_2SO_4$ mixture solution, the negative rejection of Cl^- and high rejection of SO_4^{2-} can be explained by the ion competing transport mechanism.

The PBI membranes may be applied in the chlor-alkli process for the removal of trace sulphate form high concentrated NaCl solutions. In addition, in the binary NaCl/MgCl$_2$ mixture solution, PBI membrane exhibits a much higher rejection of Mg^{2+} over Na$^+$. Thus, divalent ions and monovalent ions can be fractionated in their mixtures by the PBI membrane. Based on the amphoteric property of PBI molecules, the PBI membrane shows a V-shaped trend of NaCl rejection under different pH, which is attributed to the surface charge characteristics influenced by pH in the media. The newly developed PBI NF membranes can concentrate and purify cephalexin from the aqueous solutions by adjusting operation conditions based on the interaction between the charged membrane surface and the ionized cephalexin molecules under different pH. Moreover, it is possible to effectively separate chromate from aqueous solutions with the PBI NF hollow fiber membranes under high pH up to 12 based on the interaction between the charged membrane and chromate ions.

6.2 RECOMMENDATIONS

Based on the experimental results obtained, the discussions presented and the conclusions made from this research, the following recommendations may be interesting for future investigation related to this topic:

1) Further investigate the separation mechanism of PBI membrane to different valent cations and anions in the aqueous solutions;

2) Extend the present work to the fabrication of PBI dual layer hollow fiber membranes through producing sponge-like support layer while keep the selective layer as thinner as possible to further decrease transport resistance;

3) Extend the present study to the application of PBI NF membranes in the organic solvent system due to the excellent chemical stability of PBI;

4) Couple with reactor to form membrane reactor in the aqueous or organic solvent environment based on the suitable molecular weight cut-off and charge characteristics which can be controlled through fabrication process;

5) Explore the commercialization of the PBI hollow fiber membrane in the separation of pharmaceuticals and fractionation of electrolytes.

REFERENCES

Afonso, M. D. & M. N. de Pinho, Transport of $MgSO_4$, $MgCl_2$, and Na_2SO_4 across an amphoteric Nanofiltration membrane, J. Membr. Sci. 179 (2000) 137.

Aimar, P., M. Meireles & V. Sanchez, A contribution to the translation of retention curves into pore size distribution for sieving membranes, J. Membr. Sci. 54 (1990) 321.

Anderson, J. L. & J. A. Quinn, Restricted transport in small pores. A model for steric exclusion and hindered particle motion, Biophysical J. 14 (1974) 131.

Aptel, P., N. Abidine, F. Ivaldi & J. P. Lafaille, Polysulfone hollow fibers-effect of spinning conditions on ultrafiltration properties, J. Membr. Sci. 22 (1985) 199.

Bindoff, A., The nanofiltration and reuse of effluent from the caustic extraction stage of wood pulping, Desalination 67 (1987) 455.

Boom, R. M., I. M. Wienk, Th van den Boomgaard & A. A. Smolders, Microstructures in phase inversion membranes, Part 2. The role of a polymeric additive, J. Membr. Sci., 73 (1992) 277.

Bouchet, R. & E. Siebert, Proton conduction in acid doped polybenzimidazole, Solid State Ionics., 118   (1999) 287.

Bowen, W. R., A. O. Sharif, Transport through microfiltration membrane-particle hydrodynamics and flux reduction, J. Colloid Interface Sci. 168 (1994) 414.

Bowen, W. R., H. Mukhtar, Characterization and prediction of separation performance of nanofiltration membranes, J. Membr. Sci. 112 (1996) 263.

Bowen, W. R., A.W. Mohammed & N. Hilal, Characterization of nanofiltration membranes for predictive purposes-Use of salts, uncharged solutes and atomic force microscopy, J. Membr. Sci. 126 (1997) 91.

Bowen, W. R. & A. W. Mohammad, Characterization and prediction of Nanofiltration membrane performance – A general assessment, Trans IChemE, Part A, 76 (1998) 885.

Bowen, W. R., A. N. Filippov, A. O. Sharif & V. M. Starov, A model of the interaction between a charged particle and a pore in a charged membrane surface, Adv. Colloid Interface Sci. 81 (1999) 35.

Bowen, W. R. & T. A. Doneva, Atomic force microscopy studies of nanofiltration membranes: surface morphology, pore size distribution and adhesion, Desalination 129 (2000) 163.

Bowen, W. R. & J. S. Welfoot, Modeling of membrane nanofiltration—pore size distribution effects, Chem. Eng. Sci. 57 (2002) 1393.

Bowen, W. R., J. S. Welfoot, Modeling the performance of membrane nanofiltration - critical assessment and model development, Chem. Eng. Sci. 57 (2002) 1121.

Broens, L. F., W. Altena & C. A. Smolders, Asymmetric membrane structures as a result of phase separation phenomena, Desalination 32 (1980) 33.

Cabasso, I., E. Klein & J. K. Smith, Polysulfone hollow fibers. I. Spinning and Properties, J. Appl. Polym. Sci. 20 (1976) 2377.

Cahn, J. W. & R. J. Charles, The initial stages of phase separation in glasses, Phys. Chem. Glasses, 6 (1965) 181.

Cao, C., T. S. Chung, S. B. Chen & Z. J. Dong, The study of elongation and shear rates in spinning process and its effect on gas separation performance of Poly (ether sulfone) (PES) hollow fiber membranes, Chem. Eng. Sci. 59 (2004) 1053.

Capelle, N., P. Moulin F. Charbit and R. Gallo, Purification of drug derivative from concentrated saline solution by nanofiltration, J. Membr. Sci. 196 (2002) 125.

Cassano, A.; Drioli, E.; Molinari, R.; Bertolutti, C. Quality improvement of recycled chromium in the tanning operation by membrane processes. Desalination 108 (1996) 193.

Chou, W.-L. & M.-C. Yang, Effect of take-up speed on physical properties and permeation performance of cellulose acetate hollow fibers, J. Membr. Sci. 250 (2005) 259.

Christy, C. & S. Vermant, The state-of-the-art of filtration in recovery processes for biopharmaceutical production, Desalination 147 (2002) 1.

Chung, T. S., S. K. Teoh, X. D. Hu, Formation of ultrathin high-performance polyethersulfone hollow-fiber membranes, J. Membr. Sci., 133 (1997a) 161.

Chung, T. S. The limitations of using Flory-Huggins equation for the states of solutions during asymmetric hollow fiber formation. J. Membr. Sci. 126 (1997b) 19.

Chung, T. S. & X. D. Hu, Effect of air-gap distance on the morphology and thermal properties of polyethersulfone hollow fibers, J. Appl. Polym. Sci., 66 (1997c) (1067).

Chung, T. S., The limitations of using Flory-Huggins equation for the states of solutions during asymmetric hollow fiber formation. J. Membr. Sci., 126 (1997d) 19.

Chung, T. S., Polybenzimidazoles, Handbook of thermoplastics, O. Olabisi ed.,T Marcel Dekker, New York, 701 (1997e).

Chung, T. S., A Critical Review of Polybenzimidazoles: Historical Development and Future R & D. J. Macromol. Sci., Polym. Rev., C37 (1997f) 277.

Chung, T. S., S. K. Teoh, W.W.Y. Lau, M. P. Srinivasan, Effect of Shear stress within the spinneret on hollow fiber: membrane morphology and separation performance. Ind. Eng. Chem. Res. 37 (1998) 3930.

Chung, T. S., J. J. Qin & J. Gu, Effect of shear rate within the spinneret on morphology, separation performance and mechanical properties of ultrafiltration polyethersulfone hollow fiber membranes, Chem. Eng. Sci. 55 (2000) 1077 and 56 (2001) 5869.

Chung, T. S., W.H. Lin & R. H. Vora, The effect of shear rate on gas separation performance of 6FDA-durene polyimide hollow fibers, J. Membr. Sci. 167 (2000) 55.

Cohen, C., G. B. Tanny & S. Prager, Diffusion-controlled formation of porous structures in ternary polymer systems. J. Polymer Sci., Polymer Physics, 17 (1979) 477.

Cuperus, F. P., Characterization of ultrafiltration membranes. Pore structure and top layer thickness, Ph.D thesis, University of Twenty, The Netherlands, 1990.

Deen, W. M., Hindered transport of large molecules in liquid-filled pores. AIChE J. 33 (1987) 1409.

Donnan, F. G., Theory of membrane equilibria and membrane potentials in the presence of non-dialysing electrolytes. A contribution to physical–chemical physiology, J. Membr. Sci. 100 (1995) 45.

Donnelly, D., J. Bergin, T. Duane & N. McNulty, Application of membrane bioseparation processes in the beverage and food industries, in Bionseparation and Bioprocessing, Vol. I: Biochromatography, membrane separations, modeling, validation, G. Subramanian ed., Wiley-VCH, 1998.

Drioli, E. & M. Romano, Progress and new perspectives on integrated membrane operations for sustainable industrial growth, Ind. Eng. Chem. Res. 40 (2001) 1277-1300.

Einstein, A., Investigation on the theory of the Brownian movement, R. Fourth ed., Dover, New York, 1956.

Ekiner, O. M. & G. Vassilatos, Polyaramide hollow fibers for H_2/CH_4 separation II Spinning and properties, J. Membr. Sci. 186 (2001)71.

Eriksson, P., Nanofiltration extends the range of membrane filtration, Env. Progress 7 (1988) 58.

Ernst, M., A. Bismarck, J. Springer & M. Jekel, Zeta-potential and rejection rates of a polyethersulfone nanofiltration membrane in single salt solutions, J. Membr. Sci. 165 (2000) 251.

Flory, P. J., thermodynamics of high polymer solutions, J. Chem. Phys., 10 (1942) 51.

Frank, M., G. Bargeman, A. Zwijnenburg & M. Wessling, Capillay hollow fiber nanofiltration membranes, Sep. Purif. Tech. 22-23 (2001) 499.

Fredrickson, A. G. & R. B. Bird, Non-Newtonian Flow in Annuli, Ind. Eng. Chem. 50 (1958) 347.

Garcia-Aleman, J.& J. M. Dickson, Mathematical modeling of Nanofiltration membranes with mixed electrolyte solutions, J. Membr. Sci. 235 (2004) 1.

Garem, A., G. Daufin, J. L. Maubois, B. Chaufer & J. Leonil, Selective separation of amino acids with a charged inorganic nanofiltration membrane: effect of physicochemical parameters on selectivity, Biotech. Bioeng. 54 (1997) 291.

Ghosh, A. C., S. Borthakur, M. K. Roy & N. N. Dutta, Extraction of cephalosporin C using supported liquid membrane, Sep. Technol. 5 (1995) 121.

Glipa, X., M. El Haddad, D. J. Jones & J. Roziere, Synthesis and characterization of sulfonated polybenzimidazole: a highly conducting proton exchange polymer, Solid State Ion. 97 (1997) 323.

Glipa, X., B. Bonnet, B. Mula, D. J. Jones & J. Roziere, Investigation of the conduction properties of phosphoric and sulfuric acid doped polybenzimidazole, J. Mater. Chem. 9 (1999) 3045.

Goulas, A. K., P. G. Kapasakalidis, H. R. Sinclair, H. R. Sinclair, R. A. Rastall & A. S. Grandison, Purification of oligosaccharides by nanofiltration, J. Membr. Sci. 209 (2002) 321.

Gross, R. J. & J. F. Osterle, Membrane transport characteristics of ultrafine capillaries, J. Chem. Phys. 49(1) (1968) 228.

Guizard, C. & G. Rios, Transport and fouling phenomena in liquid phase separation with inorganic and hybrid membranes, Fundamentals of inorganic membrane science and technology, A. J. Burggraaf, L. Cot eds., Elsevier, Amsterdam, pp 569-618 (1996).

Gupta, G. S. & Y. C. Sharma, Environmental management of textile and metallic industrial effluents, J. Coll. Interface Sci. 168 (1994) 118.

Hafiane, A., D. Lemordant & M. Dhahbi, Removal of hexavalent chromium by nanofiltration, Desalination 130 (2000) 305.

Hoffer, E. & O. Kedem, Hyperfiltration in charged membranes: the fixed charge model, Desalination 2 (1967) 25.

Horst, H. C., J. M. Timmer, T. Robbertsen & J. Leenders, Use of nanofiltration for concentration and demineralization in the dairy industry: Model for mass transport, J. Membr. Sci. 104 (1995) 205.

Horst, R., & B. A. Wolf, Calculation of the phase-separation behavior of sheared polymer blends, Macromolecules, 25 (1992) 5291.

Idris, A., A. F. Ismail, M. Noorhayati & S. J. Shilton, Measurement of rheologically induced molecular orientation using attenuated total reflection infrared dichroism in reverse osmosis hollow fiber cellulose acetate membranes and influence on separation performance, J. Membr. Sci. 213 (2003) 45.

Ismail, A. F., S. J. Shilton, I. R. Dunkin, S. L. Gallivan, Direct measurement of rheologically induced molecular orientation in gas separation hollow fiber membranes and effects on selectivity, J. Membr. Sci. 126 (1997) 133.

Ismail, A. F. & P. Y. Lai, Effects of phase inversion and rheological factors on formation of defect-free and ultrathin-skinned asymmetric polysulfone membranes for gas separation, Sep. Purif. Tech. 33 (2003) 127.

Kedem, O. & A. Katchalsky, Thermodynamic analysis of the permeability of biological membranes to non-electrolytes, Biochim. Biophys. Acta, 27 (1958) 229.

Kesting, R. E. & A. K. Fritzsche, Polymeric Gas separation Membranes, John Wiley and Sons, New York, 1993.

Kesting, R.E., Synthetic polymeric membranes, 2nd ed., McGraw-Hill, New York, 1985.

Kim, J. H., B. R. Min, J. Won, H. C. Park & Y. S. Kang, Phase behavior and mechanism of membrane formation for polyimide/DMSO/water system, J. Membr. Sci. 187 (2001) 47.

Kimbrough, D. A., Y. Cohen, A.M. Winer, L. Creelman & C. Mabuni, A critical assessment of chromium in the environment, Crit. Rev. Environ. Sci. Technol. 29 (1999) 1.

Kishore, N., S. Sachan, K. N. Rai & A. Kumar, Synthesis and characterization of a nanofiltration carbon membranes derived from phenol-fornaldehyde resin, Carbon 41 (2003) 2961.

Kiso, Y., T. Kon, T. Kitao & K. Nishimura, Rejection properties of alkyl phthalates with Nanofiltration membranes, J. Membr. Sci. 182 (2001) 205.

Koros, W. J. and G. K. Fleming, Review: Membrane-based gas separation. J. Membr. Sci., 83 (1993) 1.

Koros, W. J., Membrane: Learning a Lesson from Nature, Chem. Eng. Proc. (1995) 68.

Koros, W., Evolving beyond the thermal age of separation processes: Membrane can lead the way, AIChE J. 50(10) (2004) 2326.

Kreuer, K. D., A. Fuchs, M. Ise, M. Spaeth & J. Maier, Imidazole and parazole-based proton conducting polymers and liquids, Electrochim. Acta 43 (1998) 1281.

Kuder, J. E., J. C. Chen, Chemical Modification of Preformed Polybenzimidazole Semipermeable Membrane, US Patent 4,634,530, 1987.

Leob, S. & S. Sourirajan, Sea water demineralization by means of an osmosis membrane. Adv. in Chem. Ser. 38 (1963) 117.

Levich V. G., & V. S. Krylov, Surface tension driven phenomena. Annual Review of Fluid Mechanics, 1 (1969) 293.

Li, D. F., T. S. Chung, J. Z. Ren & R. Wang, Thickness dependence of macrovoids evolution in wet phase-inversion asymmetric membranes, Ind. Eng. Chem. Res., 43 (2004a) 1553.

Li, D. F., T. S. Chung & R. Wang, Morphology aspects and structure control of dual-layer asymmetric hollow fiber membranes formed by a simultaneous co-extrusion approach, J. Membr. Sci., 243 (2004b) 155.

Li, S. L., C. Li, Y. S. Liu, X. L. Wang & Z. A. Cao, Separation of L-glutamine from fermentation broth by nanofiltration, J. Membr. Sci. 222 (2003) 191.

Lin, K. Y., D. M. Wang & J. Y. Lai, Nonsolvent-Induced gelation and its effect on membrane morphology, Macromolecules 35 (2002) 6697.

Liu, Y., G. H. Koops & H. Strathmann, Characterization of morphology controlled polyethersulfone hollow fiber membranes by the addition of polyethylene glycol to the dope and bore liquid solution. J. Membr. Sci. 223 (2003) 187.

Luthra, S. S., X. J. Yang, L. M. Freitas do Santos, L. S. White & A. G. Livingston, Phase-transfer catalyst separation and re-use by solvent resistance nanofiltration membranes, Chem. Commun. 16 (2001) 1468.

Mahon, H. I., Permeability separatory apparatus and membrane element, method of making the same and process utilizing the same, U.S. Patent 3,228,876 (1966a).

Mahon, H. I., Permeability separatory apparatus and process using hollow fibers, U.S. Patent 3,228,877 (1966b).

Maladkar, N. K., Enzymatic production of Cephalexin, Enzyme Micro. Technol., 16 (1994) 715.

McHugh, A. J. & L. Yilmaz, The diffusion equation for polymer membrane formation in ternary systems, J. Polym. Sci., Part B: Polym. Phys., 23 (1985) 1271.

McKelvey, S.A., W.J. Koros, Phase separation, vitrification, and the manifestation of macrovoids in polymeric asymmetric membranes, J. Membr. Sci. 112 (1996) 29.

Michaels, A. S., Analysis and prediction of sieving curves for ultrafiltration membranes: A universal correlation. Sep. Sci. Technol. 15 (1980) 1305.

Model, F. S., H. J. Davis & J. E. Poist, PBI membrane for reverse osmosis, Reverse osmosis and synthetic membranes - theory-technology-engineering, S. Sourirajan ed., Ottawa, pp 231-248 (1977).

Mohammad, A. W., A Modified Donnan-Steric-Pore Model for Predicting Flux and Rejection of Dye/NaCl Mixture in Nanofiltration Membranes, Sep. Sci. Technol. **37**(5) (2002) 1009.

Mohammad, A. W., R. Othaman & N. Hilal, Potential use of nanofiltration membranes in treatment of industrial wastewater from Ni-P electroless plating, Desalination 168, (2004) 241.

Mulder, M., Basic Principles of Membrane Technology, Kluwer Academic Publisher, London, 1996.

Nakao, S. I. & S. Kimura, Models of membrane transport phenomena and their applications for ultrafiltration data, J. Chem. Eng. Japan 15(3) (1982) 200.

Nakao, S. I., Determination of pore size distribution, 3. Filtration membranes, J. Membr. Sci. 96 (1994) 131.

Newman, J. S., Electrochemical systems, Second Ed., Prentice Hall, USA, 1991.

Nguyen, Q. T. & J. Neel, Characterization of ultrafiltration membranes. Part IV. Influence of the deformation of macromolecular solutes on the transport through ultrafiltration membranes, J. Membr. Sci. 14 (1983) 111.

Noro, J., K. Maruyama, Y. Komatsu, Separation of chromium (VI) by combination of solvent and ion exchange methods, Anal. Sci. 17 (2001) 1332.

O'Dwyer, T. F. & B. K. Hodnett, Recovery of chromium from tannery effluent using a redox adsorption approach, J. Chem. Technol. Biotechnol., 62 (1995) 30.

Pastagia, K. M., S. Chakraborty, S. DasGupta, J. K. Basu & S. De, Prediction of permeate flux and concentration of two-component dye mixture in batch Nanofiltration, J. Membr. Sci. 218 (2003) 195.

Paul, D. R., Spin orientation during acrylic fiber formation, J. Appl. Polym. Sci. 13 (1969) 817.

Paul, E. L. & C. B. Rosas, Challenges for chemical engineers in the pharmaceutical industry, Chem. Eng. Progr. 86(12) (1990) 17.

Peeters, J. M. M., Characterization of nanofiltration membranes, Ph.D. Thesis, University of Twente, Enschede, The Netherlands, 1997.

Pekny, M. P., J. Zartman, W. B. Krantz, A. R. Greenberg & P. Todd, Flow-visualization during macrovoid pore formation in dry-cast cellulose acetate membranes, J. Membr. Sci. 211 (2003) 71.

Perry, M. & C. Linder, Intermediate reverse osmosis ultrafiltration (RO UF) membranes for concentration and desalting of low molecular weight organic solutes, Desalination 71 (1989) 233.

Petersen, R. J., Composite reverse osmosis and nanofiltation membranes, J. Membr. Sci. 83 (1993) 81.

Petruzzelli, D., R. Passino & G. Tiravanti, Ion exchange process for chromium removal and recovery from tannery wastes, Ind. Eng. Chem. Res., 34 (1995) 2612.

Pinnau, I. & B. D. Freeman, Formation and modification of polymeric membranes: Overview, in Membrane formation and modification, ACS symposium series 744, I. Pinnau & B. D. Freeman (Eds.) ACS, Washington DC, 1999.

Porter, M. C., Handbook of Industrial Membrane Technology, Noyes Publications, NJ, USA, 1990.

Powers E. J. and G. A. Serad, History and development of polybenzimidazoles, in High performance polymers: their origin and development, R. B. Seymour and G. S. Kirshenbaum ed., Elsevier Sci., 1986.

Pugazhenthi G. & A. Kumar, Chromium (VI) separation from aqueous solution using anion exchange membrane, AIChE J. 51 (2005) 2001.

Qin, J. J. & T. S. Chung, Effect of dope flow rate on the morphology, separation performance, thermal and mechanical properties, J. Membr. Sci. 157 (1999) 35.

Qin, J. J., J. Gu, T. S. Chung, Effect of wet and dry–wet spinning on the shear-induced orientation during the formation of ultrafiltration hollow fiber membranes, J. Membr. Sci. 182 (2001) 57.

Ram, M. J., Process for forming hollow polybenzimidazole filament for reverse osmosis application, US Patent 3,851,025, 1974.

Raman, L. P., M. Cheryan & N. Rajagopalan, Consider nanofiltration for membrane separations, Chem. Eng. Progr. 90(3) (1994) 68.

Rautenbach, R. & A. Groschl, Separation potential of nanofiltration membranes, Desalination 77 (1990) 73.

Rautenbach, R. & K. VoBenkaul, Pressure driven membrane process-the answer to the need of a growing world population for quality water supply and water disposal, Sep. Purif. Technol. 22-23 (2001) 193.

Ren, J. Z., T. S. Chung, D. F. Li, R. Wang & Y. Liu, Development of asymmetric 6FDA-2, 6 DAT hollow fiber membranes for CO_2/CH_4 separation-1. The influence of dope composition and rheology on membrane morphology and separation performance, J. Membr. Sci. 207 (2002) 227.

Reuvers, A. J., J. W. A. v.d. Berg & C. A. Smolders, Formation of membranes by means of immersion precipitation. I. A model to describe mass transfer during immersion precipitation, J. Membr. Sci. 34 (1987) 45.

Sahoo, G. C., A. C. Ghosh & N. N. Dutta, Recovery cephalexin from dilute solution in a bulk liquid membrane, Proc. Biochem. 32(4) (1997) 265.

Sahoo, G. C., Studies on emulsion liquid membrane extraction of Cephalexin, J. Membr. Sci. 145 (1998) 15.

Saitúa, H., M. Campderrós, S. Cerutti & A. P. Padilla, Effect of operating conditions in removal of arsenic from water by nanofiltration membrane, Desalination 172(2) (2005) 173.

Samms, S. R., S. Wasmus & R. F. Savinell, Thermal stability of proton conducting acid doped polybenzimidazole in simulated fuel cell environments, J. Electrochem. Soc. 143, 1225 (1996).

Sansone, M. J., *N*-substituted polybenzimidazole polymer, US Patent 4,898,917, 1990.

Schaep, J. C., Vandecasteele, A. W. Mohammad & W. R. Bowen, Modeling the retention of ionic components for different nanofiltration membranes, Sep. Purif. Technol. 22 (2001) 169.

Schaep, J., B. Van der Bruggen, C. Vandecasteele and D. Wilms, Influence of ion size and charge in nanofiltration, Sep. Sci. Technol. 14 (1998) 155.

Schäfer A. I., A. G. Fane & T. D. Waite, Nanofiltration-Principles and Applications, Oxford ; New York : Elsevier Advanced Technology (2005).

Schweitzer, P. A., Handbook of separations Technology, 2nd Ed., Mc Graw-Hill, 1988.

Scindia, Y. M., A. K. Pandey & A. V. R. Reddy, Coupled-diffusion transport of Cr(VI) across anion-exchange membranes prepared by physical and chemical immobilization methods, J. Membr. Sci., 247 (2004) 37.

Sengupta, A. K., S. Subramonian & D. Clifford, More on mechanism and some important properties of chromate ion exchange, J. Environ. Eng. 114 (1988) 137.

Sharma, R. R., R. Agrawal & S. Chellam, Temperature on sieving characteristics of thin-film composite nanofiltration membranes: pore size distributions and transport parameters, J. Membr. Sci. 223 (2003) 69.

Sheth, J. P., Y. J. Qin, K. K. Sirkar and B. C. Baltzis, Nanofiltration-based diafiltration process for solvent exchange in pharmaceutical manufacturing, J. Membr. Sci. 211 (2003) 251.

Shilton, S. J., Flow profile induced in spinneret during hollow fiber membrane spinning, J. Appli. Poly. Sci., 65 (1997) 1359.

Shilton, S. J., A. F. Ismail, P. J. Gough, I. R. Dunkin & S. L. Gallivan, Molecular orientation and the performance of synthetic polymeric membranes for gas separation, Polymer 38 (1997) 2215.

Shojaie, S. S., W. B. Krantz & A. R. Greenberg, Dense polymer film and membrane formation via the dry-cast process II. Model validation and morphological study, J. Membr. Sci., 94 (1994) 281.

Singh, S., K. Khulbe, T. Matsuura & P. Ramamurthy, Membrane characterization by solute transport and atomic force microscopy, J. Membr. Sci. 142 (1998) 111.

Sirkar, K. K., Membrane separation technologies: Current developments, Chem. Eng. Commun., 157 (1997) 145.

Smolders, C. A., A. J. Reuvers, R. M. Boom, I. M. Wienk, Microstructures in phase-inversion membranes. Part 1. Formation of macrovoids, J. Membr. Sci. 73 (1992) 259.

Spiegler, K. S., O. Kedem, Thermodynamics of hyperfiltration (reverse osmosis): Creteria for efficient membranes, Desalination 1 (1966) 311.

Staiti, P., F. Lufrano, A. S. Aricò, E. Passalacqua & V. Antonucci, Sulfonated polybenzimidazole membranes – preparation and physico-chemical characterization, J. Membr. Sci., 188 (2001) 71.

Strathmann, H., K. Kock, P. Amar & R. W. Baker, The formation mechanism of asymmetric membranes, Desalination, 16 (1975) 179.

Strathmann, H. and K. Kock, The formation mechanisms of phase inversion membranes, Desalination, 21 (1977) 241.

Strathmann, H., Membrane separation processes: Current relevance and future opportunities, AIChE J. 47 (2001) 1077.

Stryer, L., Biochemistry, 4th Ed., W. H. Freeman, New York, 1995.

Tandon, R. K., P. T. Crisp, J. Ellis & R. S. Baker, Effect of pH on chromium(VI) species in solution, Talanta 31 (1984) 227.

Tsai, H. A., L. D. Li, K. R. Lee, Y. C. Wang, C. L. Li, J. Huang & J. Y. Lai, Effect of surfactant addition on the morphology and pervaporation performance of asymmetric polysulfone membranes. J. Membr. Sci. 176 (2000) 97.

Tsai, H. A., D. H. Huang, R. C. Ruaan, & J. Y. Lai, Mechanical properties of asymmetric polysulfone membraens containing surfactant as additives, Ind. Eng. Chem. Res. 40 (2001) 5917.

Tsuru, T. M., Urairi, S. Nakao & S. Kimura, Negative rejection of anions in the loose reverse osmosis separation of mono- and divalent ion mixture, Desalination 81 (1991) 219.

Tsuru, T., T. Shutou, S. I. Nakao & S. Kimura, Peptide and amino acid separation with Nanofiltration membranes, Sep. Sci. Technol. 29 (1994) 971.

Urase, T., J. Oh & K. Yamamoto, Effect of pH on rejection of different species of arsenic by nanofiltration, Desalination, 117(1-3) (1998) 11.

Van der Bruggen, B., J. Schaep, D. Wilms & C. Vandecasteele, Influence of molecular size, polarity and charge on the retention of organic molecules by Nanofiltration, J. Membr. Sci. 156 (1999) 29.

Visvanathan, C., R. Benaim & S. Vigneswaran, Application of cross-flow electro-microfiltration in chromium wastewater treatment, Desalination 71 (1989) 265.

Vrijenhoek, E. M. & J. J. Waypa, Arsenic removal from drinking water by a "loose" nanofiltration membrane, Desalination 130 (2000) 265.

Wainright, J. S., J.-T. Wang, D. Weng, R. F. Savinell & M. Litt, Acid-doped polybenzimidazole: a new polymer electrolyte, J. Electrochem. Soc. 142(7) (1995) L121.

Wang, D. L., K. Li & W. K. Teo, Preparation of polyethersulfone and polyetherimide hollow fiber membranes for gas separation: effect of internal coagulant, Polym. Materials Science and Engineering, 77 (1997) 240.

Wang, T. & Z. Li, Some thermodynamic properties of calcium chromate, J. Chem. Eng. Data 49 (2004) 1300.

Wang, X. L., A. L. Ying and W. N. Wang, Nanofiltration of L-phenylalamine and L-aspartic acid aqueous solutions, J. Membr. Sci. 196 (2002) 59.

Wang, X. L., T. Tsuru, M. Togoh, S. I. Nakao and S. Kimura, Evaluation of pore structure and electrical properties of nanofiltration membranes, J. Chem. Eng. Japan 28(2) (1995) 186.

Wang, X. L., T. Tsuru, S. I. Nakao and S. Kimura, Electrolyte transport through nanofiltration membranes by the space-charge model and the comparison with Teorell-Meyer-Sievers model, J. Membr. Sci. 103 (1995) 117.

Wang, X. L., T. Tsuru, S. Nakao, S. Kimura, The electrostatic and steric-hindrance model for the transport of charged solutes through nanofiltration membranes, J. Membr. Sci. 135 (1997) 19.

Watson, B. M., C. D. Hornburg, Low energy membrane nanofiltration for removal of color organic and hardness from water supplies, Desalination 72 (1989) 11.

Weber, R., H. Chmiel & V. Mavrov, Characteristics and application of new ceramic nanofiltration membranes, Desalination 157 (2003) 113.

Weber, R., H. Chmiel and V. Mavrov, Characteristics and application of ceramic nanofiltration membranes, Ann. N.Y. Acad. Sci. 984 (2003) 178.

Whu, J. A., B. C. Baltzis, K. K. Sirkar, Modeling of nanofiltration-assisted organic synthesis, J. Membr. Sci. 163 (1999) 319.

Wijers, M. C., M. Jin, M. Wessling and H. Strathmann, Supported liquid membranes modification with sulphonated poly(ether ether ketone) Permeability, selectivity and stability, J. Membr. Sci. 147 (1998) 117.

Wijmans, J.G., J.P.B. Baaij, C.A. Smolders, The mechanism of microporous or skinned membranes produced by immersion precipitation, J. Membr. Sci. 14 (1983) 263.

Wijmans, J.G. and C.A. Smolders, Preparation of asymmetric membranes by the phase inversion process, in H.K. Londsdale and M.H. Pinho (Eds.), Synthetic Membranes: Science, Engineering and Applications, Dordrecht, The Netherlands, pp. 39-56, 1986.

Winston Ho, W. S. & K. K. Sirkar, Member handbook, Van Nostrand Reinhold, New York, 1992.

Wolf, B. A. Thermodynamic theory of flowing polymer solutions and its applications to phase separation. Macromolecules 17 (1984) 615.

Yang, C. & E. L. Cussler, Reactive extraction of penicillin G in hollow-fiber and hollow-fiber fabric modules, Biotechnol. Bioeng., 69(1) (2000) 66.

Yaroshchuk, A. E., Y. A. Vovkogon, Phenomenological theory of pressure-driven transport of ternary electrolyte solutions with a common coion and its specification for capillary space-charge model, J. Membr. Sci. 86 (1994) 1.

Yaroshchuk, A. E., Rejection mechanisms of NF membranes, Membr. Tech. 100 (1998) 9.

Yaroshchuk, A. E., Dielectric exclusion of ions from membranes, Adv. Colloid Interface Sci., 85 (2000) 193.

Yaroshchuk, A. E., Non-steric mechanisms of nanofiltration: superposition of Donnan and dielectric exclusion, Sep. Purif. Technol. 22-23 (2001) 143.

Youm, K. H. & W. S. Kim, Prediction of intrinsic pore properties of ultrafiltration membrane by solute rejection curves: effects of operating conditions on pore properties, J. Chem. Eng. Japan 24(1) (1991) 1.

Zeman, L. J. & A. L. Zydney, Microfiltration and Ultrafiltration: Principles and Applications, Marcel Dekker, Inc., New York, 1996.

Zeman, L. & M. Wales, Steric rejection of polymeric solutes by membranes with uniform pore size distribution, Sep. Sci. Technol. 16 (1981) 275.

Zhang, W., G. H. He, P. Gao & G. H Chen, Development and characterization of composite nanofiltration membranes and their application in concentration of antibiotics, Sep. Purif. Technol. 30 (2003) 27.

Zhao, D., A. K. SenGupta, L. Stewart, Selective Removal of Cr(VI) Oxyanions with a New Anion Exchanger, Ind. & Eng. Chem. Res. 37(11) (1998) 4383.

Zhu, A., W. P. Zhu, Z. Wu & Y. F. Jing, Recovery of clindamycin from fermentation wastewater with nanofiltration membranes, Water Res. 37 (2002) 3718.

APPENDIX A

CALCULATIONS OF SHEAR RATES AND SHEAR STRESSES

INDUCED AT THE OUTLET OF SPINNERET

The schematic diagram of non-Newtorian fluid flowing through a concentric annulus die within spinneret is illustrated in Figure A.1:
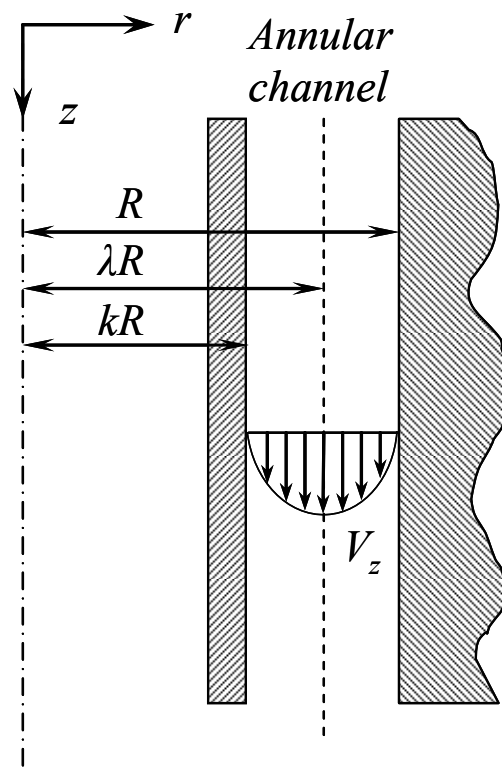

Fig. A.1 Schematic of non-Newtorian fluid flow through an Annulus Die

Equation of motion:

$$\tau_{rz} = \frac{1}{2}\frac{dP}{dz}\left(-r + \frac{(\lambda R)^2}{r}\right)$$

(A.1)

where

τ_{rz} = Shear stress

$\dfrac{dP}{dz}$ = Pressure drop along the die

λ = Constant of integration

$r = \lambda R$ = Radial distance at which $\tau_{rz} = 0$

Power law model:

$$\tau_{rz} = -K\left|\frac{dV_z}{dr}\right|^{n-1}\frac{dV_z}{dr}$$

(A.2)

where K, n are Rheological constant. In this study, m and n were obtained from the viscometric data of polymer dope solution.

Equations A.1 and A.2 are combined to give the shear rate distribution:

$$\frac{dV_z}{dr} = \left[\frac{1}{2K}\frac{dP}{dz}\left(r - \frac{(\lambda R)^2}{r}\right)\right]^{\frac{1}{n}}$$

(A.3)

Then, equation A.3 is integrated to give the velocity distribution [Fredrickson et al., 1958]:

$$V_z = R\left(\frac{dP}{dz}\frac{R}{2K}\right)^s \int_k^\rho \left(\frac{\lambda^2}{\rho} - \rho\right)^s d\rho \qquad k \leq \rho \leq \lambda$$

(A.4)

$$V_z = R\left(\frac{dP}{dz}\frac{R}{2K}\right)^s \int_\rho^1 \left(\rho - \frac{\lambda^2}{\rho}\right)^s d\rho \qquad \lambda \le \rho \le 1 \tag{A.5}$$

where $s = \dfrac{1}{n}$

Boundary condition: $V_z = 0$ at $\rho = k$ and $\rho = 1$

Equation A.3 and A.4 must give the same value of velocity at $\rho = \lambda$,

Thus, $\displaystyle\int_k^\lambda \left(\frac{\lambda^2}{\rho} - \rho\right)^s d\rho = \int_\lambda^1 \left(\rho - \frac{\lambda^2}{\rho}\right)^s d\rho \tag{A.6}$

The value of λ can be determined by solving numerically equation A.6 via trial and error.

Pressure drop along the die can be estimated using the dope flow rate by the following

equation [Bird, et al., 1987]:

$$\frac{dP}{dz} = \frac{2K}{R}\left(\frac{Q(s+2)}{(1-k)^{s+2}\,\pi R^3}\right)^{\frac{1}{s}} \tag{A.7}$$

where

Q is dope flow rate, cm^3/min.

Once the value of λ and pressure drop along the die are obtained, shear rates with

respect to different dope flow rates in the annular region can be calculated from Eq. A.3.

For example, in the Chapter II, the known experimental values are:

$R = 0.04\,cm$

$k = 0.5$

$s = 1/n = 1/0.7968 = 1.2550$

$K = 13.68\ Ns^n/m^2$

$Q = 0.25 \sim 10\ cm^3/min$

The computing program conducted with the software of Matlab 6.5 is given as follows:

```
*********************************************************************
clear
format long
a=0.5:0.00025:1.;
s=1/.7968;
tol=0.00001;

for i=1:2001
 for j=1:2001
   step1=(a(i)-.5)/2000;
   b(j)=0.5+(j-1)*step1;
   m(j)=(a(i)^2/b(j)-b(j))^s;
 end
   q1(i)=step1*(sum(m)-0.5*m(1)-0.5*m(2001));
 for k=1:2001
   step2=(1-a(i))/2000;
   c(k)=a(i)+(k-1)*step2;
   n(k)=(c(k)-a(i)^2/c(k))^s;
 end
   q2(i)=step2*(sum(n)-0.5*n(1)-0.5*n(2001));
   delta(i)=abs(q1(i)-q2(i));

   if delta(i) <tol, break, end
   lanmuda=a(i);
end
delta(i)                = 9.340e-006
lanmuda                 = 0.7330

clear
format long
step=0.00025;
a=0.5:0.00025:1.;
n=0.7968; K=13.28;
s=1/n;
Q = [0.25, 0.5, 1.0, 2.0, 3.0, 5.0, 7.0, 10.0];
R=0.04;
b=0.733;
for i=1:2001
   m(i)=(abs(b^2-a(i)^2))^(s+1)*a(i)^(-s);
end
   q3=step*(sum(m)-0.5*m(1)-0.5*m(2001));

shearrate=Q/(60*pi*R^3)*(1-b^2)^s/q3;
shearstress=K*(shearrate).^n;

shearrate
shearstress
*********************************************************************
```